NOVEMBER 1958 VOLUME 3 (1958) No. 5

GREGG M. SINCLAIR LIBRARY
UNIVERSITY OF HAWAII
8-7-63

NUCLEAR INSTRUMENTS

A JOURNAL ON ACCELERATORS, INSTRUMENTATION AND TECHNIQUES IN NUCLEAR PHYSICS

EDITOR: K. SIEGBAHN – UPPSALA

CONTENTS

I. F. ŠEVARAC, B. DJ. PEROVIĆ, B. V. DUNJIĆ and R. M. PROTIĆ, 60° sector type electromagnetic isotope separator in the Institute of Nuclear Sciences, Belgrade . . . 245
H. HINTENBERGER und L. A. KÖNIG, Massenspektrographen mit Doppelfokussierung erster Ordnung für alle Massen, die geringe Bildfehler in einem grossen Massenbereich entlang der Photoplatte aufweisen . . . 250
BRANKO BERKEŠ, Ein besonders einfacher Stromstabilisator höchster Qualität für Elektromagnete . . . 260
V. G. KIRILLOV-UGRYUMOV, L. P. KOTENKO, E. P. KUZNETSOV and A. V. SAMOILOV, Determination of the masses and momenta of charged particles from multiple scattering measurements in a propane bubble chamber . . . 265
HANSÉN, J., Read-out system for the Hutchinson-Scarrott analyzer . . . 271
PIERRE AMIOT, Device for thermal control of liquid hydrogen bubble chambers . . . 275
M. A. MEYER, P. H. STOKER and J. A. M. DE VILLIERS, Hodoscope system for experiments on the scattering of cosmic ray μ-mesons. PART I – Electronic circuits . . . 278
M. A. MEYER and J. A. M. DE VILLIERS, Hodoscope system for experiments on the scattering of cosmic ray μ-mesons. PART II – Performance of the hodoscope . . . 285
I. F. QUERCIA, Electronic apparatus for the measurement of dynamic magnetic fields . . . 292
S. M. SHAFROTH, E. N. STRAIT and R. T. CARPENTER, The response of a NaI(Tl) crystal to monoergic neutrons . . . 298
J. ERŐ, Radiofrequency modulation in the Thoneman ion source . . . 303
G. GOLDRING, M. BIRK, Z. KAMIL and D. MYDANSKY (Letter to the Editor), Method for eliminating the effects of amplitude drifts in measurements of ratios of counting rates . . . 307
News Item . . . 308

NORTH-HOLLAND PUBLISHING COMPANY – AMSTERDAM

NUCLEAR INSTRUMENTS

A journal on accelerators, instrumentation and techniques in nuclear physics

EDITOR: K. SIEGBAHN, UPPSALA

EDITORIAL BOARD:

J. B. ADAMS (CERN)
F. A. ALSINA (CNEA, Buenos Aires)
E. AMALDI (Rome)
H. L. ANDERSON (Chicago)
K. T. BAINBRIDGE (Cambridge, Mass.)
C. J. BAKKER (CERN)
P. R. BELL (Oak Ridge)
R. E. BELL (Montreal)
A. BERTHELOT (Saclay)
H. BRINKMAN (Groningen)
E. H. COOKE-YARBOROUGH (Harwell)
S. DE BENEDETTI (Pittsburgh)
M. DE HEMPTINNE (Louvain)
A. DE-SHALIT (Rehovoth)
M. DEUTSCH (Cambridge, Mass.)
S. DU TOIT (Pretoria)
B. S. DŽELEPOV (Leningrad)
W. GENTNER (CERN)
P. C. GUGELOT (Amsterdam)
H. HALBAN (Paris)
O. HAXEL (Heidelberg)
P. HUBER (Basel)
D. J. HUGHES (Brookhaven)
S. KIKUCHI (Tokyo)
J. KOCH (Copenhagen)
M. S. KOZODAEV (Moscow)
S. LIVINGSTON (Cambridge, Mass.)
E. M. MCMILLAN (Berkeley)
M. G. MEŠČERJAKOV (Moscow)
P. B. MOON (Birmingham)
M. L. OLIPHANT (Canberra)
W. PAUL (Bonn)
A. S. RAO (Bombay)
G. SALVINI (Rome)
P. SAVIĆ (Belgrade)
P. SCHERRER (Zürich)
CH. SCHMELZER (CERN)
H. W. B. SKINNER (Liverpool)
R. TANGEN (Blindern)
D. TAYLOR (Harwell)
V. I. VEKSLER (Moscow)
O. WERNHOLM (Stockholm)
G. VON DARDEL (CERN)
R. R. WILSON (Cornell)
S. D. WINTER (Saclay)

Contributions may be sent to the Editor, Professor K. Siegbahn, Institute of Physics, the University of Uppsala, either directly or through the intermediary of one of the members of the Editorial Board of the country of region in which the author is working. Contributions may be written in English, French or German, with an abstract in English.

Books for review should be sent to Professor Siegbahn.

Nuclear Instruments is published monthly. The subscription price of a volume of 360 pages is $ 17.00 (130 s), postage free.

Subscriptions should be sent to the publishers, North-Holland Publishing Company, P.O.Box 103, Amsterdam or to any subscription-agent.

No part of this issue may be reproduced in any form, by print, photoprint, microfilm or any other means without written permission from the publisher. Reprints, photoprints or microfilms are obtainable at cost from the publisher.

PHILIPS

equipment for Nuclear Physics and Atomic Energy

- Synchro-cyclotrons for various final energies.
- Cockcroft-Walton accelerators.
- Generators for very high d.c. voltages.
- Linear electron accelerators.
- Reactor control instrumentation
- Radiation measuring and detection equipment.
- Civil defence instruments.
- Area monitoring instrumentation.
- Geiger counter tubes.
- Photomultipliers.
- Radio-active isotopes.
- Air & gas liquefiers.
- Vacuum measuring equipment.

This panel permits the continuous programmed measurement and recording of the fast neutron and Gamma radiation levels at 8 different points in the building of the 150 MeV synchro-cyclotron of the "Laboratoire de Physique Nucléaire" in Orsay, France. It provides for "warning" or "alarm" signals, the latter with provision to switch off the cyclotron at a preset level of intensity.
Similar systems designed to your specific requirements can be supplied.

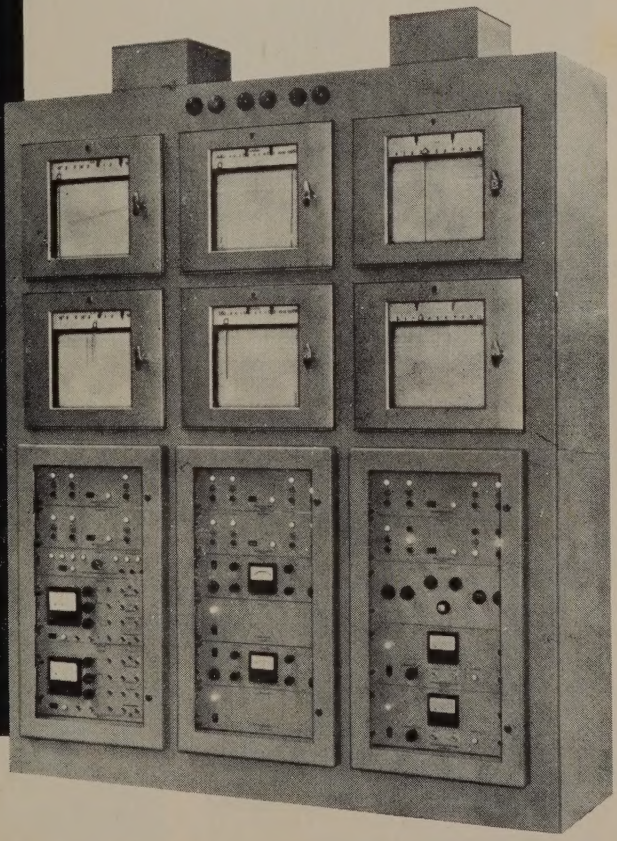

ZDO

PHILIPS
Nuclear Equipment

PHILIPS

For further information please apply to one of the following addresses:

N.V. PHILIPS' GLOEILAMPENFABRIEKEN, Scientific Equipment Department, Eindhoven-Holland
RESEARCH & CONTROL INSTRUMENTS LTD., Instrument House, 207/215, King's Cross Road, London WC1
PHILIPS ELECTRONICS INC., Instruments Division, 750, South Fulton Avenue, Mount Vernon N.Y. U.S.A.

New- a low cost neutron generator

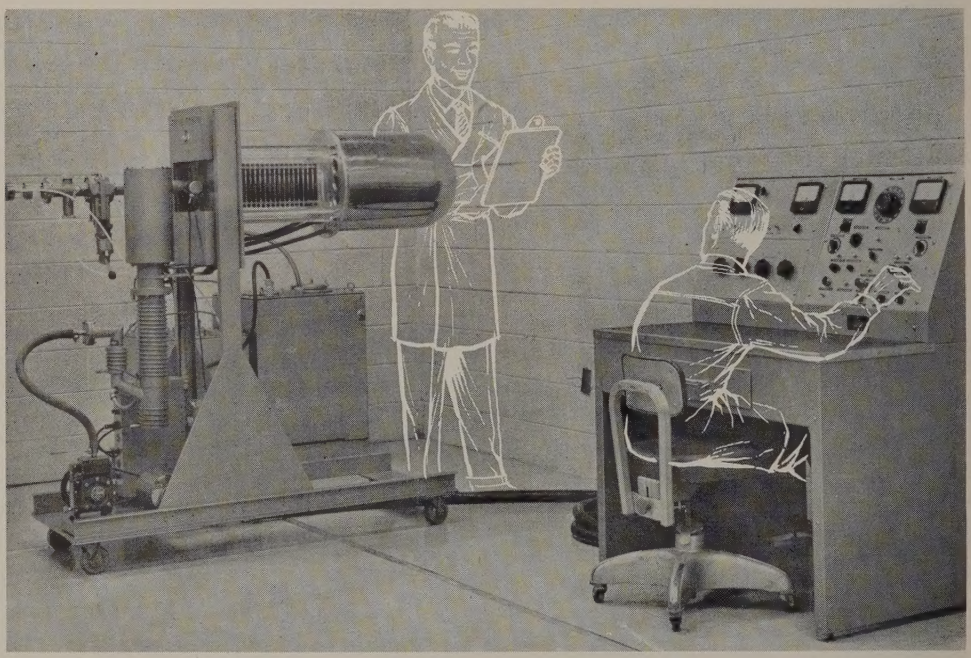

Facts and Features:

Output up to 10^{10} neutrons/sec continuous, Remote Operation, Mobile, No special building facilities required, Easily operated and maintained.

Designed for...

- Activation Analysis
- Neutron Scattering and Nuclear Reaction Research
- Radiation damage studies
- Biological Studies
- Training of Nuclear Scientists
- Instrument calibration
- Well Logging Research
- Model 100-I pictured at left, complete with targets and installed, $ 20,000. F.O.B, Austin.

For further information, write:

TEXAS NUCLEAR CORPORATION

P. O. BOX 9267 • AUSTIN 17, TEXAS

To meet the most exacting requirements of gamma ray analysis . . .

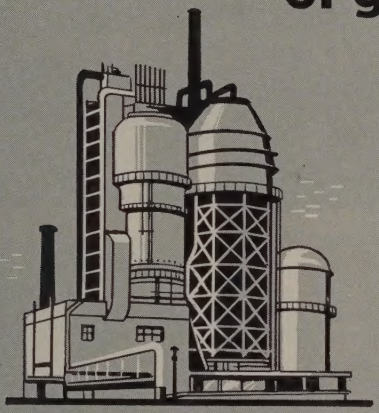

IN INDUSTRY . . . OR RESEARCH

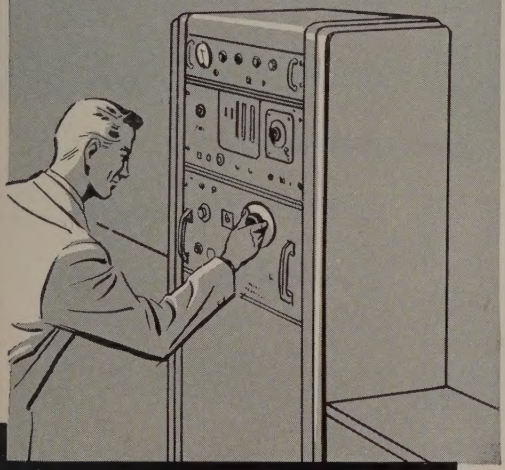

THE TMC Model PA-2A AMPLISORTER

Gamma ray spectrum analysis — from high energy industrial "tags" to the lowest level biological tracers — is more accurate when done with the precision TMC Model PA-2A Amplisorter. The Model PA-2A combines an extremely fast, accurate single-channel pulse height analyzer with a non-overloading linear amplifier in a single compact unit. The PA-2A offers many design and performance advantages for precision gamma counting. Here are a few:

ANALYZER

Fast — counts pulses only 0.5 us. apart . . . *Accurate* — discerns pulse differences as small as 0.5 volts using a *Bell-Francis* ×10 window amplifier . . . *Stable* — maintains 1% window width stability in a 1 volt window over long periods . . . *Dependable* — quality components used throughout, including six *E180F* type 10,000 hour premium tubes which do *not* require pair matching.
Differential/Integral switch provides two counting modes — differential for "window" counting, integral for counting *all* pulses above the baseline (useful in setting up experiments or testing instrument). Spectra can be plotted in the differential mode by adjusting the 0-100 volt variable baseline control to the lower limit of a 0-5 volt wide window and counting all pulses within the window.

AMPLIFIER

Wide Band — Dynamic Range of 5,000 to 1 means accurate counting of low level pulses in the presence of a large, high energy background; and counting of pulses 5,000 times greater than corresponding maximum output without pulse stretching . . . *Non-Overloading* — amplifier has special high level output stage designed to be ultra-linear up to 100 volts and limit sharply at 120 volts to prevent overloading following instruments . . . *Ultra-linear, Fast Rise* — 0.1% for output up to 100 volts; 0.15 us. rise time, 10%–90%; gain of 8000.
Clipping time selector switch provides a choice of 0.5, 1, 2, 5, 10, 20 us. R.C. clipping, or 1.0 us. delay line. Internal adjustment also permits choice of long or short (2 us.) R.C. clip at the input.

Price $1000 f.o.b. New Haven

Both the Analyzer and the Amplifier are available as separate units: Model AL-4A Linear Amplifier, Model PA-1A Single-channel Analyzer.
Complete details of the PA-2A Amplisorter or related TMC scalers, ratemeters and detectors are available on request.

TMC

TECHNICAL MEASUREMENT CORPORATION

140 STATE STREET, NEW HAVEN, CONNECTICUT

ARCO High Energy and

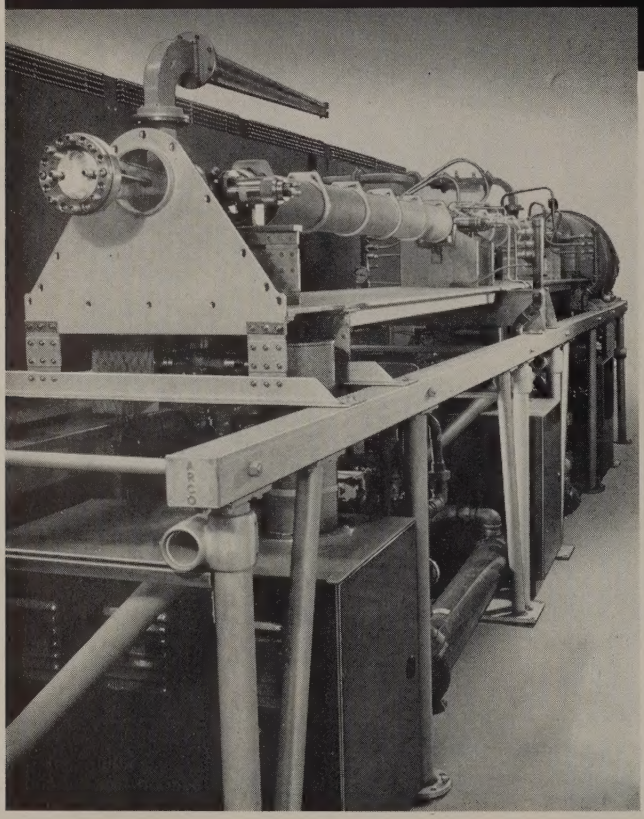

ARCO

designs and manufactures high power, high energy particle accelerators and associated apparatus. Modular construction simplifies meeting individual needs for complete systems or individual components.

ELECTRON LINEAR ACCELERATORS

ARCO linear accelerators provide intense neutron, X-ray, and electron beams for neutron physics and sub-critical reactor core studies, and for basic investigations in solid state physics and radiation chemistry. Linear accelerators produce intense neutron pulses for time-of-flight studies. Photofission reactions are among the most efficient neutron producing reactions. Up to 3×10^{12} neutrons per second (average) can be produced per kilowatt of electron beam. Pulse yields are on the order of 1×10^{3} greater.

In nuclear chemistry, precisely controlled bremsstrahlung permit investigations of photonuclear as well as neutron reactions. Pulsed electron beams are used in solid state physics to help evaluate radiation damage, and in radiation chemistry and food research to study free radicals and other short lived transients. ARCO accelerators provide the high beam energies needed for irradiation of pressurized systems and thick specimens, and the high power needed for low yield work.

ARCO is presently building electron linear accelerators with electron beam power variable to 48 kilowatts; beam energy variable to 77 Mev; and peak beam current variable to 0.8 amperes; pulse repetition rates to 800 pulses per second, with pulse lengths from 0.1 microsecond to 30 microseconds. ARCO is equipped to meet your needs, whether modest or exceeding these characteristics.

Particle Accelerators Associated Apparatus

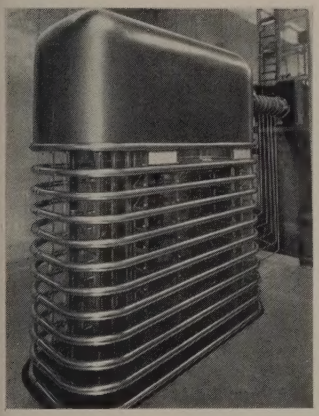

COCKCROFT-WALTON ACCELERATORS

ARCO builds both electron and positive ion C-W accelerators. Electron accelerators are suggested for shallow irradiation where economy, dependability and ruggedness are required. Positive ion machines provide neutrons from thermal to 14 Mev, in addition to protons, deuterons, tritons, alpha particles and heavy gas ions. Pulsed beams are available over a wide range of lengths and repetition rates.
Machines can be supplied with beam energies from 40 to 800 Kev, beam current to 10 ma, neutron yields to 10^{11}n/sec., 0.1% regulation, and ion beam focus to 0.3 cm diameter.

POSITIVE ION LINEAR ACCELERATORS

Positive Ion Accelerators include equipment to continuously vary and regulate ion beam energy. Large electro-magnets are not used; therefore, large stray magnetic fields are avoided and main accelerator cavities may be added later to produce higher beam energies.
ARCO machines provide proton energy from 5 to 12 Mev, Deuteron energy from 2.5 to 6 Mev, peak beam current to 300 μa, and average beam current to 10 μa.

CUSTOM PRECISION ELECTROMAGNET SYSTEMS

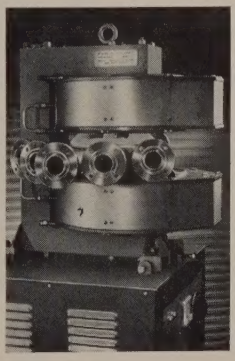

ARCO builds electron and ion beam analyzing systems and specialized magnets; also builds integrated systems involving magnets, high vacuum systems, drift tubes and Faraday cup current collectors, providing energy resolution to 0.5%. Magnet field strengths are variable to 12,000 oersteds; current regulated power supplies are available with regulation of .1% or .01%.

HIGH VACUUM SYSTEMS

Non-refrigerated traps, metal-gasketed flanges, bellows-sealed valves and automatic shut-off and restart controls are features of all-metal ARCO vacuum systems. Components accept 450° C bakeout. Units are available as separate components. System ranges include operating vacuums from 10^{-6} to 10^{-9} mm Hg.; pumping speeds from 10 to 10^3 liters/sec.

HIGH POWER DC SUPPLIES

ARCO designs and builds power supplies covering the range 100 KV to 3 Mev with output variable to 30 Kw.

SELF-CALIBRATING INTEGRATING ELECTROMETERS

ARCO AEI-101 current electrometer integrator is a single-chassis unit useful with particle accelerators as well as in integrating fluctuating light, velocity, flow, and other transducible factors. Desired integrated values can be preset. Input current range (+ or −) is 500 $\mu\mu$a to 1 ma covered in 6 decade ranges. Integrator range is 1 millimicrocoulomb to 100 coulombs. Accuracy is ±0.5% of current or charge reading. Input voltage is 0 ±2 mv, integrating rate varies from 1/sec to 1/minute; integrator drift is 0.1 unit/hr, output is 0 to 10 mv (current range) and 0 to 50 v on charge increments. Model AEI-101 is only 8¾" high, and fits a standard relay rack. Depth is 10".

ARCO IRRADIATION SERVICE CENTERS

At Rockford, Illinois, and Walnut Creek, California, ARCO irradiation facilities may be leased for an hour or many days. High energy industrial accelerators are available at both locations. The Service Centers include laboratories, locked storage and other facilities.

For information, write Dept. N 11

High energy radiation for research and processing

ARCO APPLIED RADIATION CORPORATION
Walnut Creek, California
YEllowstone 5-2250, Cable "ARCO"
5106

INTERNATIONAL

advertise

YOUR NUCLEAR PRODUCTS IN

sell

YOUR NUCLEAR PRODUCTS

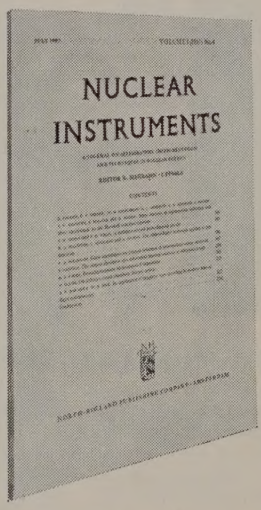

reap

YOUR NUCLEAR SALES
REWARDS

world wide

KEY NUCLEAR MANAGEMENT
NUCLEAR SCIENTISTS
NUCLEAR ENGINEERS
NUCLEAR PRODUCTION
PERSONNEL

SUBSCRIBE TO

you reach

THE WHOLE
NUCLEAR SALES WORLD IN

Entirely international in scope Nuclear Instruments is the one nuclear scientific journal that has an established subscription clientele through-out the whole world-where-ever nuclear men are at work—they want your nuclear products—they need your nuclear products—advertise in Nuclear Instruments and tell them WHAT – HOW – WHERE they can get your nuclear products

GO INTERNATIONAL WITH YOUR SALES PROGRAM TODAY WRITE

WILLIAM F. BAARS - ADVERTISING MANAGER NORTH-HOLLAND PUBLISHING COMPANY

P.O. BOX 103 – AMSTERDAM, HOLLAND

INTERNATIONAL

These names make NUCLEAR POWER

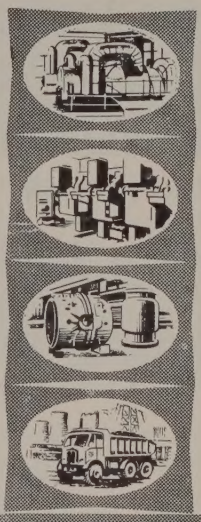

C. A. PARSONS & COMPANY LTD.

A. REYROLLE & COMPANY LTD.

HEAD, WRIGHTSON & COMPANY LTD.

SIR ROBERT McALPINE & SONS LTD.

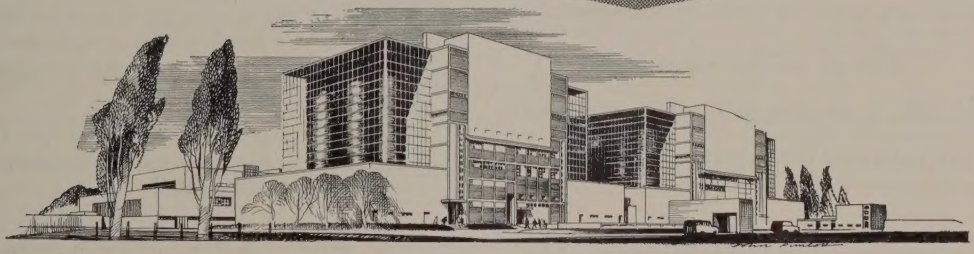

Bradwell, Essex, has leapt into fame as the site of the first commercial nuclear power station in the world to be built by N.P.P.C. Eight names make The Nuclear Power Plant Company Limited. N.P.P.C. thus combines the resources of eight specialist companies whose individual skills are co-ordinated to form a unified team capable of undertaking the construction of complete nuclear power stations throughout the world.

Bradwell nuclear power station will have a guaranteed output of 300 Megawatts. It is being built by The Nuclear Power Plant Co. Ltd. for the Central Electricity Generating Board.

A Greater Britain through Nuclear Power

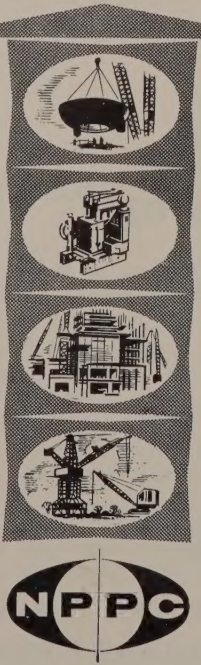

WHESSOE LTD.

STRACHAN & HENSHAW LTD.

ALEX. FINDLAY & COMPANY LTD.

CLARKE, CHAPMAN & COMPANY LTD.

NPPC

THE NUCLEAR POWER PLANT COMPANY LIMITED · BOOTHS HALL · KNUTSFORD · CHESHIRE · ENGLAND

TGA NP3A

LELAB METAL-WALLED G-M TUBES
for anti-coincidence applications where uniformity counts !

Lelab Counter Tubes are individually constructed, filled, and tested. Each is fabricated almost entirely of metal. All components are confined within the diameter of the tube shell to permit close stacking.

Compare our low prices on these superior tubes!

(Makers of Lelab [Robinson-Selverstone Type] Probe Counters for neurosurgery and where a fine needle-like probe for highly localized measurements is useful.)

Write for complete information

H. W. Leighton Laboratories

York & Sunset Lane-Hatboro, Pa. U.S.A.

NORTH-HOLLAND BOOKS

ELECTROMAGNETIC ISOTOPE SEPARATORS AND APPLICATIONS OF ELECTROMAGNETICALLY ENRICHED ISOTOPES

By J. KOCH *(Editor)*,
R. H. V. M. DAWTON, M. L. SMITH and W. WALCHER

6 x 9″ xii + 314 pp. 156 illus. 53 s.

"This is a very welcome book on a subject which had its beginnings 24 years back, which has grown to undreamt of proportions during and after the war, and of which this is the first comprehensive monograph. It is written by a team of experts with first-hand experience in electromagnetic separators... it tells in a masterly way the fascinating "success story" of a physical instrument which has grown into a giant". (D. GABOR in *British Journal of Applied Physics*)

Sole Agency for U.S.A.:
Interscience Publishers Inc. New York
NORTH-HOLLAND PUBLISHING COMPANY
AMSTERDAM

NORTH-HOLLAND BOOKS

just out

Internal Conversion Coefficients

by

M. E. ROSE

Chief Physicist, Oak Ridge National Laboratory

9 x 12½″ XXII + 176 pages 40 s.

THE CONTENTS

I INTRODUCTION
1. Definition of the Internal Conversion Process
2. The Selection Rules, Mixtures of Multipoles
3. Theoretical Considerations
4. Method of Calculation and Explanation of the "Tables"

II NUMERICAL RESULTS

K shell Internal Conversion Coefficients; L_I, L_{II}, L_{III}, subshell Internal Conversion Coefficients; Total M shell Internal Conversion Coefficients, $Z \geqslant 65$; M_I, M_{II}, M_{III}, M_{IV}, M_V, subshell Internal Conversion Coefficients, $Z \geqslant 65$; Radial Integrals for K Conversion

Sole Agency for U.S.A.: Interscience Publishers Inc. – New York

NORTH-HOLLAND PUBLISHING COMPANY — AMSTERDAM

NOW

"Completely Transistorized" Model 49-21 Scaler

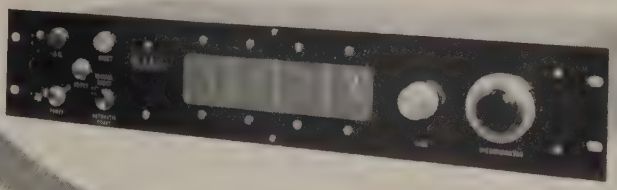

- **RELIABLE**
- **VERSATILE**
- **RUGGED**
- **COMPACT**

The Model 49-21 utilizes a completely transistorized digital read-out system with *no* need for relays or mechanical switching. The displayed numbers can be read at wide angles and in *direct* sunlight. Life testing in the RIDL laboratory has demonstrated the complete reliability of the components used: over five million counts per light without a failure. Printed circuitry is used throughout. The design of the circuitry is such as to provide extremely wide margins; a variation of the supply voltage over a range of ± 20% will not affect the operation.

- **Resolving Time:** ½ microsecond at the decades.
- **Maximum Counting Rate:** Two mega-cycles.
- **Maximum Count Capacity:** 10^8 (4 decades followed by a four place Sodeco register).
- **Reset:** Electrical for decades and register - provision for local or remote operation.
- **Sensitivity:** 1 millivolt to 1 volt.
- **Amplifier:** Equipped with fixed amplitude discriminator—fine and coarse gain adjustments.
- **Input Power:** 110-220 volts; 50-60-400 cycles (can be supplied with a battery pack for use as a portable scaler).
- **Dimensions:** 3½" high x 19" wide x 15" deep—fits in standard relay rack.

Vacuum tube high voltage supplies, up to 5000 volts, can be supplied for use with the 49-21. **QUICK DELIVERY**

NEW-FULLY AUTOMATIC

MODEL 50-1 SCINTILLATION SPECTROMETER

The 50-1 Spectrometer consists of the Model 33-1 Single Channel Pulse Height Analyzer (modified ORNL Q-1192), containing an Argonne type A-61 non-overloading linear amplifier, the Model 39-2 Electronic Sweep-Count Rate Meter and High Voltage Supply along with a 2 second Brown ElectroniK Recorder.
Reliable, proven circuitry is used throughout these units to assure extreme dependability and high linearity. The *Electronic* Sweep circuit, offering a wide dynamic range, in conjunction with automatic reset features, allow maximum reproducibility of data.

The Model 50-1 Spectrometer - - - complete as shown $ 2,395.00

The Models 49-21 and 50-1 are just two of the many fine instruments manufactured by RIDL. REMEMBER, whatever your instrumentation problem may be, RIDL has the solution. Our staff is always available to answer your inquiries. Write today for complete information.

RIDL

Radiation Instrument Development Laboratory, Inc.

5737 South Halsted Street, Chicago 21, Illinois • TRiangle 3-2345

A Beta-Ray Spectrometer in commercial production, engineered to highest standards of performance

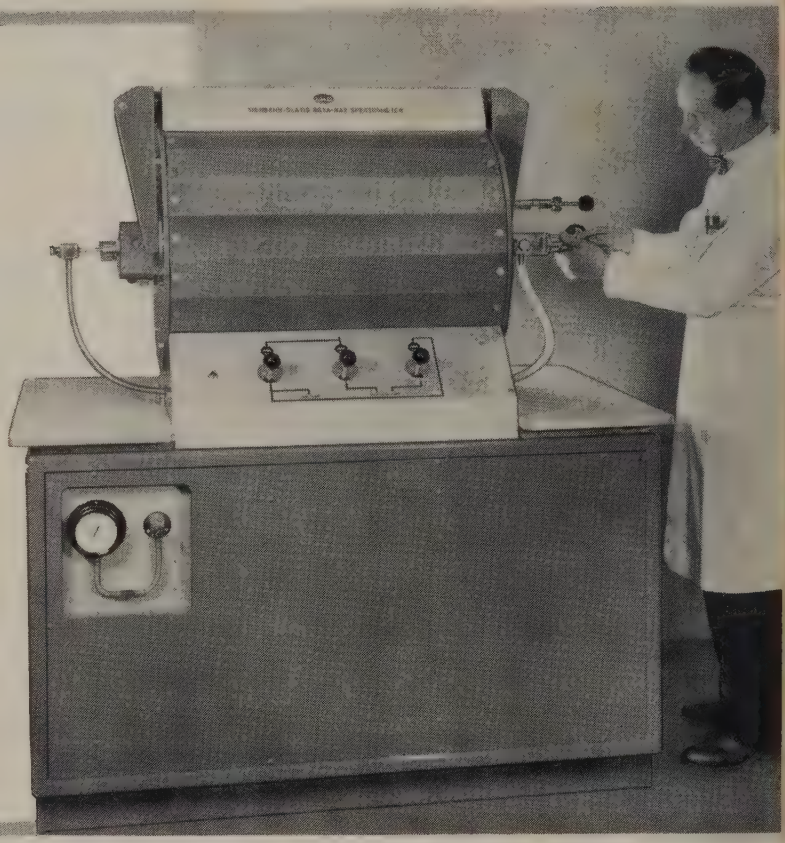

▲ Operator inserting source holder into spectrometer chamber through lock valve. Control console and 50 kW motor-generator set not shown.

The LKB 3024B Siegbahn-Slätis Intermediate Image Beta-Ray Spectrometer

Features distinguishing the LKB Beta-Ray Spectrometer include:

Energy Range: 1 keV to 8.3 MeV electrons, or, when used as pair spectrometer, up to 17.6 MeV gammas.

Transmission: up to 8% of 4π.

Resolution: 0.7% at 1% transmission or 1.2% at 6% transmission.

Linearity: $B\rho$ proportional to magnet current within ±0.11% between 36 keV and 8.3 MeV.

Shielding: Spectrometer is iron-jacketed, insuring extremely low stray-field level.

Operation: Safe and fast. There are protective devices against all possible kinds of failure. Precision electronic regulator with follow-up servo facilitates current setting.

To be shown at the Geneva "Atoms for Peace" Exhibition, Sept. 1–14, 1958

Other LKB Products for the Nuclear Physicist:
Custom-built Precision-Stabilized and Transient-Free High Current D. C. Power Supplies.
Autovac Vacuum Gauge.

LKB

Write for details and references to:

LKB-PRODUKTER

Fabriksaktiebolag

P.O. Box 12220, Stockholm 12, Sweden
Distributors throughout the world

NUCLEAR INSTRUMENTS 3 (1958) 245–249; NORTH-HOLLAND PUBLISHING CO. – AMSTERDAM

60° SECTOR TYPE ELECTROMAGNETIC ISOTOPE SEPARATOR IN THE INSTITUTE OF NUCLEAR SCIENCES — BELGRADE

I. F. ŠEVARAC, B. Dj. PEROVIĆ, B. V. DUNJIĆ and R. M. PROTIĆ

Laboratory of Physics, Institute of Nuclear Sciences "Boris Kidrich"

Received 3 August 1958

A 60° sector type electromagnetic isotope separator with homogeneous magnetic field is described. The radius of the ion path is 75 cm. The ion source of magnetic type with oscillating electrons is used. Characteristics of the separator and results of measurements are given.

1. Description of the Assembly

The construction of the electromagnetic isotope separator in the Institute began toward the end of 1953. In type and design, the machine is similar to the one at Saclay, constructed by R. Bernas in 1952. The whole machine is shown in the schematic diagram fig. 1.

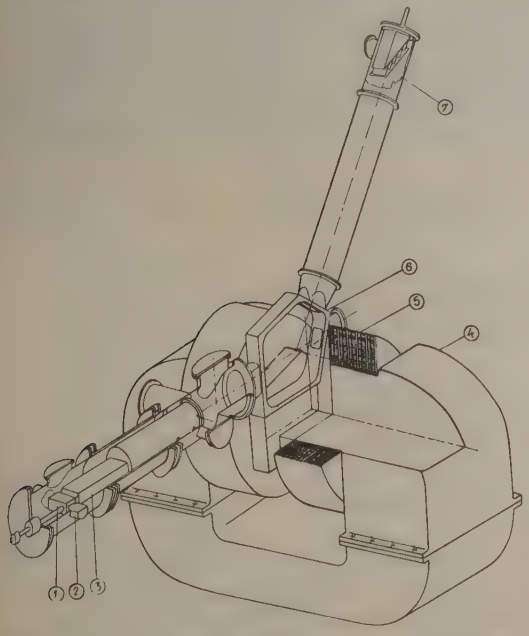

Fig. 1. Exploded view of isotope separator. 1. Ion source. 2. Ion source magnet. 3. Extraction electrode. 4. Magnet yoke. 5. Magnetic coil. 6. Vacuum chamber. 7. Collector.

The separator magnet has a sector angle 60°, the radius of the main ion path 75 cm, and the gap 75 mm. This gives a satisfactory mass dispersion on the collector, a complete separation of the elements from the middle of the atomic scale, same as considerable enrichment of heavy elements.

The homogeneous magnetic field was chosen for the analysis of the beam. Magnet coils are fed with the current of 30 A/300 V. The current is stabilized at 1/10 000. The measured maximum field intensity was $B_{max} = 11\,200$ G. The distribution of the magnetic field in the gap, along the ion beam and perpendicular to the beam, measured by a bismuth spiral is given in fig. 2.

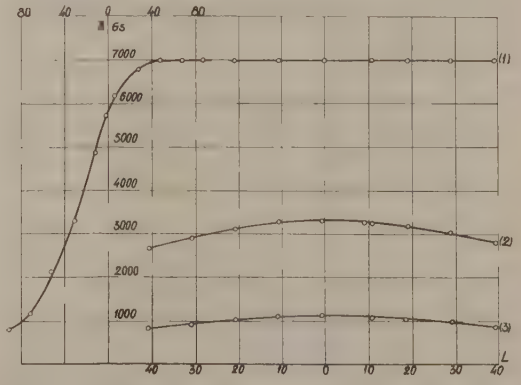

Fig. 2. (a) Fieldshape parallel to the beam. (b) Fieldshape perpendicular to the beam. 1. Inside of the pole pieces. 2. 27.5 mm outside of the pole pieces. 3. 67.5 mm outside of the pole pieces.

The evacuation of the system is achieved by oil condensation pump, having the pumping speed of 1500 l/sec, provided with liquid air trap and a mechanical pump of pumping speed of 28 m^3/h. The different working conditions of the pumping system are effected by a valve block which connects the two pumps together (fig. 3). These working conditions are resumed in table 1. The vacuum in the system, measured by an ionization gauge, was usually in the range of $2–5 \times 10^{-5}$ mm Hg.

Ions were produced in the magnetic ion source with electrons oscillating along the axis of discharge and with ion extraction perpendicular to the axis of discharge. Tungsten filament of 0.5 mm and 1.0 mm and electron acceleration voltage of 40–120 V are used. The copper discharge chamber is covered with several layers of thin stainless steel plates which act as a thermal reflector. The source slit dimensions are 50×2 mm. The pyrex glass and lava furnace are used. The ion source magnet can yield a magnetic field up to 1000 G.

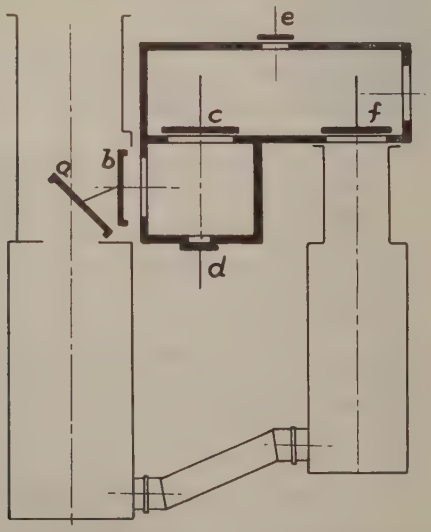

Fig. 3. Schematic diagram of vacuum valve.

The system for the ion beam extraction, made according to Pierce is provided with an additional electrode for compensation of the ion beam space charge. High voltage supply may give 60 kV and the current of 50 mA. Its stabilisation is 1/3000, obtained by method of series stabilisation.

Table 1

		Valves opened		Valves closed			
1	Normal pumping	a	f	b	c	d	e
2	Direct pumping	b	c	a	d	e	f
3	Pump. without back. pump	a		b	c	d	e + f
4	System under vacuum isolated from the pumps	b	e	a	c	d	f

The collector consists of different movable pockets, made of copper plates whose base is cooled with water. In dependence on the ion source efficiency, collected isotopes are of the order of mg/h. In order to control permanently conditions of separation on the collector, it was equiped with a special arrangement for the visual observation of isotope distribution and yield. This arrangement consists of a probe which oscillates in front of the collector and transmits to the osciloscope the datas of the distribution and intensity of the ion beam.

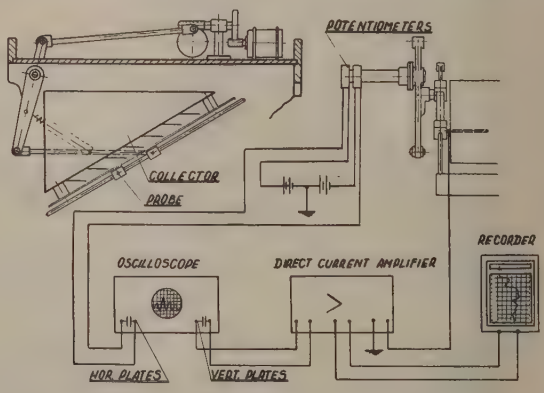

Fig. 4. Schematic diagram of the scanning assembly.

Fig. 4 gives the picture of assembly with probe and scheme of measurements with it.

In fig. 5 can be seen a photo of the separator with supplies and control arrangement.

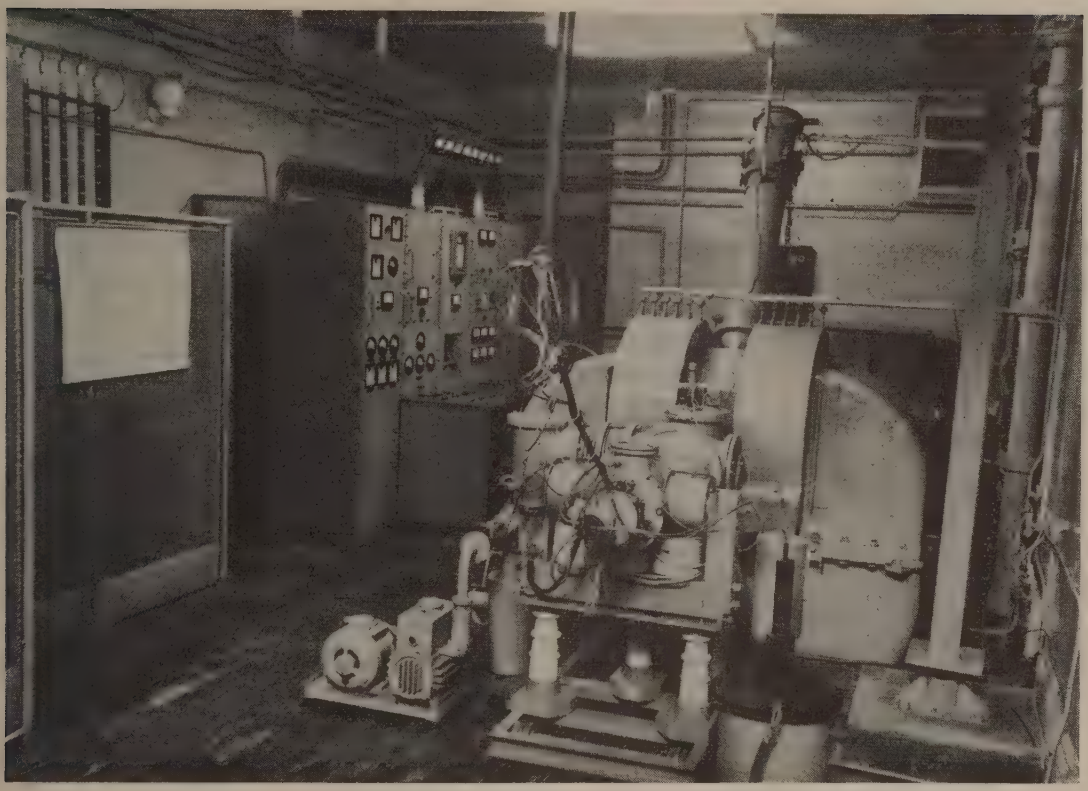

Fig. 5. Separator with supplies and control arrangement.

2. Working Conditions of the Machine and some Results

The work of the whole machine and especially of the ion source is strongly dependent on many various geometrical and physical factors. Hence, it is necessary to find the optimal running conditions to obtain maximum yield and high separation factor with minimal material and power consumption in the source. The influence of the main acting parameters can be presented as follows:

(a) The influence of the electron current, i.e. the filament heating power. From all measurements of anode current the curves of conventional type are obtained, showing a marked tendency to saturation at determined values which increase with increasing anode voltage. The collector current curves follow very exactly these of the anode current.

(b) The dependence of the total anode current, extracting electrode and collector current on the energy of ionizing electrons is given in fig. 6.

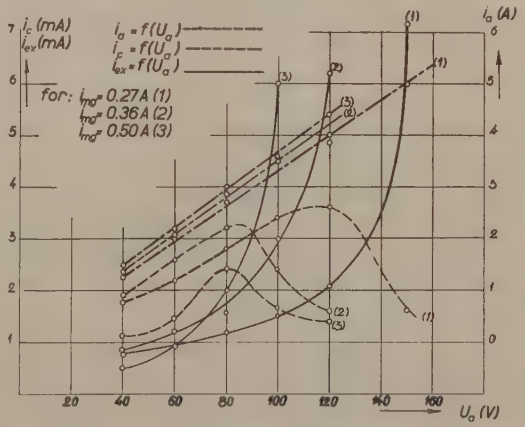

Fig. 6. Dependence of collector, extracting electrode and anode current on anode voltage.

These characteristics are obtained for different values of the ion source magnetic field. The

anode current increases almost linearly with voltage in whole examined range. At some voltage values, differing for different magnetic fields, starts a sharp increase of unuseful extracting electrode current with a parallel marked decrease of the collector current. The ratio of the collector to the extracting electrode current (i_c/i_{ex}), which is the measure of the ion transmission, decreases at the same time very sharply. The sharp changes of these currents are followed by moving and distortion of the collector image. Therefore the work with higher ionizing electron energy is not recommended.

(c) The effect of the ion source magnetic field is shown in fig. 7. The anode current is practically

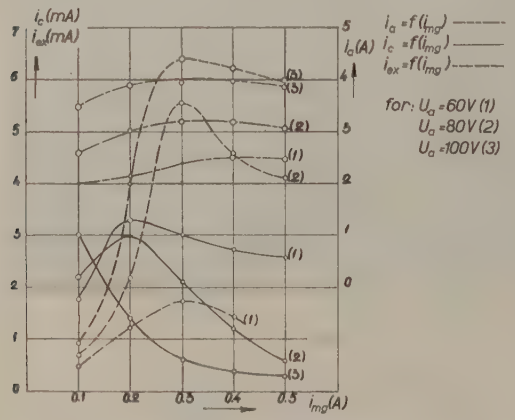

Fig. 7. Dependence of collector, extracting electrode and anode current on ion source magnetic field.

unchanged with increase of magnetic field while ionic currents are strongly effected by it. The optimum values for collector current are obtained by using smaller values of the ion source magnetic field. It is evident from measurements and from ratio of the collector to anode current (i_c/i_a), that work with smaller magnetic field is more efficient.

(d) The influence of the extracting voltage. The anode current remains practically unchanged while the curves of the collector and extracting electrode current, given in fig. 8, show clearly the focusing action of the higher accelerating potentials. At higher anode potentials, when abnormal extracting electrode ion currents appear, collector current drops to very low values and remains almost constant with further increase of accelerating voltage. Collector to extracting electrode current ratio (i_c/i_{ex}), which normally increases with voltage, is in this case very low and remains practically unchanged.

Table 2 gives usual running parameters used for the separation of isotopes.

TABLE 2

El-ement	Isotopes collected	i_a A	U_a V	U_{ex} kV	i_c mA	i_{ex} mA
Mg	24, 25, 26	2.0	70	30	6.2	1.0
Zn	64, 66, 68	2.3	60	41	3.7	1.2
Cd	110, 112, 113, 114	1.5	60	50	4.4	0.5

The finding of optimal running conditions is not always easy as higher yields at the collector are followed by the widening of collector image and the deterioration of the resolving power at the collector. Retention of the separated isotopes

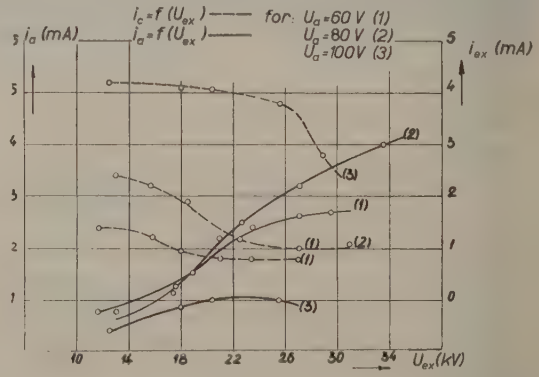

Fig. 8. Dependence of collector and extracting electrode current on accelerating voltage.

in the collector pockets is generally low because of the intense reevaporation and sputtering of the collected quantities. Good collection is also difficult because of the moving of the focus location of separated isotopes on the collector during the operation. Maximal collected quantity in one separation run was 4 mg Mg and 2.1 mg Zn.

This separator is intended to give the separated isotopes, required for scientific research in

our Institutes. The future work develops with the aim to ameliorate working conditions of the machine with heavier elements and with elements of low vapor pressure.

The references [1–16]) give information about other electromagnetic isotope separators.

Acknowledgment

We would like to express our thanks to Dr Pavle Savić and Dr Robert Walen for the encouragement and valuables suggestions during this work. The help of Ing. Jovičić Z. and technicians, late Petrović S., Josimov G., Cvjetan M., Cvjetan R., and Marković T. in designing and mounting of the machine was very valuable. We thank also to Mrs. Čobić Branka for experimental aid in the preparation and analysis of the samples. In the same time we acknowledge the members of the workshops for the unselfish effort in the construction and handling of parts of the separator.

REFERENCES

[1]) O. Almén, G. Bruce and A. Lundén, Nuclear Instruments **2** (1958) 249.

[2]) G. Andersson, Arkiv f. Fysik **12** (1957) 331.

[3]) J. Bergström, S. Thulin, N. Svartholm and K. Siegbahn, Arkiv f. Fysik **1** (1949) 281.

[4]) R. Bernas, J. Phys. Rad. **14** (1953) 34.

[5]) R. Bernas, Thèse, Paris (1954).

[6]) Ch. Cassignol, Proc. Symp. Isotop. Sep. Amsterdam, 1957 (North-Holland Publishing Co., Amsterdam, 1958) p. 631.

[7]) R. H. Dawton, Proc. Conf. Electromagn. Enr. Isot. & Mass-spectrom. Harwell (London, 1956) p. 208.

[8]) R. H. Dawton and M. L. Smith, Rev. Chem. Soc. **9** (1955) 1.

[9]) C. P. Keim, Ann. Rev. Nucl. Sci. **1** (1952) p. 263.

[10]) J. Koch, Mass spectr. Phys. Research (1953) p. 165.

[11]) J. Koch, Proc. Conf. Electrom. Enr. Isot. & Mass-spectrom. Harwell (London, 1956) p. 214.

[12]) C. E. Normand, Proc. Conf. Electrom. Enr. Isot. & Mass-spectrom. Harwell (London, 1956) p. 197.

[13]) K. O. Nielsen and O. Skilbreid, Nuclear Instruments **2** (1958) 15.

[14]) M. L. Smith, Prog. Nucl. Phys. **6** (1957) 163.

[15]) S. Thulin, Thesis, Uppsala (1954).

[16]) C. J. Zilverschoon, Thesis, Amsterdam (1954).

NUCLEAR INSTRUMENTS 3 (1958) 250–259; NORTH-HOLLAND PUBLISHING CO. – AMSTERDAM

MASSENSPEKTROGRAPHEN MIT DOPPELFOKUSSIERUNG ERSTER ORDNUNG FÜR ALLE MASSEN, DIE GERINGE BILDFEHLER IN EINEM GROSSEN MASSENBEREICH ENTLANG DER PHOTOPLATTE AUFWEISEN

H. HINTENBERGER und L. A. KÖNIG

Max-Planck-Institut für Chemie, Mainz

Received 10 August 1958

The properties of the aberration coefficients of the mass spectrographs with first order double focusing along a straight image line are examined, of which in a previous paper[6]) was shown that in one point of the image line two or three of the aberration coefficients are zero. It results that for some of these instruments, besides the mentioned advantages, further improvements are possible. There exist not only instruments in which some aberration coefficients vanish in additional points at the photographic plate, but also instruments with small aberration coefficients in a wide range of the plate. The dimensions of especially favourable mass spectrographs are given in a table, the progress of the aberration coefficients belonging to them is shown in diagrams and the positions of the zero points of the coefficients are indicated in a table.

1. Einleitung und Problemstellung

Nach der Berechnung der Koeffizienten der vom Öffnungswinkel α und der relativen Geschwindigkeitsabweichung $\beta = \Delta v/v$ quadratisch abhängigen Bildfehler in Massenspektrometern und Massenspektrographen, die aus einem elektrischen Radialfeld und einem dahintergeschalteten magnetischen Ablenkfeld bestehen[1]), sind in früheren Arbeiten eine grosse Zahl von Massenspektrometern[2,3,4]) angegeben worden, die vollständige Doppelfokussierung zweiter Ordnung für die beobachtete Masse zeigen. Auch Massenspektrographen, die Doppelfokussierung erster Ordnung für alle Massen entlang einer geraden Photoplatte aufweisen und für die an einer Stelle der Photoplatte ein, zwei oder auch alle drei Koeffizienten der von α^2, $\alpha\beta$ und β^2 abhängigen Bildfehler verschwinden, haben wir beschrieben[5,6]). In dieser Arbeit soll gezeigt werden, dass in solchen Massenspektrographen niedrige Werte für die Bildfehlerkoeffizienten in einem weiten Bereich der Photoplatte erreicht werden können. Es ist auch möglich, an mehreren Stellen der Photoplatte Bildfehlerkoeffizienten Null zu machen und unter günstigen Umständen sogar manche Koeffizienten über einen weiten Bereich der Photoplatte praktisch zum Verschwinden zu bringen.

2. Zur Berechnung der Bildfehlerkoeffizienten entlang der photographischen Platte

Die Ordinate y_B, mit der der Nebenstrahl mit einem Öffnungswinkel α und einer Geschwindigkeitsabweichung β auf einen senkrecht zum Hauptstrahl durch den Gaussschen Bildpunkt gehenden Schirm *Sch* auftrifft (siehe Abb. 1) ist in allen Massenspektrographen der oben definierten Art durch den Ansatz[1]) darstellbar:

$$y_B = r_m \{B_{11}\,\alpha^2 + B_{12}\,\alpha\beta + B_{22}\,\beta^2\}, \qquad (1)$$

wobei B_{11} den Koeffizienten des Öffnungsfehlers, B_{12} den Koeffizienten der gemischt

[1]) H. Hintenberger und L. A. König, Z. Naturforsch. **12a** (1957) 140.

[2]) H. Hintenberger und L. A. König, Z. Naturforsch. **12a** (1957) 443.

[3]) H. Hintenberger und L. A. König, Z. Naturforsch. **12a** (1957) 773.

[4]) H. Hintenberger und L. A. König, Z. Naturforsch. **13a** (1958) 236.

[5]) H. Hintenberger, H. Wende und L. A. König, Z. Naturforsch. **10a** (1955) 344.

[6]) L. A. König und H. Hintenberger, Nuclear Instruments **3** (1958) 133.

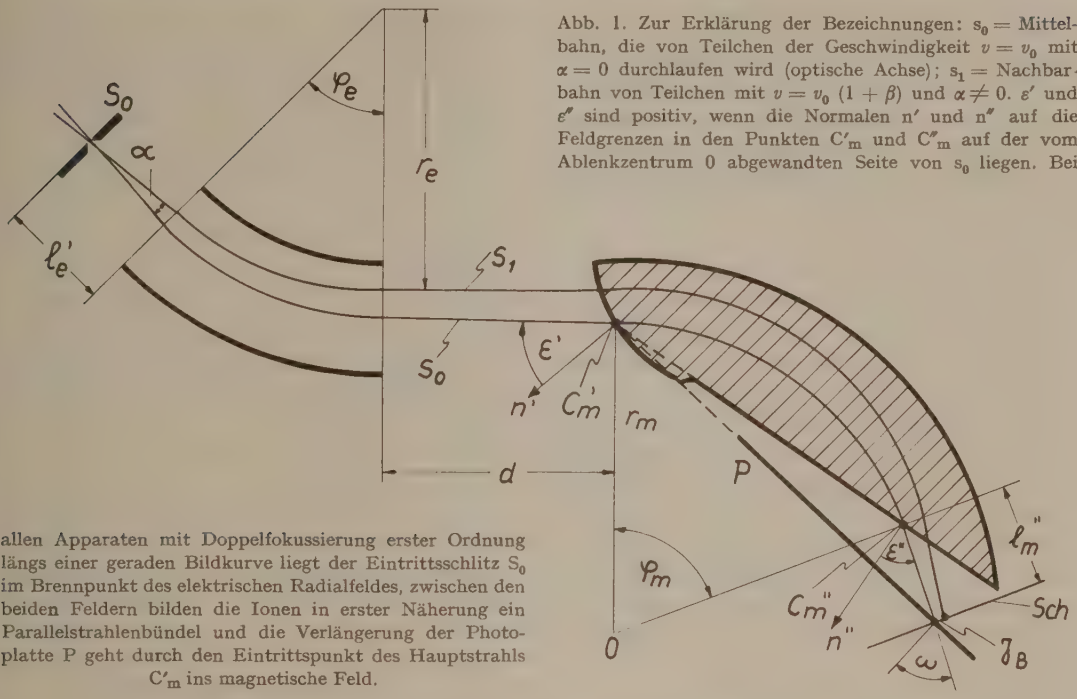

Abb. 1. Zur Erklärung der Bezeichnungen: s_0 = Mittelbahn, die von Teilchen der Geschwindigkeit $v = v_0$ mit $\alpha = 0$ durchlaufen wird (optische Achse); s_1 = Nachbarbahn von Teilchen mit $v = v_0\,(1+\beta)$ und $\alpha \neq 0$. ε' und ε'' sind positiv, wenn die Normalen n' und n'' auf die Feldgrenzen in den Punkten C'_m und C''_m auf der vom Ablenkzentrum 0 abgewandten Seite von s_0 liegen. Bei allen Apparaten mit Doppelfokussierung erster Ordnung längs einer geraden Bildkurve liegt der Eintrittsschlitz S_0 im Brennpunkt des elektrischen Radialfeldes, zwischen den beiden Feldern bilden die Ionen in erster Näherung ein Parallelstrahlenbündel und die Verlängerung der Photoplatte P geht durch den Eintrittspunkt des Hauptstrahls C'_m ins magnetische Feld.

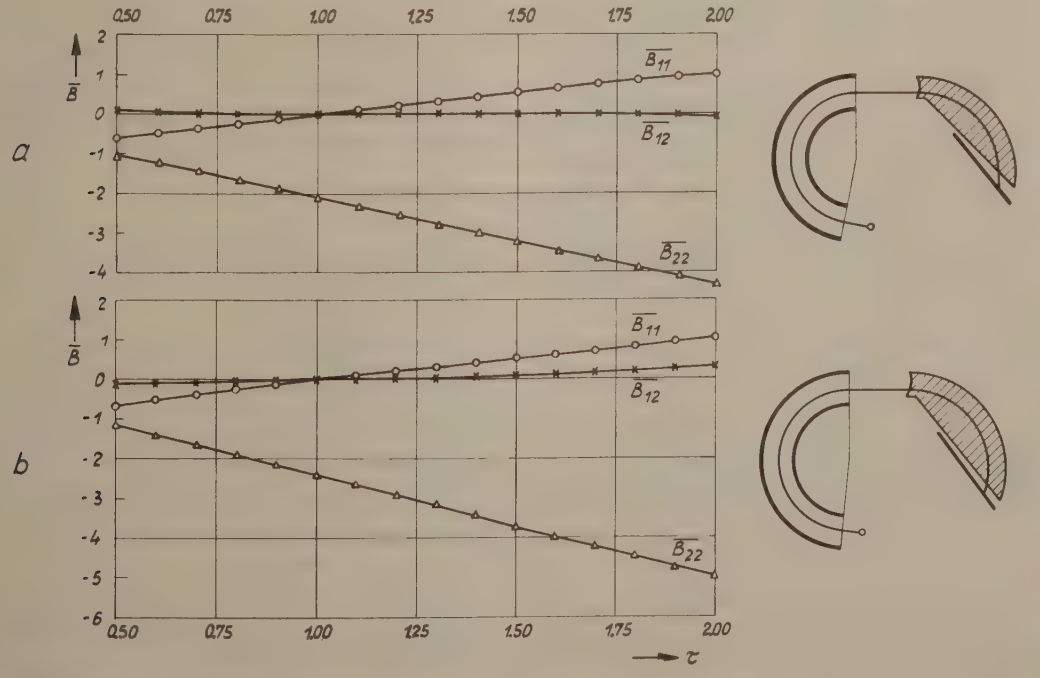

Abb. 2. Die Bildfehlerkoeffizienten $\bar{B}_{ik}$ in Abhängigkeit von $\tau = r_m/r_{m_0}$ für die Apparate No. I und IV der Tab. 1 dieser Arbeit. Die genauen Abmessungen dieser Apparate können aus Tab. 1, die Nullstellen τ_1^{ik} und τ_2^{ik} der Bildfehlerkoeffizienten aus Tab. 2 entnommen werden.

öffnungswinkel- und geschwindigkeitsabhängigen Aberration und B_{22} den Koeffizienten der rein geschwindigkeitsabhängigen Aberration bedeutet. Diese Koeffizienten sind von den Ablenkwinkeln im elektrischen und magnetischen Feld, vom Ein- und Austrittswinkel des Hauptstrahls am Magnetfeld, vom Abstand der Felder, vom Verhältnis der Bahnradien im elektrischen und im magnetischen Feld und von den Krümmungsradien der Feldgrenzen abhängig. Wir können die umfangreichen Formeln zur Berechnung dieser Koeffizienten hier nicht wiederholen und verweisen auf unsere früheren Arbeiten[1,3,6]). In diesen Formeln wurde der Krümmungsradius r_m der Hauptbahn s_0 im homogenen Magnetfeld als Längeneinheit benutzt. Um die Abbildungseigenschaften entlang der geraden Bildkurve in den hier behandelten Apparaten zu beschreiben ist es zweckmässig, Gl. (1) etwas abzuändern[7]). Wir führen eine dimensionslose Variable τ durch die Beziehung

$$\tau = \frac{r_m}{r_{m_0}} \tag{2}$$

ein†. Jetzt ist r_{m_0} die benutzte Längeneinheit, die im Prinzip willkürlich festgelegt werden kann, zweckmässig aber so gewählt wird, dass Teilchenbahnen mit dem Radius r_{m_0} im Magnetfeld auf die Mitte der Photoplatte oder einen anderen ausgezeichneten Punkt der Platte (z.B. auf einen Punkt mit korrigierten Bildfehlern) treffen. Jeder Punkt auf der Platte ist dann durch einen bestimmten τ-Wert gekennzeichnet. Für den Bezugspunkt ist $\tau = 1$. Wir definieren nun die Bildfehlerkoeffizienten etwas anders und schreiben den Ausdruck für y_B statt nach Gl. (1) in der Form

$$y_B = r_{w_0}\{\bar{B}_{11}\,\alpha^2 + \bar{B}_{12}\,\alpha\beta + \bar{B}_{22}\,\beta^2\}. \tag{3}$$

Zwischen den neuen Bildfehlerkoeffizienten $\bar{B}_{ik}$ der Gl. (3) und den früher definierten B_{ik} der Gl. (1) besteht der Zusammenhang

$$\bar{B}_{ik} = \tau \cdot B_{ik}\,. \tag{4}$$

Für die $\bar{B}_{ik}$ kann der Ansatz gemacht werden:

$$\bar{B}_{ik} = b_{-1}^{ik}\frac{1}{\tau} + b_0^{ik} + b_1^{ik}\,\tau \qquad (ik = 11, 12, 22)\,. \tag{5}$$

† Führt man statt r_m und r_{m_0} die Massen M und M_0 ein, so gilt $\tau = (M/M_0)^{\frac{1}{2}}$.

Die Grössen b_l^{ik} $(l = -1, 0, 1)$ sind vom Parameter τ, der die Lage der Massenlinien auf der Photoplatte angibt, unabhängig. Bezüglich ihrer Berechnung müssen wir wieder auf die früheren Arbeiten verweisen[7,1,3,6]).

In Abschnitt 3 werden für eine Reihe von Massenspektrographen die Bildfehlerkoeffizienten $\bar{B}_{ik}$ als Funktion des Parameters $\tau = r_m/r_{m_0}$ wiedergegeben.

Die Strahlbreite W_S und die Linienbreite auf der Photoplatte W_B können aus den Bildfehlerkoeffizienten und den Dimensionen und der Lage der Blenden in folgender Weise ermittelt werden.

Die Strahlenbreite ist gegeben durch

$$W_S = W_{S_0} + \Delta W_S \tag{6}$$

mit W_{S_0} = Strahlbreite in Gaussscher Näherung,

$\Delta W_S = y_{B,\max} - y_{B,\min}$,

die Breite der Massenlinien auf der Photoplatte durch:

$$W_B = \frac{W_S}{\cos\omega} = W_{B_0} + \Delta W_B \tag{7}$$

mit $$W_{B_0} = W_0 \cdot \tau \cdot \delta \left(\delta = \frac{r_{m_0}}{r_e}\,\frac{1 - \cos\varphi_m}{\cos\omega}\right)$$

und $$\Delta W_B = \Delta W_S/\cos\omega.$$

Dabei bedeutet ω den Winkel, den das Lot auf die Photoplatte mit der Einfallsrichtung des Strahls einschliesst und W_0 die Weite des Eintrittsschlitses S_0 (Siehe Abb. 1).

3. Ergebnisse

3.1.

Wir haben die Bildfehlerkoeffizienten $\bar{B}_{11}$, $\bar{B}_{12}$ und $\bar{B}_{22}$ entlang der Photoplatte für sämtliche, in den Tabellen 1 bis 7 unserer früheren Arbeit[6]) angegebenen Massenspektrographen, die an einer Stelle der Photoplatte korrigierte Bildfehler aufweisen, nach Gl. (5) numerisch berechnet. Von den erhaltenen Ergebnissen seien im folgenden einige typische Fälle, soweit sie für eine praktische Verwirklichung in Betracht kommen, zusammengestellt. Tab. 1 zeigt die genauen Daten der hier besprochenen Apparate. Die Nummern der dazugehörigen Abbildungen dieser Arbeit sind aus Spalte 2 dieser Tabelle zu entnehmen.

[7]) L. A. König und H. Hintenberger, Z. Naturforsch., im Druck.

In Tab. 2 sind die Nullstellen τ_1^{ik} und τ_2^{ik} der Bildfehlerkoeffizienten B_{ik} angegeben. Negative τ-Werte der Nullstellen sind physikalisch unbrauchbar und wurden in Klammern gesetzt. Man sieht, dass es Fälle gibt, wo ein Bildfehlerkoeffizient zwei Nullstellen auf der Photoplatte besitzt. magnetischen Feld, für die an einer Stelle der Photoplatte gleichzeitig $\bar{B}_{11}$ und $\bar{B}_{12}$ verschwinden. Diese beiden Apparate (No. I und No. IV in Tab. 1) besitzen vernünftige Abmessungen und haben zusätzlich die Eigenschaft, dass für sie in einem grossen Bereich der Photoplatte

Tabelle 1

Nr.	Abb.	φ_m	ε'	ε''	$\frac{r_{m0}}{R'}$	$\sqrt{2}\varphi_e$	φ_e	$\frac{d}{r_{m0}}$	$\frac{r_e}{r_{m0}}$	$\frac{l'_e}{r_{m0}}$	$\frac{l''_m}{r_{m0}}$	Literaturzitat No 6	
												Tab.	Nr.
I	2a	90	12.67	—45	—4.00	240	169.71	0.817	0.810	0.331	0.184	1	7
II	—	100	16.34	—40	—0.50	250	176.78	1.027	1.478	0.380	0.102	1	8
III	—	100	16.34	—40	—1.00	250	176.78	0.961	1.275	0.328	0.102	1	9
IV	2b	100	16.34	—40	—3.00	250	176.78	0.775	0.896	0.231	0.102	1	10
V	3a	150	—45.41	—15	—0.25	80	56.57	0.534	2.339	0.292	1.840	2	7
VI	3b	210	—25.57	15	—1.00	80	56.57	0.057	1.475	0.184	0.840	2	9
VII	—	90	11.27	—45	0.60	238	168.29	0.738	3.803	1.680	0.166	3	5
VIII	—	170	—23.93	— 5	0.75	210	148.49	2.611	1.442	1.766	2.981	4	4
IX	—	170	—23.93	— 5	2.00	210	148.49	1.725	0.886	1.085	2.981	4	5
X	—	190	—15.04	5	3.00	210	148.49	1.609	0.778	0.953	2.633	4	7
XI	4	190	—24.62	5	1.00	230	162.63	1.920	1.394	0.827	1.658	4	8
XII	—	90	0	—45	2.00	45	31.82	1.628	2.412	1.706	0	5	2
XIII	5a	90	0	—45	2.50	45	31.82	1.009	2.184	1.545	0	5	3
XIV	—	90	0	—45	3.00	45	31.82	0.711	2.011	1.422	0	5	4
XV	5b	90	0	—45	3.50	45	31.82	0.539	1.873	1.325	0	5	5
XVI	—	90	0	—45	4.00	45	31.82	0.427	1.761	1.245	0	5	6
XVII	5c	90	0	—45	4.50	45	31.82	0.350	1.666	1.178	0	5	7
XVIII	6a	90	20.10	—45	3.00	75	53.03	0.613	0.799	0.151	0.268	6	3
XIX	—	90	22.24	—45	3.00	85	60.10	0.658	0.556	0.034	0.290	6	4
XX	—	90	20.10	—45	4.00	75	53.03	0.478	0.686	0.130	0.268	6	7
XXI	6b	90	22.24	—45	4.00	85	60.10	0.530	0.479	0.030	0.290	6	8
XXII	7a	123.75	—42.57	—28.13	0.50	205	144.96	1.898	1.328	2.014	3.434	7	3
XXIII	7b	145.94	—38.78	—17.03	0.40	220	155.56	1.744	1.961	1.652	2.571	7	4
XXIV	7c	151.72	—43.03	—14.14	0.50	245	173.24	1.241	1.757	0.579	1.941	7	5

Tab. 1. Zusammenstellung der genauen Daten von Massenspektrographen mit Doppelfokussierung erster Ordnung für alle Massen entlang einer geraden Photoplatte, bei denen ausserdem noch an verschiedenen Stellen der Photoplatte manche oder alle der Bildfehlerkoeffizienten $\bar{B}_{ik}$ verschwinden und auch in grösseren Gebieten der Platte niedrige Werte aufweisen. Die Bedeutung der einzelnen Grössen ist aus Abb. 1 zu ersehen. In Spalte 2 sind die Nummern der Abbildungen angegeben, aus denen der Verlauf der Bildfehlerkoeffizienten entlang der Photoplatte für besonders günstige Apparate zu ersehen ist. (Aus den Spalten 13 und 14 sind die genauen Angaben zu entnehmen, wo der betreffende Apparat in der früheren Arbeit behandelt wurde.) Die Apparate I bis VII besitzen gleichsinnige, die übrigen gegensinnige Ablenkung in den beiden Feldern.

3.2. GLEICHSINNIGE ABLENKUNG

3.2.1. Die Abb. 2a und b zeigen das Verhalten der Bildfehlerkoeffizienten von zwei Massenspektrographen mit Doppelfokussierung erster Ordnung längs einer geraden Bildkurve bei gleichsinniger Ablenkung im elektrischen und $\bar{B}_{12}$ fast verschwindet, während die übrigen Bildfehlerkoeffizienten, insbesondere $\bar{B}_{11}$ im Bereich $0.5 < \tau < 2.0$, verhältnismässig klein sind im Vergleich zu unkorrigierten Apparaten†.

† Für Apparate vom Mattauch-Herzogschen Typ[9]) z.B. variiert $\bar{B}_{11}$ im gleichen τ-Intervall zwischen —5 und

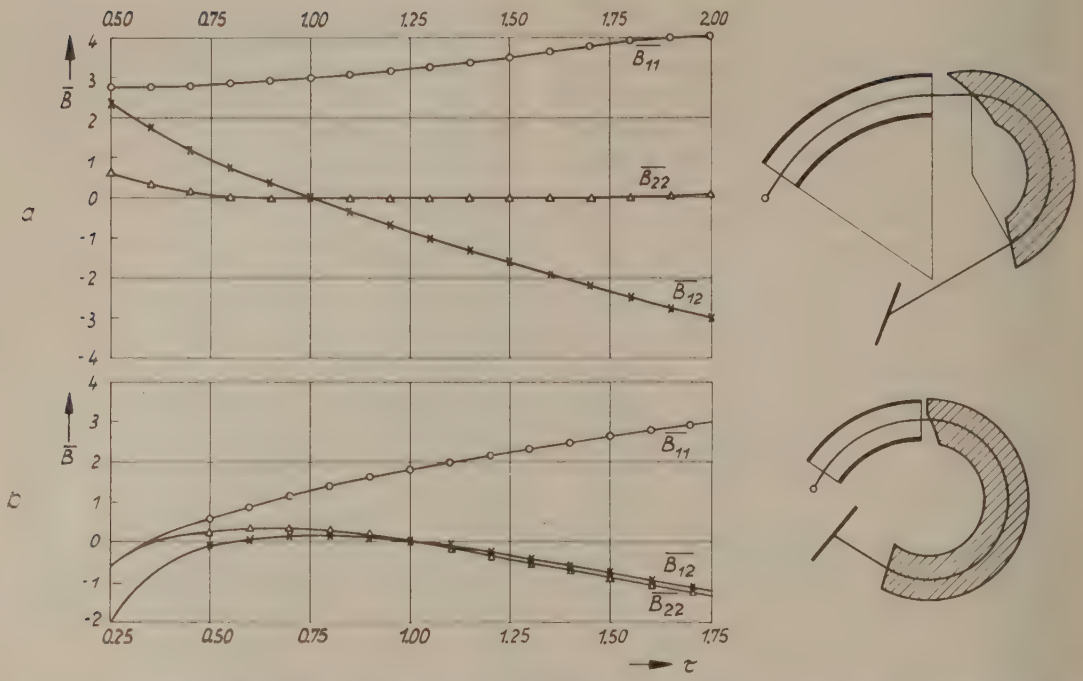

Abb. 3. Die Bildfehlerkoeffizienten $\overline{B}_{ik}$ in Abhängigkeit von $\tau = r_m/r_{m0}$ für die Apparate No. V und VI der Tab. 1 dieser Arbeit. Die genauen Abmessungen der Apparate können aus Tab. 1, die Lage der Nullstellen τ_1^{ik} und τ_2^{ik} der Bildfehlerkoeffizienten aus Tab. 2 entnommen werden.

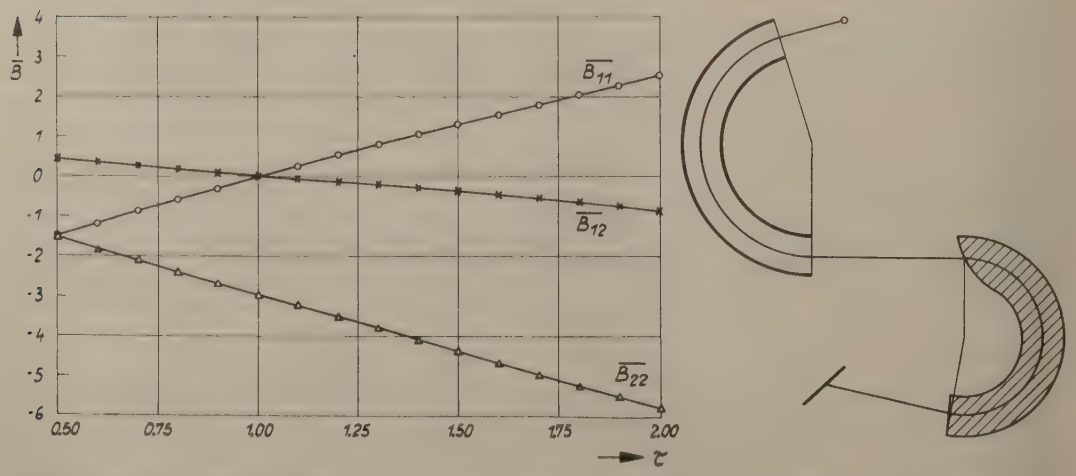

Abb. 4. Die Bildfehlerkoeffizienten $\overline{B}_{ik}$ in Abhängigkeit von $\tau = r_m/r_{m0}$ für Apparat No. XI der Tab. 1. Auch bei den Apparaten VIII, IX und X der Tab. 1 verhalten sich die $\overline{B}_{ik}$ sehr ähnlich.

Für die beiden weiteren, in der Tab. 1 angeführten Massenspektrographen dieser Art (Apparat No. II und Apparat No. III) ist der Verlauf der Bildfehlerkoeffizienten den in den Abb. 2a und b gezeigten Diagrammen so ähnlich, dass wir auf eine Wiedergabe eigener Figuren für diese Apparate verzichten.

3.2.2. Die Abb. 3a und b zeigen den Verlauf der Bildfehlerkoeffizienten entlang der Photoplatte für zwei Apparate (No. V und VI, Tab. 1), bei denen an einer Stelle der Platte $\bar{B}_{12} = \bar{B}_{22} = 0$ ist. Während in Apparat No. V $\bar{B}_{22}$ zwischen $\tau = 0.8$ und $\tau = 2.0$ praktisch verschwindet und auch die beiden anderen Koeffizienten im

Tabelle 2

Nr.	Abb.	$\tau_1^{(11)}$	$\tau_2^{(11)}$	$\tau_1^{(12)}$	$\tau_2^{(12)}$	$\tau_1^{(22)}$	$\tau_2^{(22)}$
				gleichsinnige Ablenkung			
I	2a	1.000	(—0.161)	4.394×10^5	1.000	—	—
II	—	1.000	(—0.656)	1.766	1.000	—	—
III	—	1.000	(—0.488)	1.067	1.000	—	—
IV	2b	1.000	(—0.241)	1.000	0.299	—	—
V	3a	—	—	1.000	(—0.498)	1.630	1.000
VI	3b	0.354	(—1.149)	1.000	0.533	1.000	0.358
VII	—	1.000	(—3.779)	1.000	(—169.62)	3.955	1.000
				gegensinnige Ablenkung			
VIII	—	1.000	(—0.010)	1.000	(—0.017)	—	—
IX	—	1.000	(—0.004)	1.000	(—0.005)	(—0.011)	(—0.103)
X	—	1.000	(—0.022)	1.000	(—0.027)	—	—
XI	4	1.000	(—0.149)	1.000	(—0.165)	—	—
XII	—	0.451	(—4.557)	1.749	1.000	6.978	1.000
XIII	5a	0.368	(—4.578)	1.119	1.000	3.482	1.000
XIV	—	0.311	(—4.593)	1.000	0.812	2.165	1.000
XV	5b	0.269	(—4.604)	1.000	0.633	1.514	1.000
XVI	—	0.237	(—4.613)	1.000	0.516	1.138	1.000
XVII	5c	0.212	(—4.620)	1.000	0.434	1.000	0.899
XVIII	6a	0.116	(—0.745)	1.000	0.206	1.000	0.290
XIX	—	0.077	(—0.388)	1.000	0.131	1.000	0.171
XX	—	0.090	(—0.709)	1.000	0.144	1.000	0.192
XXI	6b	0.060	(—0.367)	1.000	0.093	1.000	0.117
XXII	7a	1.000	0.257	1.000	0.732	1.009	(—0.863)
XXIII	7b	1.000	0.247	1.000	0.956	1.000	(—0.513)
XXIV	7c	1.000	0.131	1.000	(—0.893)	1.007	(—0.101)

Nullstellen τ_1^{ik} und τ_2^{ik}, an denen die Bildfehlerkoeffizienten $\bar{B}_{ik}$ auf der Photoplatte für die unter der gleichen römischen Ziffer in Tab. 1 angegebenen Massenspektrographen verschwindet.

$+ 2.5\,\bar{B}_{12}$ und $\bar{B}_{22}$ für die gebräuchlichen d-Werte zwischen —2 und —25. Beim Reuterswärdschen Apparat[10]) nehmen die Bildfehlerkoeffizienten noch viel grössere Werte an[7]).

[8]) Ch. F. Robinson, Rev. Sci. Instr. **28** (1957) 777.
[9]) J. Mattauch und R. Herzog, Z. Phys. **89** (1934) 786.
[10]) C. Reuterswärd, Ark. Mat. Astr. Fys. **30a** (1943) No. 7.

gleichen Bereich nicht sehr gross werden, bleiben für den Apparat No. VI im Bereich zwischen $\tau = 0.3$ und $\tau = 1.1$ alle drei Bildfehlerkoeffizienten sehr klein. In diesem Intervall verschwindet, wie aus Tab. 2 entnommen werden

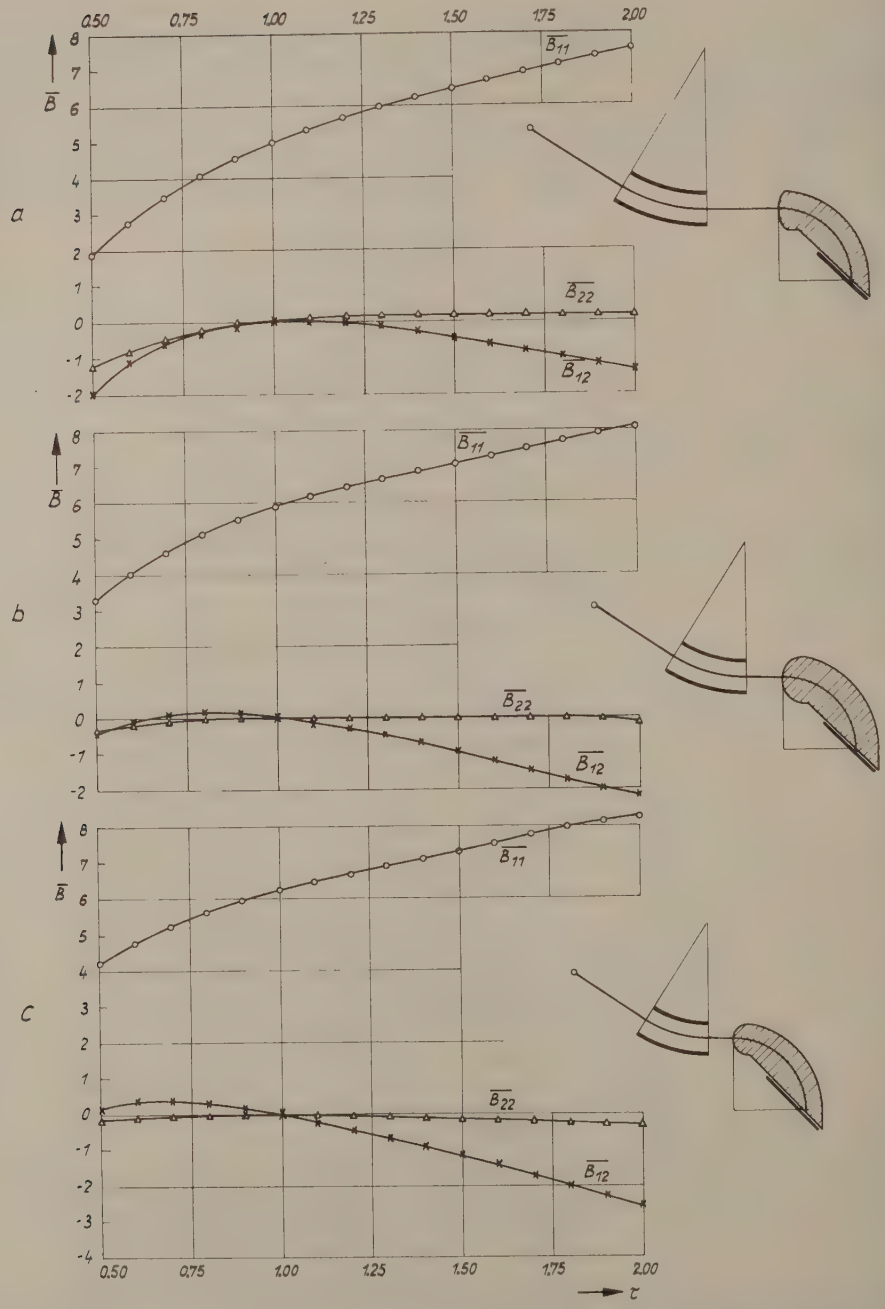

Abb. 5. Die Bildfehlerkoeffizienten $\overline{B}_{ik}$ in Abhängigkeit von $\tau = r_m/r_{m0}$ für Apparate vom Mattauch-Herzogschen Typ, bei denen die Eingangsgrenze des Magnetfeldes so gekrümmt wurde, dass an einer Stelle der Photoplatte (für $\tau = 1$) $\overline{B}_{12}$ und $\overline{B}_{22}$ verschwinden. Wie man sieht, existieren Apparate dieser Art, für die in einem weiten Bereich um die Nullstelle $\overline{B}_{12}$ nur sehr kleine Werte annimmt und $\overline{B}_{22}$ im gleichen Bereich naheser verschwindet. (Apparate No. XIII, XV und XVII der Tab. 1).

kann, $\bar{B}_{22}$ an zwei, $\bar{B}_{12}$ auch an zwei und $\bar{B}_{11}$ an einer Stelle. Insgesamt liegen also im angegebenen Intervall auf der Photoplatte 5 Nullstellen der Bildfehlerkoeffizienten, wobei zwei davon zusammenfallen. Trotz des fast in sich geschlossenen Strahlverlaufs ist der praktische Bau solcher Instrumente durchaus möglich, zumal durch leichte Abänderungen der hier angegebenen Winkel und Abmessungen im Rahmen der Korrekturbedingungen der Apparat für den praktischen Bau noch günstiger gestaltet werden kann, ohne den Verlauf der Bildfehlerkoeffizienten wesentlich zu verändern.

3.3. GEGENSINNIGE ABLENKUNG

3.3.1. Für Massenspektrographen mit $\bar{B}_{11} = \bar{B}_{12} = 0$ an einer Stelle der Photoplatte haben wir für 4 Beispiele (Apparate No. VIII–XI der Tab. 1) den Verlauf der Bildfehlerkoeffizienten als Funktion von $\tau = r_m/r_{m_0}$ angegeben. Abb. 4 zeigt als typisches Beispiel die Verhältnisse bei Apparat No. XI der Tab. 1. Die Bildfehlerkoeffizienten zeigen auch bei den drei anderen Apparaten einen der Abb. 4 sehr ähnlichen Verlauf.

3.3.2. Die Abb. 5a, b und c zeigen den Verlauf von $\bar{B}_{11}$, $\bar{B}_{12}$ und $\bar{B}_{22}$ entlang der Photoplatte

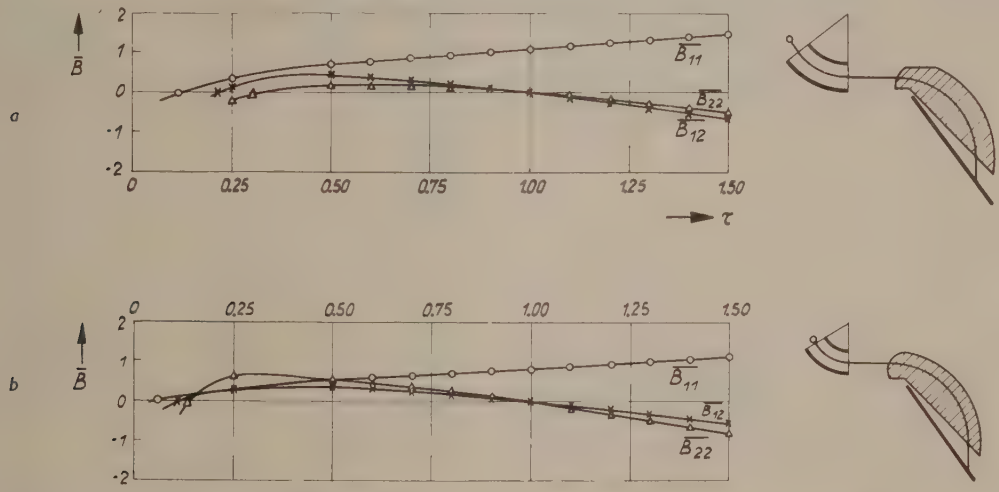

Abb. 6. Die Bildfehlerkoeffizienten $\bar{B}_{ik}$ in Abhängigkeit von $\tau = r_m/r_{m_0}$ für die Apparate No. XVIII und XXI der Tab. 1 Im Bereich zwischen $\tau = 0.1$ und 1.1 liegen fünf Nullstellen der Bildfehlerkoeffizienten, wobei für $\tau = 1$ zwei Nullstellen zusammenfallen. Die genauen Werte der Nullstellen können aus Tab. 2 entnommen werden.

3.2.3. Wir haben den Verlauf der Bildfehlerkoeffizienten auch in Apparaten, die vollständige Doppelfokussierung zweiter Ordnung an einer Stelle der Photoplatte zeigen ($\bar{B}_{11} = \bar{B}_{12} = \bar{B}_{22} = 0$ für $\tau = 1$) berechnet, dabei jedoch im Vergleich zu weiter unten angeführten Instrumenten keine sehr günstigen Verhältnisse gefunden. Bei diesen Apparaten wachsen die Bildfehlerkoeffizienten mit dem Abstand von der korrigierten Stelle sehr rasch an. Diese Instrumente besitzen auch ein unverhältnismässig grosses elektrisches Radialfeld (siehe Tab. 1 App. No. VII).

für Massenspektrographen vom Mattauch-Herzogschen Typ (Apparate No. XIII, XV, XVII der Tab. 1), bei denen die Krümmung der Eintrittsgrenze des Magnetfeldes und der Abstand der beiden Felder d/r_{m_0} so günstig gewählt wurden, dass $\bar{B}_{12}$ und $\bar{B}_{22}$ für $\tau = 1$ verschwinden†. Die Abbildungen zeigen, dass bei ihnen der Bildfehlerkoeffizient $\bar{B}_{22}$ entlang eines weiten

† Dass für Apparate vom Mattauch-Herzogschen Typ die Bildfehlerkoeffizienten durch geeignete Wahl der Krümmung der Eintrittsfeldgrenze und des Feldabstandes d/r_{m_0} Null gemacht werden können, hat bereits Robinson [8]) durch Anwendung unserer allgemeinen Formeln gezeigt, bevor wir diese Apparate genauer behandelt haben[6]).

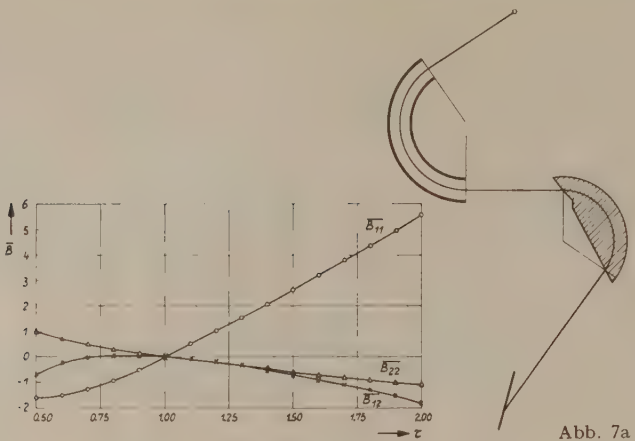

Abb. 7a

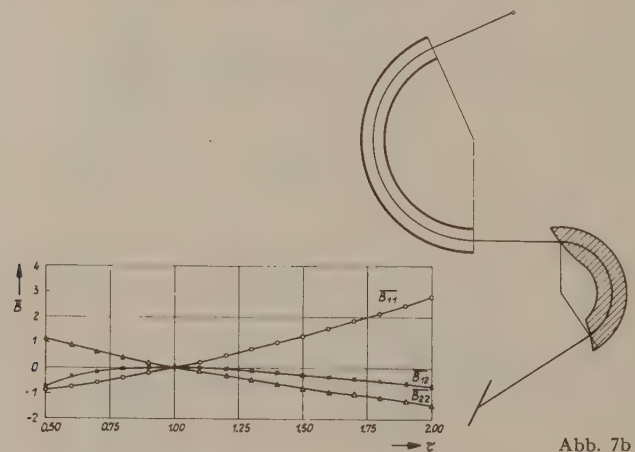

Abb. 7b

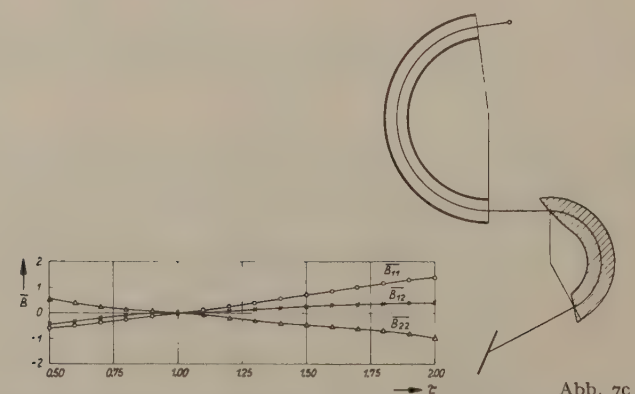

Abb. 7c

Abb. 7. Die Bildfehlerkoeffizienten $\overline{B}_{ik}$ in Abhängigkeit von $\tau = r_m/r_{m_0}$ für verschiedene Massenspektrographen, die Doppelfokussierung erster Ordnung für alle Massen und vollständige Doppelfokussierung zweiter Ordnung an einer Stelle der Photoplatte zeigen.

($\overline{B}_{11} = \overline{B}_{12} = \overline{B}_{22} = 0$ für $\tau = 1$). Abb. 7a gilt für Apparat No. XXII, 7b für Apparat No. XXIII und 7c für Apparat XXIV der Tab. 1.

Bereiches der Photoplatte fast zum Verschwinden gebracht und $\bar{B}_{12}$ im gleichen Bereich ziemlich klein gehalten werden kann. Dieser günstige Verlauf der Koeffizienten $\bar{B}_{12}$ und $\bar{B}_{22}$ muss allerdings mit einer Vergrösserung des Koeffizienten $\bar{B}_{11}$ erkauft werden, der in dem für $\bar{B}_{12}$ und $\bar{B}_{22}$ günstigen Bereich keine Nullstelle mehr aufweist. Der Öffnungsfehler hat aber, wie wir an anderer Stelle zeigen konnten[7]), keinen sehr grossen Einfluss auf die wirkliche Bildbreite in Apparaten vom Mattauch-Herzogschen Typ.

Geht man mit der Photoplatte aus dem Magnetfeld heraus, so ist der Verlauf von $\bar{B}_{22}$ nicht mehr ganz so extrem günstig wie im modifizierten Mattauch-Herzogschen Fall, dafür wird aber der Koeffizient des Öffnungsfehlers $\bar{B}_{11}$ kleiner, so dass in einem ziemlich weiten Bereich der Photoplatte alle 3 Bildfehlerkoeffizienten klein sind. Die Abb. 6a und b zeigen den Verlauf der Bildfehlerkoeffizienten $\bar{B}_{ik}$ als Funktion von $\tau = r_m/r_{m0}$ für die Apparate XVIII und XXI der Tab. 1.

3.3.3. Die Abb. 7a, b und c zeigen den Verlauf der Bildfehlerkoeffizienten für die drei Apparate No. XXII, XXIII und XXIV der Tab. 1, für die an einem Punkt der Photoplatte vollständige Doppelfokussierung zweiter Ordnung erreicht wird. ($\bar{B}_{11} = \bar{B}_{12} = \bar{B}_{22} = 0$ für $\tau = 1$). Wie der Vergleich der drei Abbildungen zeigt, muss der günstige Verlauf der Bildfehlerkoeffizienten entlang der Photoplatte durch ein verhältnismässig grosses Radialfeld und einen grossen Eintrittswinkel ε' erkauft werden.

NUCLEAR INSTRUMENTS 3 (1958) 260–264; NORTH-HOLLAND PUBLISHING CO. – AMSTERDAM

EIN BESONDERS EINFACHER STROMSTABILISATOR HÖCHSTER QUALITÄT FÜR ELEKTROMAGNETE

BRANKO BERKEŠ

Institut "Rudjer Bošković", Zagreb

Received 6 July 1958

A type of current stabilizer for magnet, used in nuclear magnetic resonance experiments (fig. 3), is described. A high dynamic stability (1:20 000 at 1.6 A, input voltage variations ± 5%, load variations 10%) is obtained using a diode with a wolfram filament, which represents a stage with an extremely high amplification in the feedback loop. A high thermal stability is provided by means of a diode which is practically insensitive to normal room temperature changes, as it is evident from eq. (3).

In spite of a relatively high time constant of the heater filament—in connection with fig. 3—owing to the great inductance of the magnet, it is possible to obtain a very quick answer to sudden changes of input voltage.

Measurements were made with a precision potentiometer of an accuracy 1:100 000 and results agree within 20% with theoretical considerations.

1. Einleitung

Die besprochene Stabilisierungsapparatur wird als Stromquelle für einen Elektromagnet für Kernresonanzuntersuchungen verwendet. Die benötigte dynamische Stabilität (Netzspannungsänderung ± 5%, Laständerung 10%) und zeitliche Schwankungen (30 Minuten) des Stromes sollen nicht grösser als 1:20 000 sein und es ergibt sich schon invorhinein die Frage, auf welcher Art die hohen Werte der Stabilität, besonders hinsichtlich der Zeitkonstanz des Gerätes, am einfachsten zu erreichen sind.

In der Literatur findet man häufig Beschreibungen von Stromstabilisatoren, die von speziellen Zerhackern (Brown-converter oder dergleichen) gebrauch machen. Dadurch entfällt zwar der Gleichspannungsverstärker als ein Element der den zeitlichen Veränderungen am grössten unterliegt, doch muss man dann eine Wechselspannungsverstärkerstufe mit hoher Verstärkung einbauen, damit die kleinen Spannungsdifferenzen—die dem Zerhacker zugeführt werden—auf benötigte Grösse verwandelt werden können. Eigentlich ist die Stabilität in diesem Fall durch Grenzempfindlichkeit des Zerhackers und Stabilität der Vergleichsspannung und Referenzwiderstandes bedingt.

Obwohl die Benutzung von Zerhackern sicherlich einige gewisse Vorteile bietet, schien uns noch besser, als Stromindikator eine Diode im Sättigungsgebiet zu verwenden, die—wie weiter ausführlich beschrieben wird—eine ausserordentliche Stabilität gegenüber der Aussentemperaturschwankungen zeigt. Die Diode selbst besitzt auch sehr hohe Verstärkung, wodurch in meisten Fällen weitere Verstärkerstufen unnötig sind. Bei sehr grossen Anforderungen—wie bei dem besprochenen Magnet—konnte durch Beifügung einer einfachen Gleichspannungsverstärkerstufe auch reichlich hohe dynamische Stabilität erzielt und trotzdem die benötigte Elementenzahl auf Minimum zurückgeführt werden.

2. Die Diode

Zur Verfügung steht uns die bekannte Diode 29Cl der Firma Siemens Edison Swan Ltd. Aus den Kennlinien $I_a - U_a$ und $I_a - I_h$ (Bild 1) konnte—unter Berücksichtigung hoher Lebensdauer der Röhre—entnommen worden, dass der günstigste Arbeitspunkt bei ungefähr $U_{h0} =$ 3 V, $I_{h0} = 0.7$ A und $T_{k0} = 2000°$ K liegt. Theoretisch hat die Röhre dann eine Lebensdauer von einigen hunderttausend Arbeitsstunden, was unbedingt zu dem Entschluss führt, dass während eines Messexperimentes

(1–2 Tage) der Heizstrom (der zugleich auch der stabilisierte Strom ist) der Diode nur den geringsten Änderungen—die noch weit unter der benötigten Stabilitätsgrösse sind— unterworfen wird.

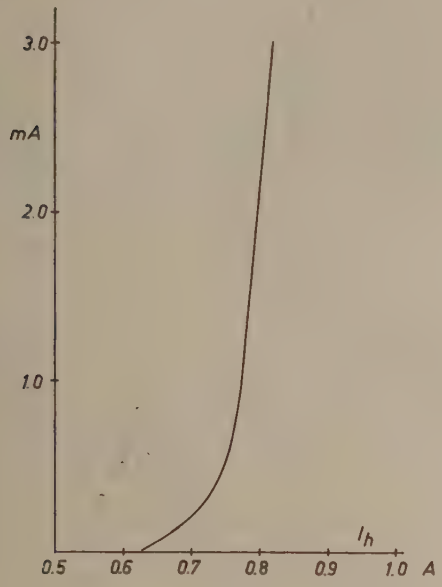

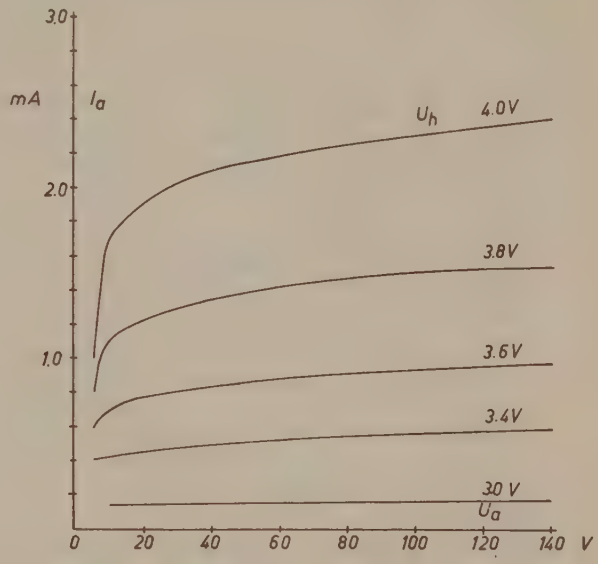

Bild 1. Heiz- und Anodenstromkennlinien der Diode 29Cl.

Die Diode befindet sich in der Brückenschaltung (Bild 2), wobei der stabilisierte Strom—wie erwähnt—gleichzeitig der Heizstrom der Diode ist. Nach einfachen theoretischen Überlegungen[1]) ergibt sich für den Stromverstärkungsfaktor

$$a_i = \frac{\mathrm{d}U_a}{\mathrm{d}I_h} = \frac{(1-\gamma)\,U_b}{I_{h0}} \cdot \frac{2 + b/T_{k0}}{2 - \alpha/2} \cdot \xi$$

$$\xi = \frac{R_i}{R_i + R_a} \qquad \gamma = \frac{R_1}{R_1 + R_2} \qquad \alpha = 1.195 \qquad (1)$$

wobei die verschiedene Bezeichnungen aus dem Bild 2 leicht zu ersehen sind. Mit $U_b = 500$ V, $\gamma = 1/5$, $R_a = 2$ MOhm und $\xi = 0.72$ ist die Verstärkung der Diode $a_i = 8300$.

Wir wollen jetzt verschiedene Einflüsse auf die Stabilität des Heizstromes untersuchen. Diese können wir in drei Hauptgruppen unterteilen und zwar: (a) Aussentemperaturschwankungen, (b) Schwankungen der Spannung zur Speisung der Diode und (c) Änderungen des Anodenwiderstandes.

(a) Unter Voraussetzung dass die Temperaturänderungen nur durch Strahlung in das Innern der Diode eindringen können und dass keine Wärme-Reflexion und Absorption am Glaskolben entstehen, dürfen wir schreiben

$$\mathrm{d}\,(\sigma \cdot e_{tb} \cdot T_b^4) = \mathrm{d}\,(\sigma \cdot e_{ta} \cdot T_{av}^4)$$

wo $\sigma = 5.673 \times 10^{-12}$ W·°K^{-4}·cm^{-2} die bekannte Stephan-Boltzmannsche Konstante und e_{tb}, e_{ta}, T_b und T_{av} die Emissionskoeffizienten und die Temperatur des Glases bzw. der Anode sind.

Die Emissionsvermögen der Aussen- und Innenteile der Anode unterscheiden sich[2]) (S. 176–178) und mit $q_a = N_{au}/N_{av}$ gilt nach ähnlicher Überlegung wie oben

$$\mathrm{d}\,(\sigma \cdot e_{ta} \cdot T_{au}^4) = \mathrm{d}\,(\sigma \cdot e_{tk} \cdot T_k^4)$$

oder (e_{tk} = Emissionskoeffizient der Kathode)

$$\frac{\mathrm{d}T_{kb}}{T_{k0}} = \frac{\mathrm{d}T_b}{T_{b0}} \cdot q_a \cdot \frac{e_{tb}}{e_{tk}} \left(\frac{T_{b0}}{T_{k0}}\right)^4 . \qquad (2)$$

[1]) V. Radeka, Periodicum math.-phys. et astr. Croatiae No. 3–4 (1956) 263.

[2]) B. M. Zarew, Berechnung und Konstruktion von Elektronenröhren, (Verlag Technik, Berlin, 1955).

Bei einer Erhöhung der Raumtemperatur um 1° C wird die Kathodentemperatur relativ um 5.3×10^{-7} vergrössert. Das führt[1]) zu einer Heizstromerhöhung

$$\frac{dI_{hb}}{I_{h0}} = \left(2 - \frac{\alpha}{2}\right) \frac{dT_{kb}}{T_{k0}} = 7.5 \times 10^{-7}/°C \qquad (3)$$

worauf wir noch in Kapitel 4 näher eingehen werden.

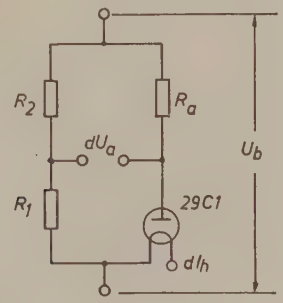

Bild 2. Diode 29C1 in Brückenschaltung.

(b) Viel grösseren Einfluss als die Aussentemperaturänderungen haben die Schwankungen der Anodenspeisespannung der Diode. Nach Bild 2 folgt

$$dU_a = dU_b\,(\xi - \gamma) = 2.6\,V/\% \ . \qquad (4)$$

Daraus ist gleich zu entnehmen, dass U_b gut stabilisiert sein muss, wenn ein hoher Grad der Stromstabilisation gewünscht ist.

(c) Ähnlich ist die Situation bei der Änderung des Anodenwiderstandes der Diode. Aus (1) folgt durch Differentiierung

$$\frac{dI_a}{I_{a0}} = -\frac{dR_a}{R_a} \cdot \xi = -7.2 \times 10^{-3}/\% \ . \qquad (5)$$

3. Der Verstärker

Obwohl die Diode eine ausserordentlich hohe Verstärkung besitzt, ist es für unsere Anforderungen notwendig, in den Stabilisator noch eine Verstärkerstufe einzubauen. Diese ist aus zwei Pentoden in Differenzschaltung (Bild 3) zusammengesetzt, wodurch noch immer genügende Verstärkung zu erreichen ist, aber die Heizspannungsänderungen der Pentoden nicht zum Ausdruck kommen. Mit $R_{ap} = 0.5$ MOhm konnte $K = \frac{1}{2} K_0 = 100$ erzielt worden, wobei K_0 die Verstärkung einer Pentode bedeutet.

Die nachstehende Pentodenschaltung dient zur voller Ausnutzung des zur Verfügung stehendes Strombereiches der Regulatorröhren 6AS7G (Bild 3) unter Berücksichtigung der maximal zulässiger Spannung an diesen Röhren und ist keineswegs ein notwendiges Element des Stabilisators. Die Gesamtverstärkung wird durch diese Pentode nur wenig beeinflusst.

4. Der Stromstabilisator

Auf Bild 3 ist die gesamte Schaltung des Stabilisators wiedergegeben. Mit (1) und den Bezeichnungen aus Bild 3 gilt dann

$$i = \frac{E_1 + \mu \cdot K \cdot a_1 \cdot I_{h0}}{(R_m + R_f)(1 + \mu) + R_u + \mu \cdot K \cdot a_1 \cdot \beta} \qquad (6)$$

$$\beta = \frac{R_p}{R_h + R_p}, \qquad R_f = \frac{R_h R_p}{R_h + R_p}$$

und angenähert

$$i = \frac{I_{h0}}{\beta} \qquad (6a)$$

$$\frac{di}{dE_1} = \frac{1}{\mu \cdot K \cdot a_1 \cdot \beta} \qquad (7)$$

$$\frac{di}{dR_m} = \frac{-I_{h0}}{K \cdot a_1 \cdot \beta^2} \ . \qquad (8)$$

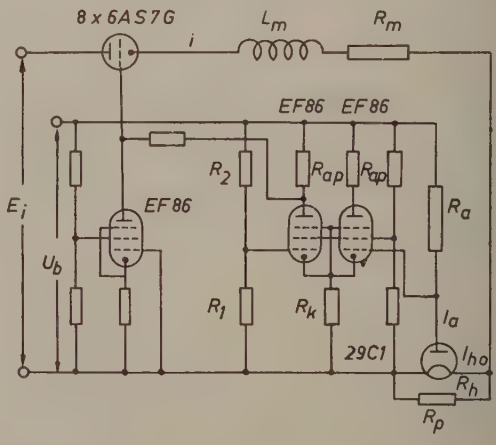

Bild 3. Gesamtschaltung des Stromstabilisators.

Bei einer Stromentnahme von $i = 0.8$ A, $\mu = 2$ und $\beta = 0.88$ ist die Stromänderung im Verbraucher 0.7×10^{-6} A/V bzw. 1.1×10^{-6} A/Ohm. Mit $E_1 = 400$ V, können wir noch $dE_1/E_1 = 14\%$ bei $di/i = 5 \times 10^{-5}$ tolerieren, was weit über die auf die Apparatur gestellten

Anforderungen liegt. Zur gleichen Zeit bleibt der Strom noch im Rahmen der Stabilisierungsgrenzen wenn sich die Last ($R_m = 200$ Ohm) um 18% geändert hat. Dies entspricht einer Temperaturerhöhung der Magnetspulen von rund 45° C.

Wir können noch untersuchen, wie sich verschiedene—im Kapitel 2 besprochene—Schwankungen in der Rückkopplungsschleife benehmen. Aus der Theorie der rückgekoppelter Verstärker benützen wir die Formel für die Ausgangsspannung E_2, wenn irgendwo in der Apparatur eine Störspannung E_s entsteht

$$E_2 = \frac{A_v \cdot E_s}{1 - r \cdot A_t} \tag{9}$$

wo A_v die Verstärkung von Störstelle bis zum Ausgang des Verstärkers und A_t die gesamte Verstärkung ist. Faktor r bezeichnet den Teil der Ausgangsspannung E_2, der zum Verstärkereingang geführt wird.

Aus (9) bekommen wir nach unserer Schreibweise

$$\mathrm{d}i = \frac{E_s}{\dfrac{R_u + (1+\mu)(R_m + R_t)}{\mu \cdot K} + a_1 \beta} \tag{10}$$

was weiter ergibt

$$\mathrm{d}i = -\frac{\mathrm{d}I_{hb}}{I_{h0}} \cdot \frac{1}{\dfrac{\beta}{\xi \cdot I_{h0}} + \dfrac{R_u + (1+\mu)(R_m + R_t)}{\mu \cdot K \cdot R_a \cdot I_{a0}} \cdot \dfrac{2 - \frac{1}{2}\alpha}{2 + \dfrac{b}{T_{k0}}}} \tag{11}$$

In unserem Fall folgt mit (3) $\mathrm{d}i/i = -\mathrm{d}I_{hb}/(I_{h0} \cdot \xi) = -1.0 \times 10^{-6}/°$ C und es ist ersichtlich, dass dies für normale Verhältnisse eine ausserordentlich hohe Stabilität gegen Umgebungstemperaturschwankungen bedeutet.

Dementsprechend erzeugen nach (4) und (10) die Schwankungen von U_b eine Stromänderung im Verbraucher

$$\frac{\mathrm{d}i}{i} = \frac{\mathrm{d}U_b}{U_b} \cdot \frac{\dfrac{U_b}{I_{h0}} \beta \cdot (\xi - \gamma)}{\dfrac{R_u + (1+\mu)(R_m + R_t)}{\mu \cdot K} + a_1 \cdot \beta} = 4.5 \times 10^{-4}/\% \ . \tag{12}$$

Für unsere Anforderungen darf die Spannung U_b nur um $1^0/_{00}$ variieren, was man bei der Konstruktion des Spannungsstabilisators beachten muss.

Ebenso unangenehm zeigen sich die Änderungen des Anodenwiderstandes R_a, wie aus (5) und (10) zu erkennen ist

$$\frac{\mathrm{d}i}{i} = -\frac{\mathrm{d}R_a}{R_a} \cdot \frac{\xi (1-\gamma) U_b}{a_1 \cdot I_{h0}} = -5 \times 10^{-4}/\% \tag{13}$$

und bei einer Stabilität 1:20 000 darf $\mathrm{d}R_a/R_a$ höchstens $1^0/_{00}$ ausmachen. Für unsere Apparatur ist als R_a ein aus Manganindraht gewickelter Widerstand genommen, der so dimensioniert wurde, dass ihn der Anodenstrom I_{a0} nicht bedeutend erwärmen konnte, d.h. dass auf R_a nur die Aussentemperaturänderungen Einfluss haben. Für oberen Fall dürfte dann die Umgebungstemperatur um 50° C variieren.

Zuletzt können wir noch auf die Frage der Stabilität des Widerstandes R_p näher eingehen. Aus (6) und (6a) bekommen wir

$$\frac{\mathrm{d}i}{i} = -\frac{\mathrm{d}\beta}{\beta}, \qquad \frac{\mathrm{d}\beta}{\beta} - (1-\beta)\frac{\mathrm{d}R_p}{R_p}. \tag{14}$$

Bei Drahtwiderständen aus Manganin beträgt $\mathrm{d}R_p/R_p = 2 \times 10^{-5}/°$ C und damit haben wir aus (14) im ungünstigsten Fall, d.h. bei grösstem Strom $i = 1.6$ A ($\beta = 0.45$), $\mathrm{d}\beta/\beta = 1.1 \times 10^{-5}/°$ C. Dadurch darf während einer Messung die Umgebungstemperatur um höchstens 5° C steigen bzw. fallen, wenn eine Stabilität 1:20 000 gewünscht ist. Die Erwärmung von R_p durch den Strom $(1-\beta) \cdot I_{h0}$ kann wegen der ausreichenden Dimensionierung des Widerstandes vernachlässigt werden.

5. Schaltvorgänge und Brummspannung

Die zeitlich veränderlichen Vorgänge stammen hauptsächlich von den sprunghaften Änderungen der Eingangsspannung, da die Erwärmung der Magnetspulen und die dadurch verursachte Störung $\mathrm{d}R_m$—im Verhältnis zu der Zeitkonstante des Gerätes—so langsam vor sich geht, dass man sie ohne weiters vernachlässigen kann.

Aus[1]) können wir vor allem entnehmen, dass der Heizfaden der Diode eine Zeitkonstante τ_d besitzt, welche von der Masse, Temperatur und

Leistungsverbrauch des Heizfadens abhängig ist; für die Diode 29C1 bei einer Heizleistung von 2.1 W beträgt die Zeitkonstante ungefär 80 ms. Die Zeitkonstante τ_k des Verstärkers ist im Vergleich zu τ_d sehr klein (Verminderung der Parasitkapazitäten durch sorgfältigen Aufbau der Elemente) und beträgt in unserem Fall 10–20 μs. Dadurch ist statt (7) die Differentialgleichung

$$(1+\mu)\,L_m\frac{\partial\,\mathrm{d}i(t)}{\partial t}+[(1+\mu)\,(R_m+R_t)+R_u]\,\mathrm{d}i(t)+\mu\cdot K\cdot\beta\cdot a_1\left[\mathrm{d}i(t)-\frac{c_p\cdot m}{2\,I_{ho}\,R_{ho}\beta}\frac{\partial\,\theta(t)}{\partial t}\right]=\mathrm{d}E_1 \tag{15}$$

gültig (L_m, Induktivität des Magnets, c_p, spez. Wärme, m, Fadenmasse, $\theta(t)$, Temperaturänderung des Heizfadens). Andererseits ist nach[1]) (O, Fadenoberfläche)

$$c_p\cdot m\frac{\partial\,\theta(t)}{\partial t}+\sigma\cdot e_{tk}\cdot O\cdot[T_{ko}+\theta(t)]^4=[I_{ho}+\beta\cdot\mathrm{d}i(t)]^2\,R_{ho}\left[1+\frac{\theta(t)}{T_{ko}}\right]^{\alpha} \tag{16}$$

daraus mit (15) ($\tau_L=(1+\mu)L_m/[(R_m+R_t)\,(1+\mu)+R_u]$)

$$\frac{\partial^2\,\mathrm{d}i(t)}{\partial t^2}+\left[\frac{1}{\tau_d}+\frac{1}{\tau_L}\right]\frac{\partial\,\mathrm{d}i(t)}{\partial t}+\left[\frac{1}{\tau_L\tau_d}+\frac{\mu\cdot K\cdot\beta\cdot a_1}{(1+\mu)\,L_m\cdot\tau_d}\right]\mathrm{d}i(t)=\frac{\frac{\partial\,\mathrm{d}E_1}{\partial t}+\frac{1}{\tau_d}\mathrm{d}E_1}{(1+\mu)\,L_m}. \tag{17}$$†

Mit vorher angegebenen Werten und mit L_m zwischen 500–1000 H sind gedämpfte Schwingungen kleiner Amplituden (Grössenordnung des stationären Wertes der Stromänderung di) vorhanden, doch ist in Wirklichkeit die Situation besser, da wegen den Filtern vor dem Stabilisator dE_1 nicht in sprunghafter Form entstehen kann.

Der Gleichstrom durch den Verbraucher soll möglichst brummfrei sein, weil die Wechselstromkomponenten zusätzliche Erwärmung des Fadens verursachen und stellen damit einen nicht kontrollierbaren Störungssignal vor, wessen Anderungen die Stabilität stark vermindern können.

6. Messergebnisse

Der Strom i wurde mittels einen Referenzwiderstandes (2 Ohm $\pm$ 0.01%) und Kompensationsapparat (Genauigkeit 1:100 000) gemessen. Die im Kapitel 4 theoretisch behandelten Änderungen konnten dadurch bestätigt werden und zwar in Fehlergrenzen von 20%. Dieser Fehler entsteht meistens durch den unrichtig bestimmten Faktor ξ in (1), bzw. bei der Temperaturmessung durch die ungleichmässige Erwärmung des Glaskolbens der Diode. Der Stabilisator besitzt eine Erwärmungszeit von 30–40 Minuten (hauptsächlich Änderungen der Hilfsspannung U_b) und der Strom bleibt nachher in den Grenzen von 1:20 000 für mehrere Tagen. Änderungen des Sollwertes zwischen 0.8 und 1.6 A haben nach der Erwämungszeit keinen bedeutenden Einfluss auf die Stabilität.

Die Reproduzibilität des Stromes nach 40 Minuten Erwärmungszeit ist besser als 1:10 000.

Der Verfasser spricht hiermit Kollegen Dipl. Ing. H. Babić für zahlreiche Diskussionen und nützliche Anweisungen und Herrn A. Miran für technische Ausführung des Gerätes verbindlichsten Dank aus.

† Wegen der Länge ist die Lösung der Differentialgleichung hier nicht angeführt.

NUCLEAR INSTRUMENTS 3 (1958) 265–270; NORTH-HOLLAND PUBLISHING CO. – AMSTERDAM

DETERMINATION OF THE MASSES AND MOMENTA OF CHARGED PARTICLES FROM MULTIPLE SCATTERING MEASUREMENTS IN A PROPANE BUBBLE CHAMBER†

V. G. KIRILLOV-UGRYUMOV, L. P. KOTENKO, E. P. KUZNETSOV and A. V. SAMOILOV

P. N. Lebedev Physical Institute, USSR Academy of Sciences, Moscow

Received 1 July 1958

It is shown that the masses and momenta of charged particles can be determined from measurements of multiple scattering in a propane bubble chamber. To measure a mass of the order of a π-meson or μ-meson mass with an accuracy of 30% it is sufficient to have a 36 cm range in propane; to determine a mass of the order of the proton mass with the same accuracy a range of 72 cm in propane suffices. To measure a particle momentum of the order of 100 MeV with an accuracy, say, of 15%, it is sufficient to have a range of 25 cm in propane.

1. Introduction

Bubble chambers will find wider application in physical experiments when it becomes possible to measure the momenta and masses of particles from their angles of multiple scattering in the liquid of the chamber. The method of determining the mass and momentum (or, to be more exact, the product of the momentum by the velocity) of particles by multiple scattering measurements has found wide application in experiments with photographic emulsions and, more recently, multiplate cloud chambers. In photographic emulsions the angles of multiple scattering are measured on elements of track ("cells") 50–100 μ in length. For short particle tracks (5–10 mm) this allows of determining the mass (utilizing the data on the residual range and ionization) with good accuracy.

In bubble chamber experiments, due to several circumstances, the track of a particle cannot be divided into such elements. This is due mainly to the large size of the bubbles which form the track and to their small density. The diameters of the bubbles in a bubble chamber are several times greater than the cell lengths usually chosen in nuclear emulsions. As a result, in view of the available quality of the tracks in a propane (C_3H_8) bubble chamber it becomes necessary to utilize cell lengths of the order of 10 mm.

For an analysis of multiple scattering in a bubble chamber we utilized the method of Olbert *et al.*[1]), which in addition to multiple scattering, takes into account single and double Coulomb scattering as well as the finite dimensions of the nucleus (the latter consideration may be disregarded in the case of the particles and energies considered in our experiments on scattering in propane).

2. Experimental Material, Method of Measurement, Experimental Errors

The multiple scattering measurements were made on photographs of tracks of π^+ and μ^--mesons and protons which came to rest in an propane bubble chamber[2]). The chamber was irradiated on the phasotron of the Joint Institute of Nuclear Research. In order to increase the range of the stopped particles, a 5 mm brass plate was set up in the middle of the chamber

† The present paper represents the extended text of the report delivered by the authors at the symposium on cloud chambers, diffusion and bubble chambers held at Dubna, November, 1957.

[1]) M. Annis, H. Bridge and S. Olbert, Phys. Rev. 89 (1953) 1216.

[2]) L. P. Kotenko, Yu. S Popov and E. P. Kuznetsov, Pribory i Tekhnika Eksperimenta No. 1 (1957).

(length of effective volume–16 cm). We chose for analysis 246 photographs of the tracks of particles which came to rest in the second half of the chamber. The multiple scattering angles were measured by the method of chords used with nuclear emulsions[3]). In this method the substitution of the angle between two chords for the angle between two tangents to the track of the particle leads to a systematic error. For a chord equal to one-half the cell length this error amounts to 2%, decreasing as the length of the chord decreases. The angles were measured with a general purpose measuring microscope which gives an accuracy of 1′ in angular measurements and 1 μ in linear measurements. The scale marks of the microscope were set on the centres of the last bubbles on the chord, or on the centres of gravity of groups of bubbles on the ends of the chord when the density of the bubbles was great. The residual ranges were measured from the middle of the corresponding cell of the track. Since the cells in a bubble chamber are of necessity large, energy losses along their length become appreciable. In order to avoid considerable error the residual range should be several times greater than the cell length. This condition was satisfied in our experiments, since we measured the angles for particles which came to rest in the second half of the chamber, i.e., beyond the brass plate, on the part of the track before the plate.

The root mean square error of one measurement of the angle for meson tracks (density $10 \div 20$ bubbles per cm) was 17′. For the proton tracks where the bubble density is several times greater, the root mean square error was 7.6′ (for a chord length of 3 mm). In computing the root mean square error we took several measurements of each angle, every time subtending the chord between neighbouring bubbles, so as to take into account the spread of the bubbles about the axis of the track. The cell lengths and the rational number of measurements of each angle were chosen taking into consideration that the root mean square scattering angle for a cell should be at least five times greater than the experimental error (in this case the error in the angle is not greater than 2%). For cell lengths of 1 cm and 2 cm C_3H_8 and a chord length of 3 mm five measurements of each angle on the meson and proton tracks yielded experimental errors of 7.5′ and 3.5′, respectively, so that the condition regarding the ratio of the measured angle to the experimental error is satisfied. The root mean square scattering angles of mesons on a path of 1 cm in propane at our energies comprised 54′, and for protons on a path of 2 cm in propane 30′.

We considered the problem of distortions of the projections of the angles in propane for the given geometry of the photography. It can be shown[4]), that for particle tracks running parallel or at small angles (5°–20°) to the plane of the photographic film the central projection of the angle obtained in the photograph practically does not differ from the orthogonal projection.

In analyzing the particle tracks we measured the projections of the angles on the plane of the photographic film, whereas the accepted theories of multiple scattering are based on the projections of the angles on a plane passing through the initial direction of the track. The mean deviation of the track in the region of measurement of multiple scattering from the plane of the photographic film did not exceed 5°, which affects the projection of the angle of multiple scattering by a factor of $\cos^{\frac{3}{2}} \alpha$, where α is the angle of inclination of the particle track to the plane of the film. $\cos^{\frac{3}{2}} 5° = 0.994$, i.e., the maximum change in the angle is insignificant, $\approx 1\%$.

Among the factors which may cause noticeable distortion of the bubble track and the angles one must consider possible local disturbances in the liquid of the chamber up to the moment of photographing; a parallel transfer of the track, even if it does exist, will not affect the magnitude of the angles. In order to test our assumption of the absence of local distortions of the track we carried out the following measurement. The section of the track up to

[3]) Y. Goldschmidt-Clermont, D. T. King, H. Muirhead and D. M. Riston, Proc. Phys. Soc. A **61** (1948) 138.

the plate for a particle which came to rest in the second half of the chamber was divided into three equal elements. On each element we measured the multiple scattering angles–φ_1, φ_2, φ_3, respectively. We also measured the scattering angle on all three elements taken together–φ_4. In the absence of local distortions we should have

$$\sqrt{\bar{\varphi}_1^2 + \bar{\varphi}_2^2 + \bar{\varphi}_3^2} = \bar{\varphi}_4$$

in the Gaussian approximation.

TABLE 1

Particle	Number of angles	$\sqrt{\bar{\varphi}_1^2+\bar{\varphi}_2^2+\bar{\varphi}_3^2}$	$\bar{\varphi}_4$
π^+	101	$104' \pm 7'$	$102' \pm 6'$
μ^-	51	$124' \pm 13'$	$114' \pm 11'$
p	96	$41' \pm 2'$	$42' \pm 2'$

The data of table 1 testify to the absence of such distortions, or at any rate, to the fact that the distortions are small relative to the statistical error. In addition, these data provide additional proof that in general, the experimenta errors in the measurement of the angles are small. Were the errors slightly greater than the angles measured, we should have the following relation:

$$\bar{\varphi}_1 = \bar{\varphi}_2 = \bar{\varphi}_3 = \bar{\varphi}_4, \text{ i.e., } \sqrt{\bar{\varphi}_1^2 + \bar{\varphi}_2^2 + \bar{\varphi}_3^2}/\sqrt{3} = \bar{\varphi}_4 .$$

3. Determination of the Particle Mass

To determine the mass of the particle we made use of the formula obtained by S. Olbert *et al.*[4]:

$$\frac{1}{n}\sum_{i=1}^{n}(\varphi_i R_i^{\alpha}) = K_1 (A_Z m_e c^2)^{\alpha} \sqrt{t}\left(\frac{m_e}{m}\right)^{1-\alpha} \qquad (1)$$

$$K_1 = \left[8 r_e^2 N \frac{Z^2}{A} G\right]^{\frac{1}{2}}\left[1 + \frac{0.982}{2G} + \omega\right]$$

where m is the mass of the scattered particle, t–the thickness of the scattering layer in g/cm², φ_i–the projection of the scattering angle, R_i–the residual range in g/cm², N–Avogadro's number, A–the atomic weight, $\alpha = 0.55$ for all the cells, Z–the nuclear charge, m_e and r_e–the mass and classical radius of the electron, ω–the correction for the finite dimensions of the nucleus. For the energies used this correction is negligible in propane in comparison with 0.982/2 G.

The quantity A_Z is determined from the relation:

$$\frac{R}{mc^2} = A_Z\left(\frac{\Pi}{mc^2}\right)^{1/\alpha} \qquad (2)$$

where $\Pi = p\beta c$. At $\alpha = 0.55$ formula (1) is valid over a wide range of particle velocities

$$0.05 \leqslant \frac{\Pi}{mc^2} \leqslant 2 \qquad (3)$$

which corresponds to range intervals in propane for μ-mesons, π-mesons and protons of $0.2 \div 120$ cm, $0.2 \div 143$ cm and $1.4 \div 1000$ cm, respectively.

For propane $A_Z = 0.2785$

$$G \cong 5.66 + 1.24 \log_{10}\left[Z^{4/3}A^{-1}t\left\{1.13\beta^2 + 3.76\left(\frac{Z}{137}\right)^2\right\}^{-1}\right].$$

The coefficient $K_1 (A_Z m_e c^2)^{\alpha}\sqrt{t}$ (see formula (1)) equals 1692 for a cell length of 1 cm C_3H_8† and 2398 for a cell length of 2 cm C_3H_8.

3.1. π^+-MESONS

We measured 312 angles on 104 tracks of π^+-mesons using 2 cm cells. Since only three angles were measured on one track the statistical accuracy of the mass determination from one track is extremely low. The mass determined from 104 tracks of π^+-mesons equals

$$m_{\pi} = (268 \pm 23)\, m_e .$$

The statistical error in the determination of the mass equals $\Delta m/m = 2.22/\sqrt{2n}$, at $n \gg 1$, where n is the number of angles.

Fig. 1 gives the distribution of the parameter ξ introduced by Olbert:

$$\xi = \left[\frac{1}{n-1}\sum_{i=1}^{n}(\varphi_i R_i^{\alpha})^2\right]^{\frac{1}{2}} .$$

[4]) L. P. Kotenko, E. P. Kuznetsov, A. V. Samoilov and F. M. Sergeyev. Report at the Symposium on Cloud Chambers, Diffusion and Bubble Chambers, Dubna, November 1957.

† The propane is at a temperature of 65° C, at which its density is 0.42 g/cm³.

TABLE 2

Number of tracks	Number of angles	Mass of π^+-meson in m_e
12	36	429 ± 112
12	36	338 ± 89
12	36	181 ± 47
12	36	213 ± 56
12	36	227 ± 59
12	36	229 ± 78
12	36	230 ± 60
12	36	366 ± 96
8	24	325 ± 104

As can be seen, the experimental distribution of the parameter ξ is in good agreement with the theoretical for the mass 276 m_e. Table 2 gives the values of the masses of π-mesons determined from groups of 12 tracks each.

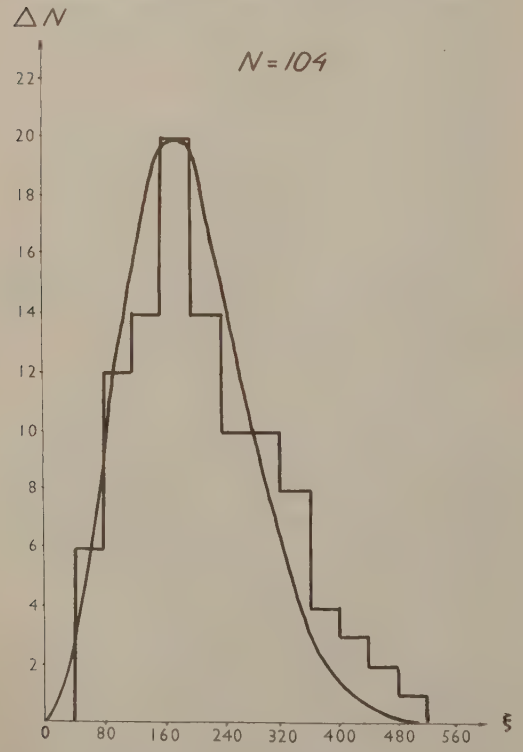

Fig. 1. Distribution of ξ for 104 stopped π^+-mesons. Solid line-theoretical value of ξ for a mass 276 m_e.

In order to reduce the range necessary for the determination of the particle mass with an accuracy of 10–15% the track was divided into 1 cm elements. The mass of the π-meson determined from 22 tracks, i.e., on 132 cm of useful track length, equals:

$$m_\pi = (263 \pm 37)\, m_e\ .$$

3.2. PROTONS

The mass of the proton was determined from 96 tracks (cell length–2 cm C_3H_8). We measured 288 angles on 96 tracks. The proton mass determined from these 288 angles equals:

$$m_p = (1973 \pm 184)\, m_e\ .$$

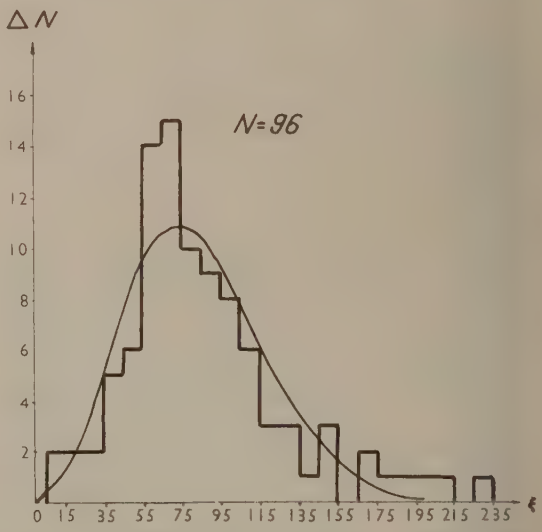

Fig. 2. Distribution of ξ for 96 stopped protons. Solid line-theoretical value of ξ for tracks of particles of mass 1836 m_e.

The distribution of the parameter ξ shown in fig. 2 is also in satisfactory agreement whith the theory. Table 3 gives the values of the proton mass obtained from measurements on groups of 12 tracks each.

TABLE 3

Number of tracks	Number of angles	Mass of proton in m_e
12	36	1116 ± 292
12	36	1950 ± 511
12	36	2650 ± 694
12	36	2075 ± 544
12	36	4015 ± 1052
12	36	2157 ± 565
12	36	3293 ± 863
12	36	1531 ± 401

3.3. μ^--MESONS

To determine the mass of the μ-meson we chose 22 photographs of the tracks of μ^--mesons that stopped in the second half of the chamber. Only two tracks with abnormally large angles (greater than five times the root mean square value) were rejected. The computations show that in view of the admixture of μ^--mesons present (1:1) these cases can be interpreted as the decay of π^--mesons in flight. If one assumes Molière's distribution[3]), the probability of scattering on such angles comprises $\approx 10^{-4}$.

We measured 132 angles on 22 tracks with cell lengths of 1 cm C_3H_8. The mass of the μ-meson determined from the 22 tracks, i.e., from 132 cm of useful range, proved equal to

$$m_\mu = (196 \pm 25)\, m_e .$$

It should be observed that formula (1), according to which the masses of the particles were computed, takes into consideration only Coulomb interaction. Estimates show that under the conditions of our experiments the effects of nuclear interaction of π-mesons and protons can be neglected in multiple scattering measurements.

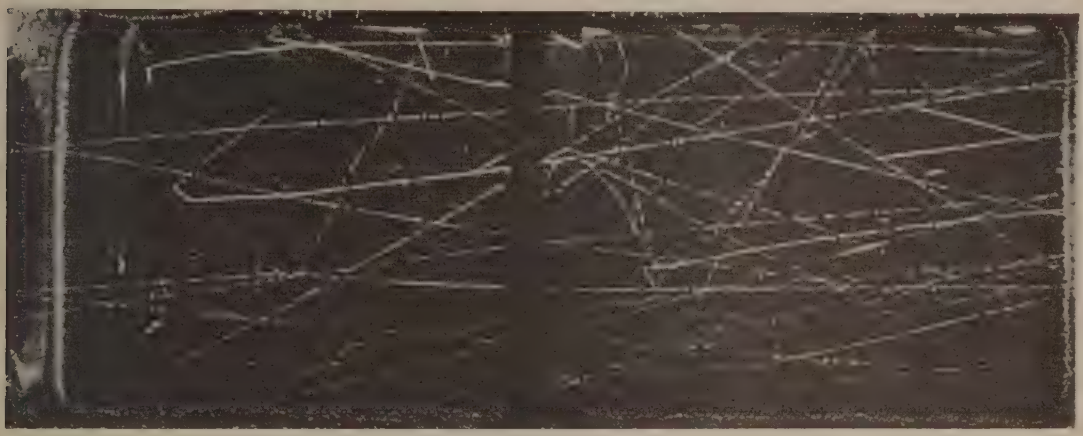

Fig. 3. Photographs of π^+-mesons stopped in the chamber.

4. Measurement of Particle Momentum

The momenta of the particles (or, to be more exact, $p\beta c$), according to Olbert, can be computed from the formula:

$$\Pi = K_1 \left[\frac{1}{n} \sum_{i=1}^{n} | \varphi_i | \right]^{-1} \sqrt{t} \cdot m_e c^2 . \qquad (4)$$

The root mean square error equals: $\Delta\Pi = \Pi/\sqrt{2n}$. $K_1 \cdot \sqrt{t} \cdot m_e c^2 = 4178$ for a cell length of 2 cm C_3H_8 and 2995 for a cell length of 1 cm C_3H_8.

Table 4 gives the values of $p\beta c$ of the particles, determined from (4), and for comparison the values of $p\beta c$, determined from the ranges.

The data of the table show that for a

Table 4

Particle	Number of tracks	Number of angles	Useful range (cm)	$\overline{\Pi}$ computed from angles (MeV)	$\overline{\Pi}$ computed from ranges (MeV)
π^+-meson	22	132	132	71 ± 5 ($\pm$ 7%)	75
μ^--meson	22	132	132	67 ± 4 ($\pm$ 7%)	65
proton	96	288	576	177 ± 7 ($\pm$ 4%)	165

sufficiently large range the value of $p\beta c$ can be estimated with great accuracy. In order to estimate the momentum with an accuracy, for example, up to 15% for mesons at $p\beta c$ equal to about MeV it is sufficient to have a 25 cm range in propane; for protons a 50 cm range is sufficient at $p\beta c$ about 200 MeV.

5. Conclusions

1. The results of the experiments show that it is possible to determine the masses, energies and momenta of charged particles from multiple scattering measurements in a propane bubble chamber. The masses of the particles determined in our experiment have the following values:

$m_\pi = (\ 268 \pm\ 23)\ m_e$, $t = 2$ cm; 312 angles

$m_\pi = (\ 263 \pm\ 37)\ m_e$, $t = 1$ cm; 132 angles

$m_\mu = (\ 196 \pm\ 25)\ m_e$, $t = 1$ cm; 132 angles

$m_p = (1973 \pm 184)\ m_e$, $t = 2$ cm; 288 angles .

2. In order to reduce the range necessary for determining the masses and momenta of the particles with a given accuracy the quality of the tracks must be improved; this means increasing the density of the bubbles on the track several fold and simultaneously reducing the diameter of the bubbles to be photographed, as well as choosing liquids with larger values of Z. Estimates show that if we increase the sensitivity of the chamber several fold and measure the multiple scattering by the "method of second differences", we can reduce the cell length in the propane chamber by a factor of two; in other words, for a given accuracy of determination of the masses and momenta, the ranges utilized can be reduced by one half.

We take this opportunity to express our gratitude to corresponding member of the USSR Academy of Sciences A. I. Alikhanyan for his interest in our work and to M. I. Dayon for discussion of the results.

NUCLEAR INSTRUMENTS 3 (1958) 271–274; NORTH-HOLLAND PUBLISHING CO. – AMSTERDAM

READ-OUT SYSTEM FOR THE HUTCHINSON-SCARROTT ANALYZER

J. HANSÉN

Research Institute of National Defence, Stockholm 80

Received 18 August 1958

A read-out system is described which by a substraction method gives recorded number of pulses in the different channels on a scaler. The arrangement is specially made for binary coded analyzers.

1. Introduction

A draw-back associated with the Hutchinson-Scarrott pulse-height analyzer[1]) is that the stored information is displayed on the cathode-ray screen in the binary system. The usual procedure of converting the information to the decimal system has been to make the transformation by hand or with a slide-rule.

To get the result directly in the decimal system Maeder[2]) and Gallagher *et al.*[3]) have modified the analyzer so that the memory works with decimal pulse coding, and thus the display on the cathode-ray tube shows the

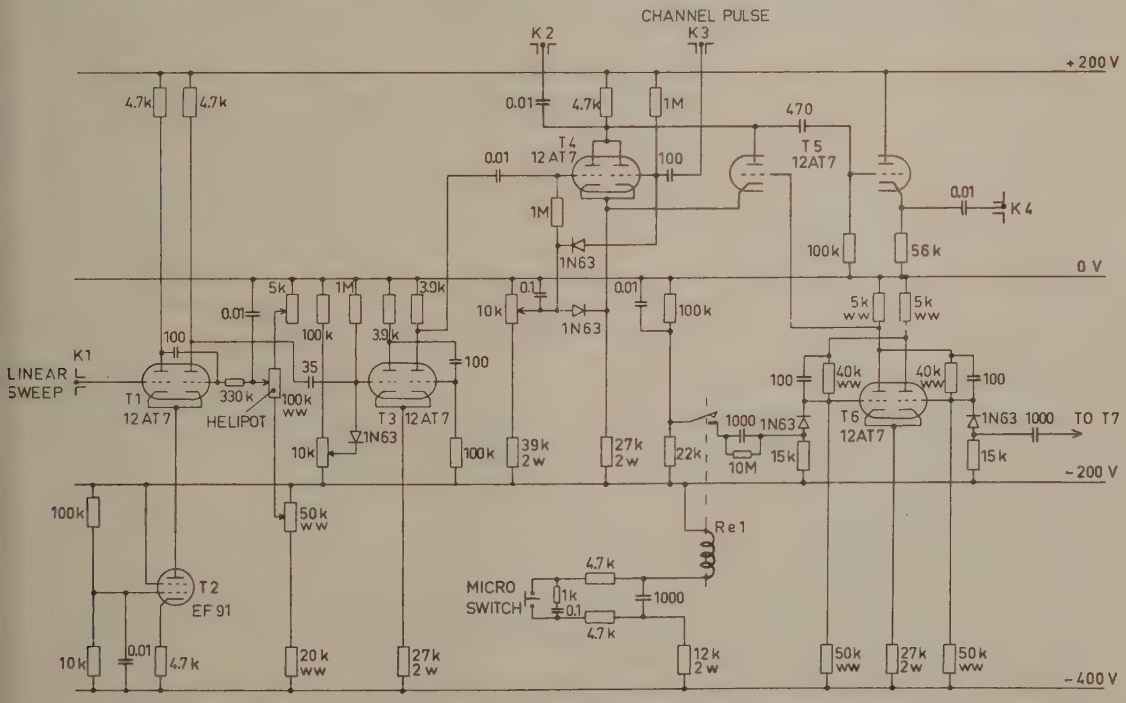

Fig. 1. Wiring diagram of the comparison circuit and the switch-off flip-flop.

[1]) G. W. Hutchinson and G. G. Scarrott, Phil Mag. **42** (1951) 792.

[2]) D. Maeder, Helv. Phys. Acta **29** (1956) 459; Nuclear Instruments **2** (1958) 121.

[3]) J. D. Gallagher, H. J. Lang and J. L. McKibben, LA-1917 (1955).

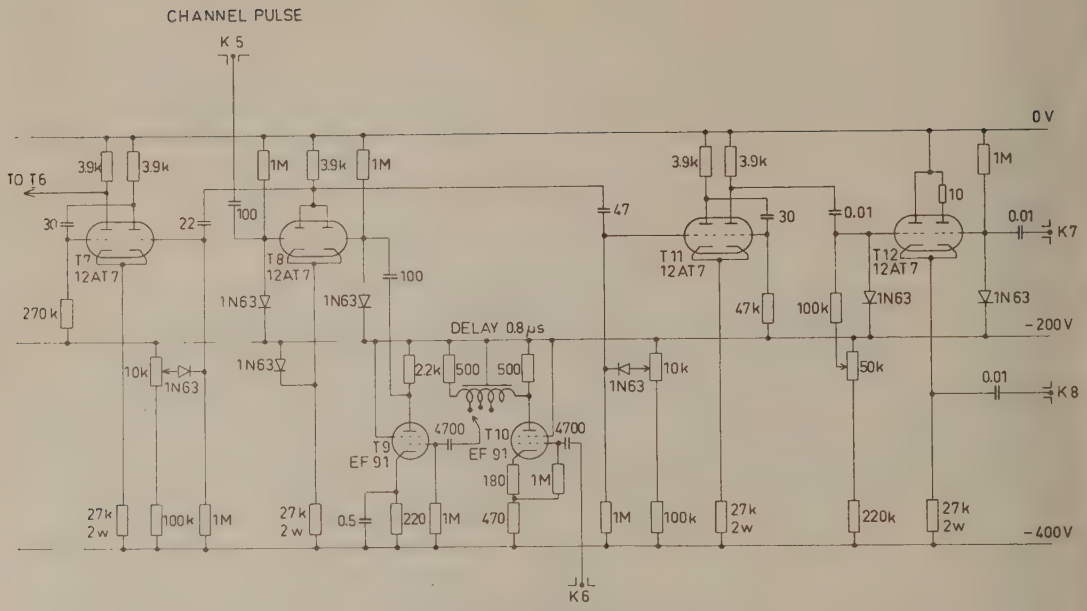

Fig. 2. Wiring diagram of the coincidence unit.

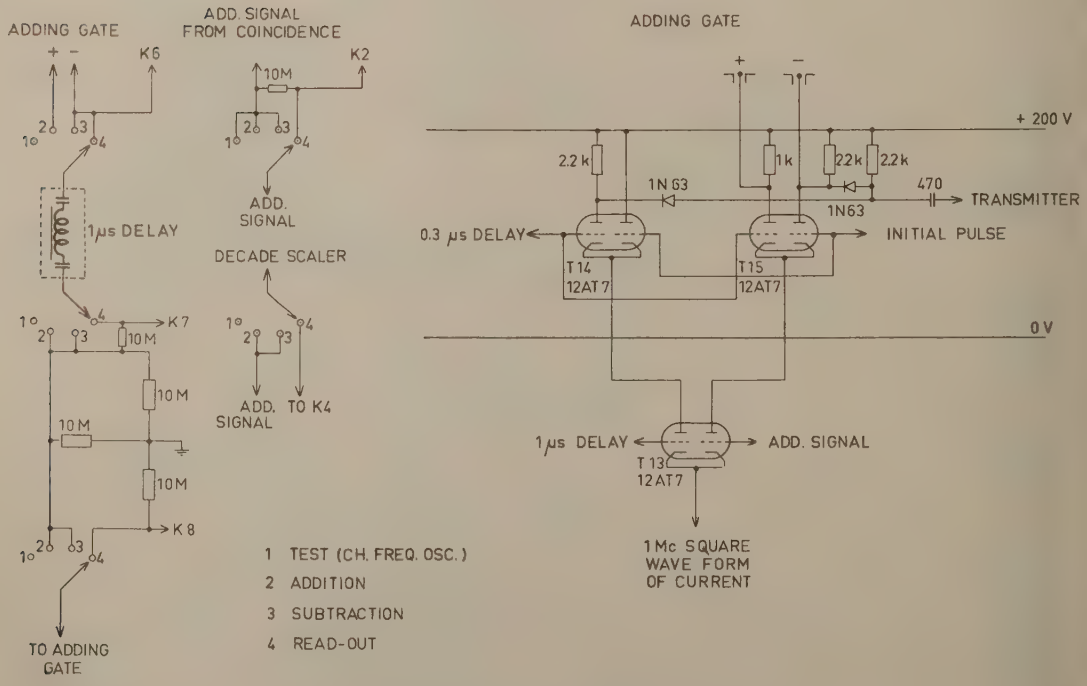

Fig. 3. Wiring diagram of the adding gate and switch unit.

numbers in a relatively easy to read decimal notation. This, however, reduces the memory capacity and makes a higher channel frequency necessary. Another method is the continous visual monitoring on an oscilloscope screen with the help of an analog converter or a print out on a recording potentiometer devised by Schultz *et al.*[4]).

the voltage of the linear sweep reaches the voltage level set with the Helipot the anode circuit of T1 in fig. 1 delivers a negative out-put pulse. This pulse is then shortened by the pulse-forming circuit (T3) to proper length (about 12 μs) and fed via T4 to the adding gate. T14 and T15 in fig. 3 (the adding gate) correspond to the two upper twin triodes in fig. 5 ref.[1]). The

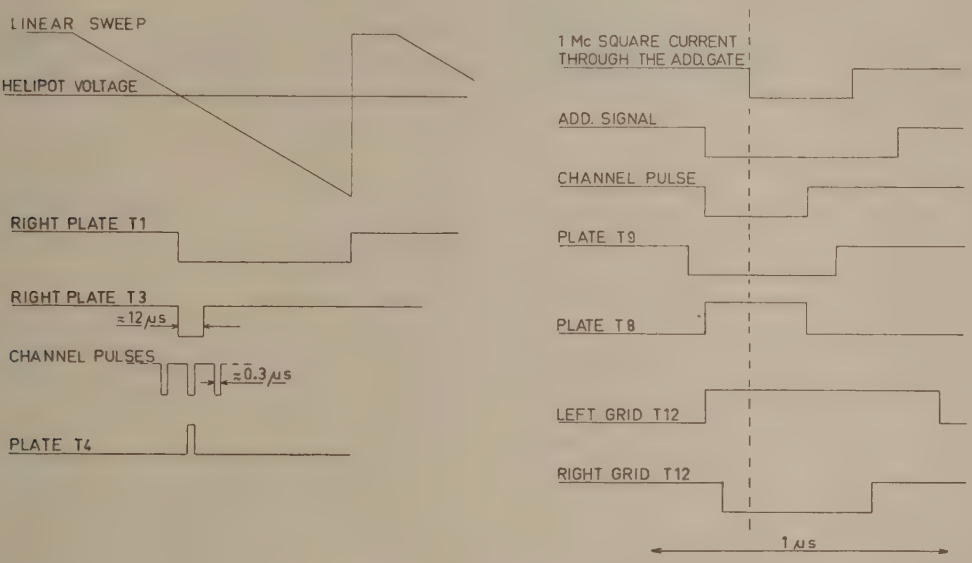

Fig. 4. Pulse forms in the switch off moment.

In order to get the exact number of pulses in one channel at a time from an ordinary *H-S* analyzer on a conventional decatron scaler a circuit has been designed which makes this conversion in a very short time.

The principle makes use of the possibility of making subtractions in the channels. The exact number of counts stored in a channel is obtained by counting the number of pulses required to empty it.

2. The Read-Out System

In order to be able to choose a certain channel the corresponding time position on the linear sweep has to be determined. This is done by using a D.C. voltage, set with a Helipot. When

changes of the original circuit has been made in order to make subtraction possible.

The channel maker pulse is fed to one input of a coincidence unit, T8 in fig. 2, and the out-put pulse from the adding gate is fed via a delay circuit (0.8 μs) to the other. When the channel in question is completely emplied the next channel maker pulse will fill it again. This gives a train of 12 out-put pulses from the adding gate spaced 1 μs in time. The last one of these, thus delayed 12 μs, will arrive at the same time as the subsequent channel maker pulse to the coincidence unit, the out-put pulses of which closes the gate T12 and gives a switch-off pulse to the flip-flop T6. It is only the 12th pulse in the pulse train that can give rise to a coincidence. The subtraction process is thus undisturbed until the channel is emptied and the next

[4]) H. L. Schultz, G. F. Pieper and L. Rosler, R.S.I. 27 (1956) 437.

channel maker pulse fills it again because the pulse train contain 12 pulses only in this last case.

It was assumed above that each channel was divided into 12 parts. This number can be changed without any changes in the read-out circuit.

In order to be able to operate the read out unit with one hand a mechanical arrangement is made on the helipot axis. By this arrangement the channel positions can be set in steps. At each step a micro switch is actuated which turns on the read-out unit and the counter unit. The counter is reset in the intermediate position between two channel positions.

The time required to read out one channel depends on the number of pulses recorded in it and amounts to, at a maximum, 5 sec (for 2^{12}—1 pulses) with a memory period of 1 250 μs. In ordinary recordings only a few channels are filled, therefore the mean time required to read out one channel will be about 1 sec.

NUCLEAR INSTRUMENTS 3 (1958) 275–277; NORTH-HOLLAND PUBLISHING CO. – AMSTERDAM

DEVICE FOR THERMAL CONTROL OF LIQUID HYDROGEN BUBBLE CHAMBERS

PIERRE AMIOT

Division of Scientific and Technical Services of CERN, *Geneva*

Received 13 May 1958

One of the important problems to be solved in the construction of hydrogen bubble chambers is the temperature control. A new device to overcome this difficulty is described. It is based on a closed circuit of pressurized hydrogen. A prototype has worked successfully. Its application to a liquid hydrogen bubble chamber has proved to be satisfactory.

1. Introduction

Various systems have been proposed to control the temperature of liquid hydrogen bubble chambers. Among them are the so called heat leak system and the pressurized bath system. The main disadvantage of the heat leak system is its lack of flexibility, which makes it necessary to produce an oversize design that calls for the use of auxiliary heaters with a consequent increase in the consumption of liquid hydrogen, especially during waiting periods.

With the pressurized bath system it is possible by pressure control to maintain around the outside of the chamber an even temperature which can be easily regulated. When the body of the chamber is made of a metal with a low thermal conductivity (i.e. stainless steel), the design can be so arranged as to have a large heat exchange area situated in the place where it is most needed (i.e. around the expansion mechanism) while keeping the walls thin and the whole apparatus very rigid. Obviously the main disadvantage of such a system lies in the difficulty of periodically refilling the pressurized reservoir from outside by means of a specially built pressure resistant dewar, without disturbing the temperature equilibrium. By pressurizing the dewar there are also serious risks of building up large temperature gradients in the liquid hydrogen.

The apparatus described below obviates these difficulties, since it provides for a closed circuit of pressurized hydrogen.

2. Basic Layout

The apparatus operates in accordance with the principles of the two phase thermosiphon and of the "cold wall". On the diagram shown in fig. 1 reservoir R_1 is the pressurized bath and it is in contact with the chamber body. P is the pressure and T the temperature inside the reservoir. The vapour phase communicates

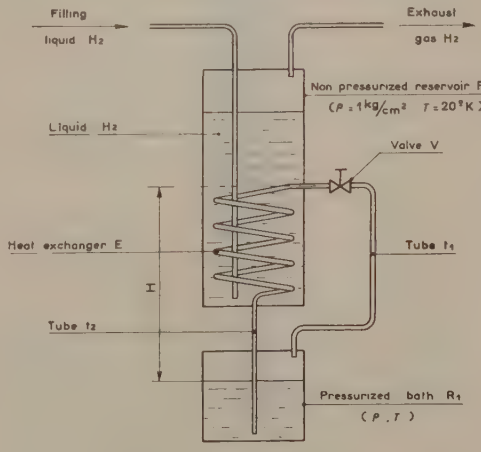

Fig. 1. Schematic diagram of the apparatus to control the temperature in a bubble chamber.

through pipe t_1 and valve V with the heat exchanger E, placed in reservoir R_2 filled with liquid hydrogen boiling under atmospheric pressure at a temperature of about 20° K. At the bottom of E, liquid hydrogen is allowed to return to the liquid phase of R_1 through tube t_2.

Valve V_1 being closed, if we assume thermal

conductivity to be negligible along t_1, t_2 and in liquid hydrogen as well as hydrogen gas, we can see that R_1, which has to bear the thermal load of the chamber, tends to get overheated so that pressure inside R_1 increases. Tube t_2 and the heat exchanger E are full of liquid while t_1 is full of gas. Let us assume that ρ_l and ρ_g represent respectively the specific gravities of liquid hydrogen and hydrogen gas under pressure P and temperature T, that H is the distance between the level of liquid in R_1 and the level of valve V and that P is the pressure at liquid

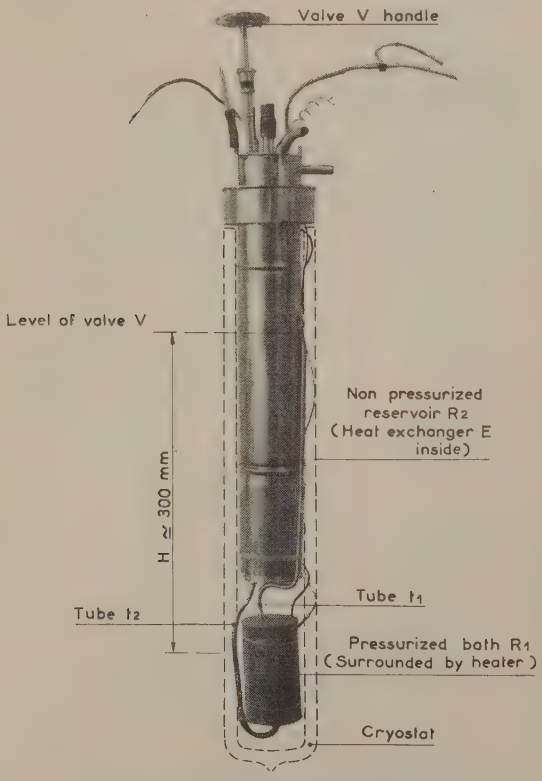

Fig. 2. Experimental set up built and tested at Kamerlingh Onnes Laboratorium, Leyden.

level in R_1. The pressures on the two sides of valve V are respectively $P - \rho_l H$ and $P - \rho_g H$. Consequently there is a difference in pressure between the two sides of V, equal to $H(\rho_g - \rho_l)$, the pressure on the gas side being greater than on the liquid side.

Under such conditions, if valve V is opened, the level of liquid in E will drop to a level H' and gas coming from t_1 at a temperature T and at the corresponding saturation pressure P, will liquefy on the walls of the heat exchanger which are in a bath at 20° K.

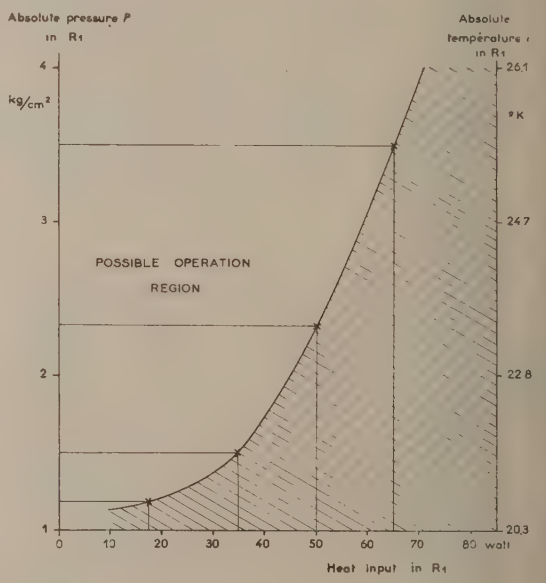

Fig. 3. Variation of minimum pressure P and temperature T with the heat input in R_1, valve V being completely open. Run made at the Kamerlingh Onnes Laboratorium in Leyden on November–December 1956.

Thus a closed circuit is obtained, which permits the automatic return in liquid form to the pressurized bath of the gas produced by boiling in the bath used to control the temperature of the chamber.

The parameters of the apparatus are obviously as follows:

the thermal load on R_1,

the temperature required T,

the distance H,

the drop in pressure in t_1, V, E and t_2,

the efficiency of E which determines the level H'.

It is difficult to design the heat exchanger E because, for reasons connected with the design of bubble chambers, there are certain restrictions concerning its shape.

A prototype, built by the Kamerlingh Onnes

Laboratorium in Leyden, and shown on fig. 2, had the following characteristics:

t_1 and t_2 = copper tubes with an inner diameter of 4 mm.
E = 4 m of spirally wound copper tubing with an inner diameter of 4 mm.
H = of the order of 300 mm.

The performance of this prototype is shown on fig. 3, for valve V in the fully open position.

3. Application

The layout described above has been put into operation in an experimental liquid hydrogen bubble chamber of 600 cc capacity, shown on fig. 4. In this case the distance H is around 150 mm, E consists of a pancacke of 4 turns made of 6 m of copper tubing with an inner diameter of 6 mm. Valve V is pneumatically

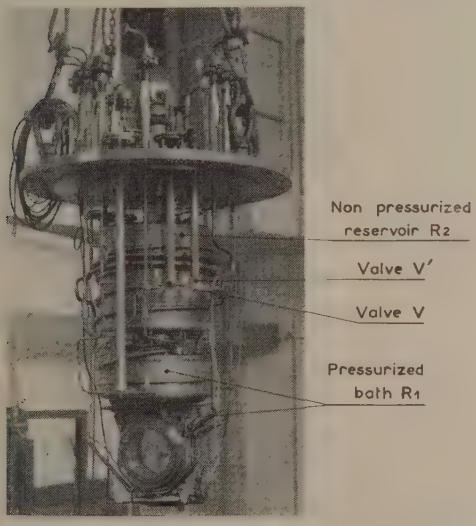

Fig. 4. Experimental liquid hydrogen bubble chamber built at CERN.

operated and remotely controlled by pressure P in R_1, and it has been placed in parallel with hand operated valve V' capable of fine adjustement. Trials with liquid nitrogen, V' being closed and V being actuated by an on-off system, have given the following results:

heat load on the bath	12 watt
temperature T	93° K
ΔT	16°
pressure $P \pm \Delta P$	4.5 ± 0.075 kg/cm²
V closed per cycle	80 sec
V open per cycle	10 sec.

It follows that, under these conditions, the maximum capacity of the heat exchanger is 110 watt. It must be noted that, as shown on fig. 4, valves V and V' are outside reservoir R_2, whereas in the prototype V was inside (fig. 3).

We think that the vibrations and the strong oscillations of pressure encountered with the prototype—which disappeared only by making constrictions on tube t_2—were due to this arrangement which allowed hydrogen to condense in t_1 before valve V. The liquid thus formed was probably sometimes falling down in t_1 and at other times violently thrown upward thus causing serious hammering in the system. Those phenomenons have completely disappeared in the design shown on fig. 4, at least with liquid nitrogen.

The system described above is now being applied to a liquid hydrogen bubble chamber of roughly 15 liter, under construction at CERN.

Acknowledgments

The author wishes to express his thanks to Dr. L. Kowarski for placing at his disposal the facilities without which this study could not have been undertaken, and to Professor Ch. Peyrou, for the interest he has shown in the development of this apparatus, which he eventually adopted for the bubble chamber constructed at CERN under his supervision.

The author also wants to record his gratitude to Professor K. W. Taconis of Kamerlingh Onnes Laboratorium at Leyden for making all the necessary arrangements to construct the prototype in his laboratory. His advice proved invaluable to the author.

NUCLEAR INSTRUMENTS 3 (1958) 278–284; NORTH-HOLLAND PUBLISHING CO. – AMSTERDAM

HODOSCOPE SYSTEM FOR EXPERIMENTS ON THE SCATTERING OF COSMIC RAY μ-MESONS

PART I — ELECTRONIC CIRCUITS

M. A. MEYER, P. H. STOKER and J. A. M. DE VILLIERS

Physics Department, University of Potchefstroom, South Africa

Received 25 August 1958

A description is given of the electronic circuits of a large hodoscope system which is being used in experiments on the scattering of μ-mesons. The principle of the method employed is to determine the direction of the trajectory of the particle before and after scattering by means of three systems of crossed counters. The counters through which the particle has passed are identified by means of neon lamps.

1. Introduction

A hodoscope is an arrangement of Geiger counters and associated electronic circuits which indicates by means of a series of neon lamps, one for each counter, which counters were discharged by the passage of a charged particle. The first hodoscope was designed by Johnson and Stevenson[1]) and apparently used mainly for demonstration purposes. Among the first to apply hodoscopes to the study of cosmic rays were Janossy and Ingleby[2]) Regener[3]) and Yeater[4]). Although the details of the circuits adopted by these early workers differed in detail, the principle upon which these and modern hodoscopes is based, is essentially the same. In order to observe cosmic ray tracks alone, without disturbance of the local radiation, the coincidence principle has been employed as a control circuit which suppresses the flashes of the neons for all individual counter discharges except those occurring coincidently with a master pulse which is formed whenever a certain counter or group of counters is discharged.

It will be realised that the hodoscope presents a method of determining the direction of the trajectory of a particle which passes through the hodoscope. This property was used by Hyams *et al.*[5]) in determining the energy of cosmic ray particles by measuring the deflection of the trajectory of a particle which has passed through a magnetic field. This feature of the hodoscope was also used by George *et al.*[6]) and by Amaldi *et al.*[7]) to study the interaction of cosmic rays with matter. Similarly, Alberigi-Quaranta *et al.*[8]) have used a hodoscope to measure the deflection of μ-mesons in magnetized iron blocks.

Hodoscopes also present an excellent means of indicating which and how many counters were discharged in a particular layer of counters. This property was used by Broadbent *et al.*[9]), Kasnitz *et al.*[10]) and Sitte *et al.*[11]) in the study of cosmic ray showers.

Other applications of the hodoscope include experiments such as the determination of the

[1]) T. H. Johnson and E. C. Stevenson, Joun. Frank. Inst. **216** (1933) 329.

[2]) L. Janossy and O. Ingleby, Journ. Sci. Instr. **19** (1942) 30.

[3]) V. H. Regener, Phys. Rev. **64** (1943) 250.

[4]) M. L. Yeater, Phys. Rev. **67** (1945) 74.

[5]) B. D. Hyams, M. G. Mylroi, B. G. Owen and J. G. Wilson, Proc. Phys. Soc. A **63** (1950) 1053.

[6]) E. P. George and P. T. Trent, Proc. Phys. Soc. A **64** (1951) 1134.

[7]) E. Amaldi, C. Castagnoli, A. Sigli and S. Scuitti, Nuovo Cimento **9** (1952) 453.

[8]) A. Alberigi-Quaranta and F. Pieracinni, Nuovo Cimento **6** (1957) 1084.

[9]) D. Broadbent, E. W. Kellermann and M. A. Hakeem, Proc. Phys. Soc. A **63** (1950) 864.

[10]) H. Kasnitz and K. Sitte, Phys. Rev. **94** (1954) 977.

[11]) K. Sitte, D. R. Stierwalt and I. L. Kofsky, Phys. Rev. **94** (1954) 988.

ratio of the positive to the negative particles in cosmic rays by Owen *et al.*[12]) and that of Barton[13]) who has designed a portable hodoscope which can be used in great depths in water. The usefulness of the hodoscope method for the investigation of the elementary processes of the generation of slow π-mesons by the nuclear active component of the cosmic radiation, was demonstrated by Zhdanov[14]).

and after scattering. The direction of the trajectory before and after scattering is determined by employing three systems A, B and C of crossed counters as shown in fig. 1. The scatterer is placed immediately above system B. The counters through which the particle has passed are identified by means of a series of neon lamps, one for each counter. A lower and upper limit on the energy of the particle is

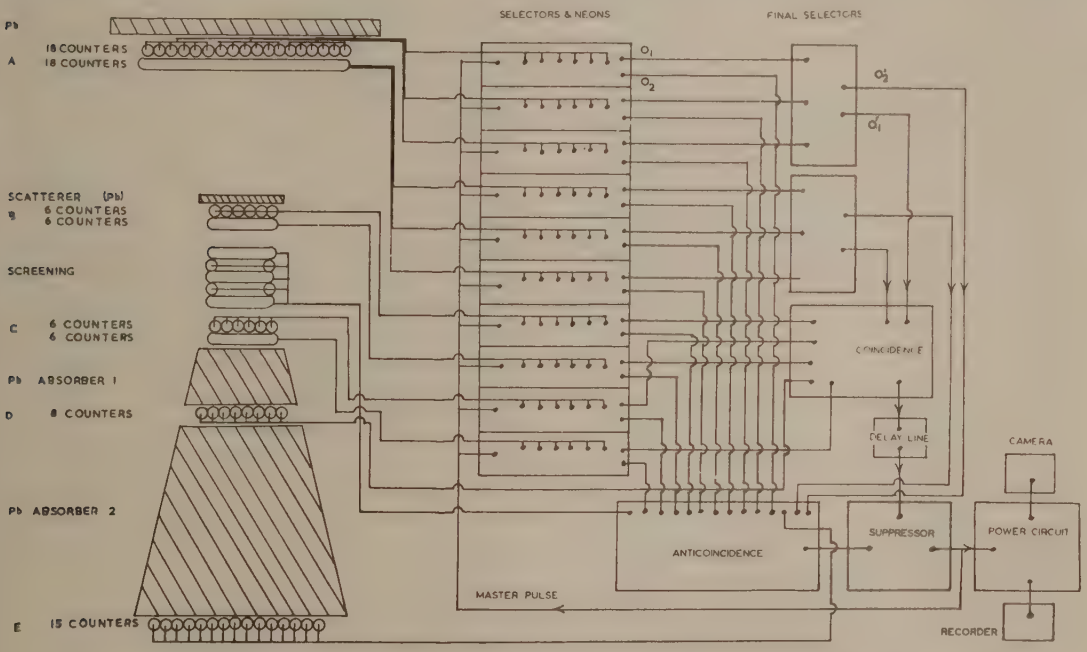

Fig. 1. Principle of the experiment and block diagram of the electronic circuits.

The most detailed description of modern hodoscopes is that of Owen[15]), and Zhadanov[14]). The principle of the circuit described here is based on that of Owen[15]).

2. Principle of the Hodoscope

2.1. PRINCIPLE OF THE METHOD

The instrument to be described is being used to study the scattering of μ-mesons by determining the direction of the trajectory before

placed by registering only those particles which passed through the counter system D but not through the counter system E. In order to arrive at a unique angle of scattering, events in which two or more particles pass simultaneously through the system of counters, must be avoided. The associated electronic circuits were therefore designed to record only events in which one particle passes unaccompanied through the counter systems A, B and C and which is absorbed in absorber 2. A reliable vacuum tube electronic circuit of good resolving time and fairly simple design fires the neons corresponding to the discharged counters whenever such an event occurs.

[12]) B. G. Owen and J. G. Wilson, Proc. Phys. Soc. A **62** (1949) 601.
[13]) J. C. Barton, Journ. Sci. Instr. **23** (1956) 308.
[14]) G. B. Zhdanov, Zh. Eksper. Teor. Fiz. **30** (1956) 437.
[15]) B. G. Owen, Proc. Phys. Soc. A **63** (1950) 1074.

The area of the systems A, B and C is 64.8^2 cm^2, 21.6^2 cm^2 and 21.6^2 cm^2 respectively. The incoming particles are therefore received over a large solid angle while the scattered particles are received over a comparatively small solid angle. This arrangement reduces the amount of lead required for absorber 2. A relatively high intensity was obtained with the abovementioned areas and scattering angles up to approximately 20° degrees can be measured, with a negligible background.

2.2. CIRCUIT SEQUENCE

The counter system A contains two layers of eighteen counters whereas systems B and C each contain two layers of six counters. On account of practical considerations, the eighteen counters in each of the layers in system A were divided into three groups, each containing six adjacent counters. The pulses from the six groups in the system A and the four groups in systems B and C are fed to ten identical circuits (fig. 1), called selectors. These circuits separate events in which a single counter in the group is discharged from events in which more than one counter in the group is discharged. These selectors delivered at an output terminal O_1 a pulse when at least one counter of the group is discharged and at another output terminal O_2 a pulse when at least two counters of the group are discharged. The pulses from the terminals O_1 of the selector circuits to which the counters of the system A are connected, are fed to two final-selectors, one for each layer. The final-selectors deliver a pulse at an output terminal O'_1 whenever at least one group in a layer is discharged and a pulse at another output terminal O'_2 whenever more than one of the three groups is discharged. The output terminals O'_1 at the two final selector circuits, the output terminals O_1 of the selector circuits to which the counter systems B and C are connected, as well as the pulses from the counter system D are fed to the coincidence circuit (fig. 1). The pulses from the output terminals O_2 of the ten selector circuits, the pulses from the output terminals O'_2 at the final-selectors as well as the pulses from the counter system E and the screening counters are fed to the anti-coincidence mixing circuit which delivers the anti-coincidence pulse to the suppressor circuit. The screening counters are arranged around the beam defined by the counter systems B and C.

A coincidence pulse is formed when at least one counter in each of the layers of the systems A, B, C and D are simultaneously discharged. The coincidence pulse from the coincidence circuit is delayed by one micro-second and subsequently fed to the suppressor circuit. When more than one counter is discharged in a layer of any of the systems A, B and C a pulse appears either at the output terminal O_2 of the selector circuits or O'_2 of the final selectors resulting in an anti-coincidence pulse which suppresses the coincidence pulse at the suppressor. In the absence of an anti-coincidence pulse, the coincidence pulse passes through the suppressor, and becomes the master pulse which actuates the power circuit for the camera and the mechanical recorder and the circuits which fire the neons, thus indicating which counters were discharged in the recorded event.

The performance of the hodoscope is described in the following publication.

3. The Electronic Circuits

3.1. GEIGER COUNTER CIRCUITS

Each Geiger counter is connected to a cathode follower shown in fig. 2. The pulses from the cathode followers to which the counters in the systems A, B and C are connected are fed through coaxial leads to the selector circuits shown in

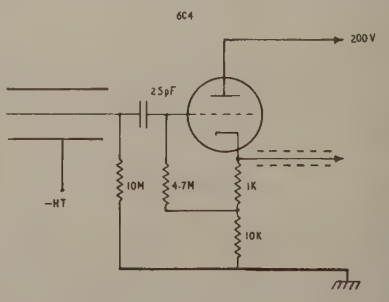

Fig. 2. Cathode follower circuit.

fig. 1. The pulses from the cathode followers to which the counters in the system D are connected, are mixed through crystal diodes (fig. 3),

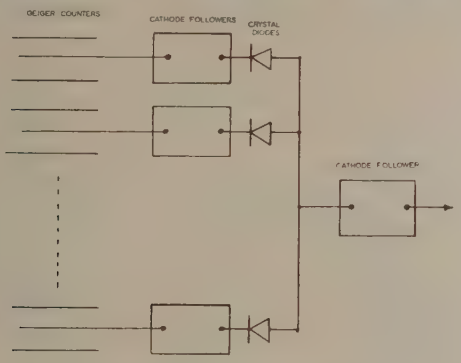

Fig. 3. Mixing circuit for the Geiger counters.

fed to a ninth cathode follower and subsequently to the coincidence circuit. The cathode followers to which the counters in the system E are connected are divided into two roughly equal groups. The pulses in each of these groups are mixed through crystal diodes in a manner similar to that shown in fig. 3 and subsequently fed through two leads, one for each group, to the anti-coincidence mixing circuit.

3.2. SELECTOR CIRCUITS

The circuit diagram of the selector circuits are shown in fig. 4. The pulses from the cathode followers are fed through diodes to a univibrator V_1 having a duration of about 8 micro-seconds. The negative univibrator pulses are fed to a conventional Rossi-circuit (left half of V_2) having a diode in the plate circuit. The resistor in series with the diode was given a value for good discrimination between pulses for single and two or more simultaneous counter discharges. Thus multiple discharges result in a large positive pulse. The discriminator V_6 is adjusted by means of the potentiometer in its grid circuit to amplify the multiple pulses only. The negative pulse from the anode of V_6 is transmitted through the cathode follower V_8 to the anti-coincidence mixing circuit.

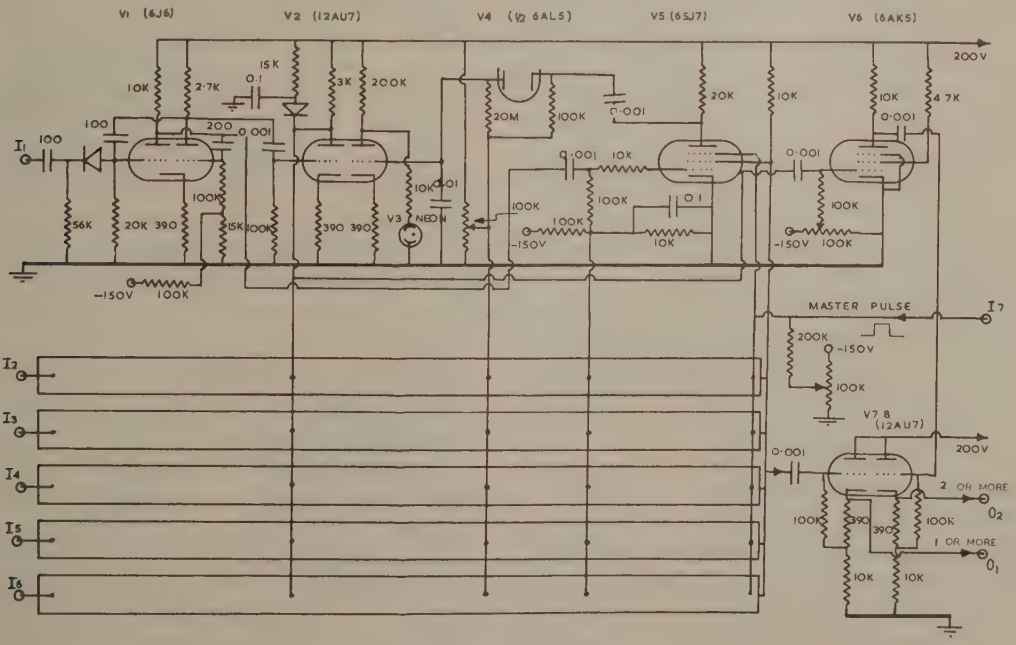

Fig. 4. Selector circuits.

The positive pulses from the univibrator V_1 are fed to the control grid of a 6SJ7(V_5) which, due to the negative grid bias, is non-conducting.

The positive pulse renders the tube conducting and consequently a negative pulse appears at te screen grid. At this stage no pulse appears at the anode because of the high negative potential of the suppressor grid. The screen grids of the 6SJ7's are connected together and fed through a common resistor. The negative pulses from the screen grid circuit are transmitted by a cathode follower V_7 to the output terminal O_1 and from there to the final selector circuits in the case of the counter system A or to the coincidence circuit in the case of the systems B and C as is shown in fig. 1.

When a desired event has occurred, the coincidence circuit provides a master pulse which is applied to the suppressor grids of the 6SJ7's (V_5). Plate current will flow through those V_5's where the control grid was made positive by a positive univibrator pulse. The duration of the univibrator pulse is sufficiently long to ensure that this pulse overlaps the master pulse. The negative pulses which appear at the anodes of those tubes which have received pulses at both the control and the suppressor grids, are fed through a diode V_4 to a *RC*-circuit having a time constant of 0.2 seconds. The integrated negative pulse is applied to the grid of a triode (right half of V_2) having a high resistor in its anode circuit. The negative pulse at the grid causes the anode voltage to rise sufficiently high to cause the neon V_3 to strike. The neon remains in discharge for about 0.25 seconds. The neons are mounted on a display board and are photographed by means of a cine-camera, operated on single frame exposure by an electromagnet which is activated by a power circuit.

3.3. FINAL SELECTOR CIRCUITS

The final selector circuits, shown in fig. 5, consist of a conventional Rossi circuit of three tubes V_1, V_2 and V_3 having a diode in the plate circuit which permitted good discrimination between single pulses and more than one simultaneous pulse at the grids of the Rossi tubes. The rest of the circuit is essentially the same as the selector circuits. The cathode follower feeds the pulse to the anti-coincidence mixing circuit. The incoming pulses are mixed by means of a circuit, shown in fig. 5, from where it is fed to the output terminal O'_1 which delivers a pulse when at least one pulse is applied to the input terminals.

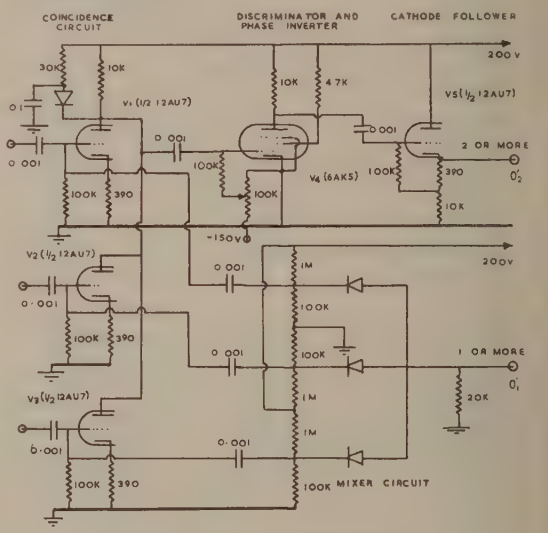

Fig. 5. Final selector circuits.

3.4. THE COINCIDENCE, ANTI-COINCIDENCE AND POWER CIRCUITS

The output terminals O'_1 of the two final selectors and the output terminals O_1 of the four selector circuits are connected to the coincidence circuit consisting of seven 6C4 triodes. The pulses from the counter system D are first shaped by a univibrator V_1 (fig. 6) and subsequently fed to the seventh tube of the coincidence circuit. The positive coincidence pulse is delayed and subsequently inverted by the left half of V_2, from where it is fed to the suppressor tube V_4. The anti-coincidence pulses which are shaped by a univibrator V_3 are obtained from a mixing circuit which is similar to the one shown in fig. 5. This anti-coincidence pulse is then fed to the suppressor tube. The output from the suppressor tube is the master pulse of approximately 90 volts. The master pulse is fed through cathode followers to the ten selector circuits and to the power unit (fig. 7) which operates the mechanical recorder and camera.

3.5. THE NEON LAMPS

The neon lamps, type NE 22, are mounted on a panel such that they occupy positions corresponding to the position of the counters in the hodoscope. They were mounted in $\frac{1}{2}$ inch thick perspex and illuminated by eight small 6V lamps also mounted in the perspex but shielded from the camera. The perspex acted as a light guide. The intensity of these lamps can be varied by means of a rheostat such that the position of all the neons are easily recognised and the neons which flashed could readily be identified.

It was noted by previous workers Janossy *et al.*[2]), Yeater[4]) and Arce[16]) that neons do not strike readily after being kept in the dark. If the lamps do not flash every time the voltage is applied, the data obtained from the hodoscope can be very misleading. Arce and co-workers incorporated a 4 watt ozone lamp shielded with an ultraviolet transmitting filter. They found that the neon lamps never failed to strike. The illumination of the neon lamps in this experiment is sufficient to ensure striking of the neons every time a voltage is applied although a slight delay of the order of 10^{-5} seconds was noted between the application of a voltage and the flashing of the lamp.

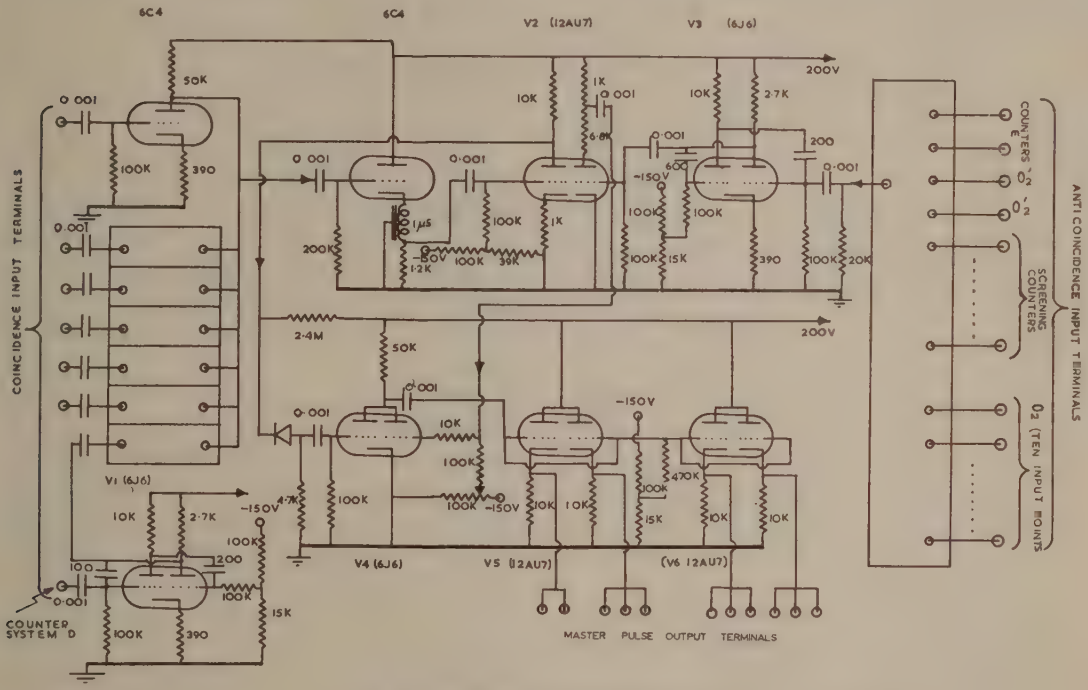

Fig. 6. Coincidence-anticoincidence circuit.

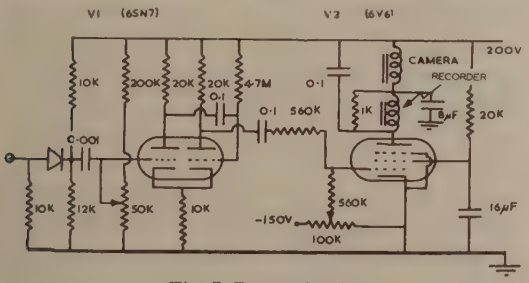

Fig. 7. Power circuit.

3.6. POWER SUPPLY

The 200 V anode supply voltage for the entire apparatus is obtained from three rectifier units

[16]) R. Arce *et al.*, Rev. Sci. Inst. **23** (1952) 441.

of which the circuit diagram is shown in fig. 8. Each unit, working from the three phase grid system, delivers approximately 500 mA. The — 150 V power unit is stabilized and delivers approximately 100 mA.

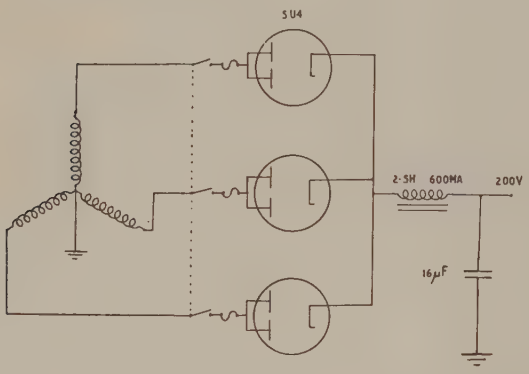

Fig. 8. Rectifier unit.

3.7. ADJUSTING AND TESTING THE CIRCUIT

A simple pulse generator shown in fig. 9 is used to test the entire circuit. Twelve output

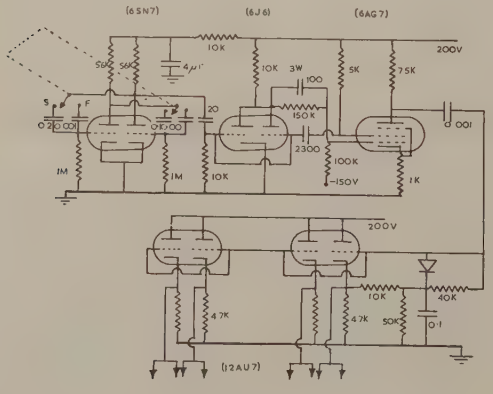

Fig. 9. Pulse generator.

terminals are available. The rate at which pulses are delivered can be changed by means of a switch. In the "slow" position, a pulse is delivered approximately every two seconds whereas approximately 133 pulses per second are delivered in the "fast" position. Each selector circuit is adjusted with the pulse generator in the "fast" position by adjusting the grid bias of V_6 for satisfactory discrimination at O_2 between single and multiple pulses. The final selectors are adjusted in a similar manner by adjusting the grid bias of V_4 (fig. 5).

The sensitivity of the anti-coincidence univibrator is adjusted by means of the potentiometer in its grid circuit. With the pulse generator still in the "fast" position, the suppressor is adjusted by changing the grid bias of V_4 in fig. 6. The power circuit is adjusted with the pulse generator in the "slow" position by adjusting the grid bias of V_2 (fig. 7). The voltage of the suppressor grids of the 6SJ7's of the selector circuits are set to — 70 volts.

The circuits which flash the neons are adjusted by decreasing the grid bias of the right half of V_2 (fig. 4) until the six neons corresponding to this circuit are all just extinguished. The action of the neons is tested by simulating desired events by means of the pulse generator, which for this test, is set in the "slow" position.

The performance of the entire circuit is tested periodically for satisfactory operation by controlling the abovementioned adjustments. The circuit requires very little attention once it is properly adjusted.

Acknowledgments

Thanks are due to Mr. J. J. Henning and Mr. D. P. du Plessis who contributed to this experiment in the early stages. Thanks are also due to Mr. P. I. Jongbloed for the technical assistance he has offered.

This work was made possible by a grant by the South African Council for Scientific and Industrial Research.

NUCLEAR INSTRUMENTS 3 (1958) 285–291; NORTH-HOLLAND PUBLISHING CO. – AMSTERDAM

HODOSCOPE SYSTEM FOR EXPERIMENTS ON THE SCATTERING OF COSMIC RAY μ-MESONS

PART II — PERFORMANCE OF THE HODOSCOPE

M. A. MEYER and J. A. M. DE VILLIERS

Physics Department, University of Potchefstroom, South Africa

Received 25 August 1958

The performance of the hodoscope which is described in the previous publication, is analyzed in detail. Spurious scattering is shown to be about 0.1% of the total counting rate. This inefficiency arises almost entirely from casual coincidences.

1. Recording Characteristics

1.1. COINCIDENCES BETWEEN THE COUNTER SYSTEMS A AND B

Coincidences between the various counter systems were recorded in order to gain some insight in the recording characteristics of the hodoscope which is described in the previous publication. The results obtained in these experiments are primarily concerned with the variation of the intensity of the cosmic ray μ-mesons with the vertical and the geometrical effects involved in the rate of recording.

It was possible to obtain information regarding the variation of the cosmic ray intensity with the vertical for all single particles which pass through the counter systems A and B. The direction of the incoming radiation with the vertical will be denoted by θ or by the projected angles α and β (fig. 1). These angles are related by the expression

$$\cos\theta = \cos\alpha \cos\beta \ .$$

The results obtained are shown in fig. 2, in which the observed intensity is plotted against the projected angle of incidence. The curve represents the intensity calculated from expressions derived in the appendix. These calculations are based on the assumption that the intensity of the incident particles can be represented by

$$I = I_0 \cos^n\theta \ .$$

The curve shown in fig. 2 is that calculated for $n = 3$. The break in the curve represents the onset of a shadow effect and occurs at an angle β for which $\tan\beta = (a - b)/z$ where $2a$ and $2b$ represent the dimensions of the squares A and B respectively and z the vertical distance between these squares. When $\tan\beta > (a - b)/z$ the particles are received by a fraction of the surface B. This results in a rapid decrease of the

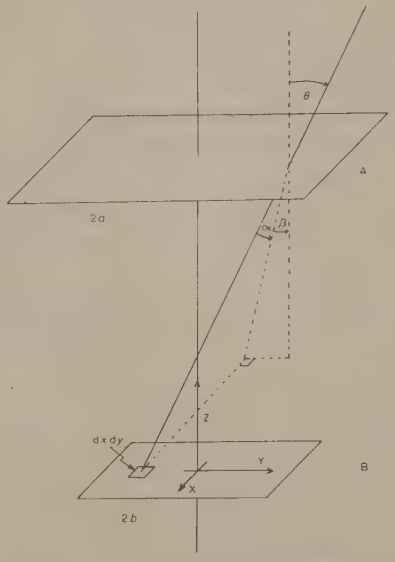

Fig. 1. The projected angles of incidence.

number of particles with increasing β. On the other hand, a particle for which $\tan\beta > (a + b)/z$ cannot be recorded as it is impossible for such a particle to pass through A and B simultaneously.

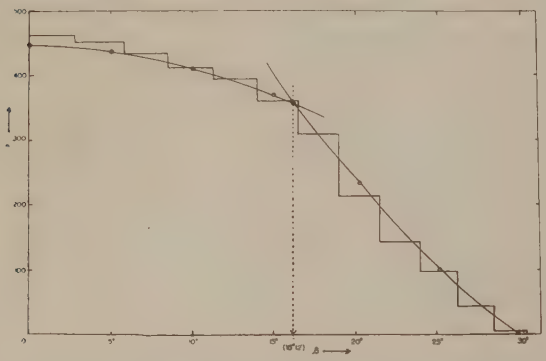

Fig. 2. The recorded intensity as a function of the angle β recorded with the counter systems A and B in coincidence.

1.2. COINCIDENCES BETWEEN THE SYSTEMS A, B, C, AND D IN ANTICOINCIDENCE WITH THE SYSTEM E

The distribution with the vertical of the particles passing through the counter systems A, B, C and D but not through the counter

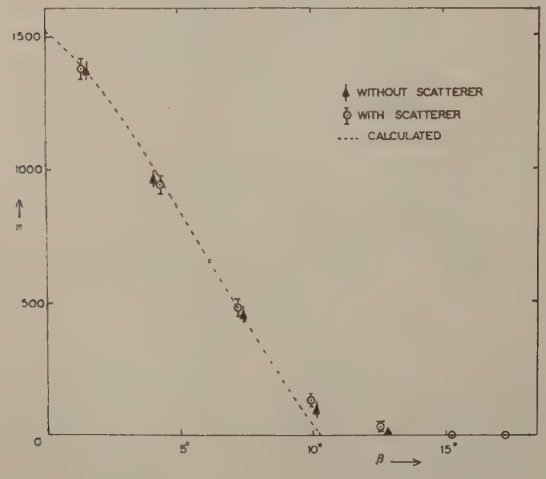

Fig. 3. Distribution of (A, B, C, D, –E)-particles with the vertical.

system E was determined. These events will be denoted by (A, B, C, D –E). The results with and without a 1 cm lead scatterer are shown in fig. 3. As will be noted, the scatterer produces a slight tail. The curve was calculated from an expression given in the appendix and assuming $n = 2$. A smaller value for n than found in the previous experiment was expected on the grounds that the energy of the particles recorded ranged from 300 MeV to 1200 MeV whereas particles having an energy greater than 100 MeV were recorded in the previous experiment.

1.3. RATE OF RECORDING

The rate of recording was analyzed by measuring different coincidence rates such as (A, B, C), (A, B, C, D) and (A, B, C, D, –E) for single as well as the combined rate for single and multiple particles. These results are shown in table 1. Particles included in the events (A, B, C) included particles having an energy greater than 100 MeV, whereas particles included in the events (A, B, C, D) have energies greater than 300 MeV. Coincidences (A, B, C, D, –E) involve particles having an energy between 300 and 1200 MeV. These rates were compared with measurements which are being carried out in this laboratory by means of a cosmic ray telescope. The agreement was found to be satisfactory.

TABLE 1

	Counting rate/hour		
	(A, B, C)	(A, B, C, D)	(A, B, C, D, –E)
Combined and multiple particle rate	338	231	99
Single particle rate	268	200	83
Difference between experimental values	70	31	16
Photographs showing more than one particle	67	32	14

2. Circuit Characteristics and anomalous Photographs

2.1. COINCIDENCE CIRCUIT

The resolving time of the coincidence circuit was determined and found to be 6.5 μsec.

This result allows one to estimate the rate at

which casual coincidences will be recorded. The rate of casual coincidences between n independent counters or counter trays with individual counting rates $N_1, N_2, \ldots N_n$ is given by

$$n_c = nN_1N_2 \ldots N_n t_0^{n-1} + \text{terms of higher order in } t_0,$$

where t_0 is the resolving time. It is sufficient to neglect higher order terms under practical conditions. Also, since the resolving time in this case is 6.5 μsec, two fold casual coincidences alone need be considered. Events which are geometrically allowed to lead to such events are given in table 2. An event indicated for example by (A, B) + (C, D, –E) involves a two-fold coincidence in which one particle passes through the systems A and B and another independent particle which passes through the systems C and D without passing through E.

TABLE 2

Event	Spurious rate per hour
(A, B) + (C, D, –E)	0.11
(A, B, C) + (D, –E)	0.063
(A, C, D, –E) + B	0.023
Total casual rate	0.196

The master pulse resulting from these casual coincidences will vary in size. Although all of them will be of sufficient magnitude to actuate the recording circuit, some of them will not be of sufficient size to fire the neons, or, because of the difference in the striking voltage of the neons, at most some of the neons corresponding to the counters through which the particles have passed. If it is assumed that the pulses must overlap for at least 4 μsec in order to yield a master pulse of sufficient magnitude to fire all the neons, then the number of photographs which will be interpreted as being due to the passage of a single particle is $0.196 \times 5/13$ per hour $= 0.076$/h. This rate will form part of the background against which the scattering will have to be studied. These events will be called "spurious" counts. The rest of the photographs, 0.12/h, will be rejected as these will exhibit less than six fired neons. Such photographs and photographs showing more than six fired neons will be called "anomalous".

2.2. ANTICOINCIDENCE CIRCUIT

The efficiency of the anti-coincidence circuit was investigated in the following manner. The passage of a single particle accompanied by a second particle through the hodoscope was simulated by means of the pulse generator at the rate of 133/sec. The resulting anticoincidence pulse at the suppressor suppresses the coincidence pulse, which being delayed, arrives 4 μsec later. Under these conditions, the coincidence pulse is fully suppressed. If in addition, random pulses from another source such as the counter system E are fed via the anticoincidence univibrator to the suppressor, then some of the coincidence pulses stimulated by the pulse generator, are not suppressed and the recording circuit is actuated at the rate of 0.46/sec. The cause of this effect was shown to be a characteristic of the anti-coincidence univibrator to produce pulses of shorter duration than normally when triggered within a short time interval following a previous triggering pulse. The time interval after an anti-coincidence pulse has occurred in which a coincidence pulse will be recorded although the latter is accompanied by an anti-coincidence pulse, is given by

$$\tau_1 = 0.46/174 \times 133 = 20 \ \mu\text{sec}$$

where the rate at which the system E delivers pulses to the anti-coincidence univibrator is 174/sec.

An accompanied particle which passes through the hodoscope during this interval of 20 μsec following an anti-coincidence pulse from the system E will give rise to a photograph on which any number of neons from zero upwards are glowing depending on the size of the master pulse and the number of particles passing through the hodoscope. An estimate of the rate at which these events will be recorded can be made as follows. During actual operation of the hodoscope, the rate at which pulses arrive at the anti-coincidence univibrator from the system

E is 174/sec, whereas the number of accompanied particles which pass through the hodoscope but not through the system E is 16/h (table 1). Consequently, the rate at which anomalous photographs will be obtained from this cause is 0.056/h.

2.3. LOSS OF EVENTS

Since the rate at which anti-coincidence pulses arrive at the suppressor is high (174/sec), some anti-coincidence pulses will overlap a few coincidence pulses with the result that true events be lost at a rate of

$$\tau_2 \, n_a \, n_c$$

where n_a and n_c are the rate at which anti-coincidence and coincidence pulses arrive at the suppressor respectively, and τ_2 the time interval during which the suppressor blocks the passage of a coincidence pulse. This quantity was determined in a separate experiment and found to be 12 μsec. Consequently, with $n_c = 83$/h (table 1), the loss of actual coincidences is 0.17/h.

Another source of losses lies with the camera magnet. The time required after the shutter closes until the next photograph can be taken was found to be 0.11 sec. The events lost during this interval is 0.21/h.

The total loss of events is therefore 0.38/h, or approximately 0.45% of the true events.

2.4. ANOMALOUS PHOTOGRAPHS

If a coincidence pulse is partly suppressed by an anti-coincidence pulse, a master pulse will be formed which is smaller than normally. This effect constitutes a third source of anomalous photographs. An estimate of the rate at which these photographs will be obtained can be made as follows. It is reasonable to assume that a master pulse of which the height is insufficient to strike all the neons will result whenever an anti-coincidence pulse follows a coincidence pulse within about 4 μsec. Similarly, it will be assumed that an anomalous photograph will result whenever a coincidence pulse dies away within about 4 μsec after the decay of an anti-coincidence pulse. The rate at which anomalous photographs will be obtained from this source is therefore.

$$174 \times 8 \times 10^{-6} \times 83/\text{h} = 0.116/\text{h} \, .$$

The fact that the camera shutter is open for 0.03 sec constitutes another source of anomalous photographs which will show two particles passing through the hodoscope. The rate at which these events will be recorded is 0.06/h.

A last source of anomalous photographs arises from the fact that the neons glow, on the average, for 0.25 seconds whereas the camera magnet requires 0.14 seconds before the next photograph can be taken. If a second particle passes through the hodoscope during the interval from 0.14 seconds to 0.25 seconds after a preceding particle, then a photograph will be obtained in which two particles will appear to pass through the hodoscope. A characteristic of these photographs will be the fact, one of the trajectories will be identical with the trajectory shown on the preceding photograph. The rate at which these photographs will be obtained is $83^2 \times 0.11/3600$ per hour $= 0.21$/h.

The total rate of anomalous photographs, obtained by adding the above-mentioned rates, is 0.56/h. The observed rate is 0.58/h.

3. Spurious Records

The large angle tail of the scattering distribution is of considerable importance. Here the number of particles is small and since most spurious processes give rise to events appearing in the tail, such contamination must be assessed. A spurious record will be a photograph on which one counter only, in each of the six layers of the system A, B, and C is discharged, and at least one counter in the system D is discharged when this event has not arisen from the passage of a single particle through the hodoscope. Particles with strong nuclear interaction such as protons and π-mesons interacting with the scatterer, knock-on electrons, extensive showers and casual coincidences will simulate μ-mesons scattered through large angles. The last scource of spurious counts has already been discussed

under § 2.2. and found to be approximately 0.08/h or 0.1% of the total counting rate.

3.1. DETERMINATION OF THE SPURIOUS BACKGROUND

The total spurious background was determined by recording coincidences (A, B, C, D, –E) without the scatterer. In the absence of spurious effects, no particles should be detected having one of the projected angles of incidence greater than 10° with the vertical. Particles having projected angles greater than 10° were classified as spurious records. The rate at which these events were recorded was found to be 0.6% without the screening counters (i.e. sixteen counters placed around the beam between the counters systems B and C) in anti-coincidence and 0.4% with the screening counters in anti-coincidence after correcting for the fact that these events will occur over all values of β with equal probability. This is considerably more than can be accounted for in terms of casual coincidences. The spurious rate remained unaltered by placing a 1 cm lead scattered below the system B. The total spurious background decreased to 0.1% by placing the scatterer above the system B. This rate can therefore be accounted for entirely in terms of casual coincidences.

3.2. NUCLEAR INTERACTIONS IN THE SCATTERER

An estimate of the upper limit of these effects can easily be made. About 1% of the cosmic ray particles of the relevant energy are protons. About 60% of these protons will penetrate the 8 cm lead absorber placed above the hodoscope and about 7% of these will interact with the 1 cm lead scatterer. This event will be interpreted as a large angle scattering event if one particle of this interaction has sufficient energy to penetrate the 14 cm lead absorber placed between the counter systems C and D. If this is assumed and account is taken of the absorption of the secondary particles in the lead between the counter systems B and C, then the contribution of this effect to the spurious background can only be about 0.015%.

The effect of π-mesons may also be deduced. Practically all the π-mesons will be produced in the lead absorber, above the hodoscope. If it is assumed that each proton interaction in this absorber leads to one π-meson of sufficient energy to reach the scatterer, then the number of π-mesons which will interact with the scatterer is about 0.04% of the total beam. Assuming that each interaction in the scatterer yields one particle of sufficient energy to penetrate the absorber between the counter systems C and D, then the contribution of π-mesons to the spurious rate will be 0.01% if account is taken of the absorption of the secondary particles in the lead between the counter systems C and D.

Clearly, the total contribution of proton and π-meson effects will be much less than 0.025% and probably not more than about 0.003% of the total beam if account is taken only of the geometry and the requirement that the particles should pass unaccompanied through the hodoscope. This is much less than the observed spurious rate.

3.3. KNOCK-ON ELECTRONS

A spurious large angle scattering will result when a meson which passes directly from the system A to the system C, without passing through the system B, produces a knock-on electron of sufficient energy to penetrate the counters of the system B in either the lead above the hodoscope or in the counter walls of the system A. The expected number of secondary electrons of the required energy, produced in the lead and counter walls, is about 0.02 per meson. The estimated spurious background was found to be approximately 0.4% of the total counting rate if account is taken of the geometry of the apparatus and the rate at which particles pass directly from the system A to the system C. If this rate is added to the spurious rate due to casual coincidences one finds 0.5% for the total spurious rate which is practically the entire background of 0.6% found without the scatterer or with the scatterer placed below the system B.

The rate of spurious events expected with a 1 cm lead scatterer placed immediately above

the system B is about 0.05%. If this rate is added to the spurious rate due to casual coincidences, one finds 0.15% for the total spurious rate. This is practically the total spurious rate of 0.1% found experimentally with the scatterer placed above the system B. It is therefore concluded that, with the scatterer placed below the system B, the entire spurious effect can be accounted for in terms of knock-on electrons and casual coincidences. When the scatterer is placed above the system B, the spurious background results almost entirely from casual coincidences.

Acknowledgments

This work was made possible by a grant by the South African Council for Scientific and Industrial Research.

Appendix

A.1. COINCIDENCES BETWEEN THE COUNTER SYSTEMS A AND B

Let A and B (fig. 1) represent the counter systems A and B respectively and let these systems be separated by a distance z. Let the dimensions of A be $2a$ and of B be $2b$. The angle of incidence θ, is related to the projected angles α and β by

$$\cos\theta = \cos\alpha\cos\beta \ .$$

The elementary solid angle is given by

$$\mathrm{d}\omega = \cos\alpha\,\mathrm{d}\alpha\,\mathrm{d}\beta \ .$$

If the intensity of the incident radiation can be represented by

$$I = I_0\cos^n\theta \qquad \text{(A1)}$$

then the rate at which particles pass through an area $\mathrm{d}x\,\mathrm{d}y$ of the square B from the direction θ is given by

$$I_0\cos^{n+1}\beta\,\mathrm{d}\beta\,\mathrm{d}x\,\mathrm{d}y\cos^{n+2}\alpha\,\mathrm{d}\alpha$$

the total number of particles recorded having a projected angle of incidence between β and $\beta + \mathrm{d}\beta$ is therefore

$$N_n(\beta)\,\mathrm{d}\beta = I_0\cos^{n+1}\beta\,\mathrm{d}\beta\int_{-b}^{Y_1}\mathrm{d}y\int_{-b}^{+b}\mathrm{d}x\int_{\alpha_1}^{\alpha_2}\cos^{n+2}\alpha\,\mathrm{d}\alpha$$

where

$$\alpha_2 = \tan^{-1}\left(\frac{a-x}{z}\cos\beta\right) \quad \alpha_1 = -\tan^{-1}\left(\frac{a+x}{z}\cos\beta\right)$$

$$y_1 = b \quad \text{when} \quad \tan\beta < (a-b)/z$$

$$y_1 = a - z\tan\beta \quad \text{when} \quad \tan\beta > (a-b)/z \ .$$

Therefore,

$$\tan\beta < (a-b)/z\text{:}$$

$$N_n(\beta)\,\mathrm{d}\beta = 2\,bI_0\cos^{n+1}\beta\,\mathrm{d}\beta\,I(n) \qquad \text{(A2)}$$

$$\tan\beta > (a-b)/z\text{:}$$

$$N_n(\beta)\,\mathrm{d}\beta = (a+b-z\tan\beta)\,I_0\cos^{n+1}\beta\,\mathrm{d}\beta\,I(n) \qquad \text{(A3)}$$

where

$$I(n) = \int_{-b}^{+b}\mathrm{d}x\int_{\alpha_1}^{\alpha_2}\cos^{n+2}\alpha\,\mathrm{d}\alpha \ .$$

This expression was integrated for $n = 0$, 2, 3 and 4 and yielded

$$I(0) = \frac{z}{\cos\beta}f(\xi,\eta) \qquad \text{(A4)}$$

$$I(2) = \frac{z}{4\cos\beta}[3f(\xi,\eta) - g(\xi,\eta)] \qquad \text{(A5)}$$

$$I(3) = \frac{2z}{15\cos\beta}h(\xi,\eta) \qquad \text{(A6)}$$

$$I(4) = \frac{z}{4\cos\beta}\left[\frac{5}{2}f(\xi,\eta) - \frac{1}{6}\phi(\xi,\eta)\right], \qquad \text{(A7)}$$

where

$$f(\xi,\eta) = \xi\tan^{-1}\xi - \eta\tan^{-1}\eta \qquad \text{(A8)}$$

$$g(\xi,\eta) = \frac{1}{1+\xi^2} - \frac{1}{1+\eta^2} \qquad \text{(A9)}$$

$$h(\xi,\eta) = \frac{8\xi^4 + 12\xi^2 + 3}{(\xi^2+1)^{3/2}} - \frac{8\eta^4 + 12\eta^2 + 3}{(\eta^2+1)^{3/2}} \qquad \text{(A10)}$$

$$\phi(\xi,\eta) = \frac{5\xi^2 + 7}{(\xi^2+1)^2} - \frac{5\eta^2 + 7}{(\eta^2+1)^2} \qquad \text{(A11)}$$

$$\xi = \frac{a+b}{z}\cos\beta \ , \qquad \eta = \frac{a-b}{z}\cos\beta \ . \qquad \text{(A12)}$$

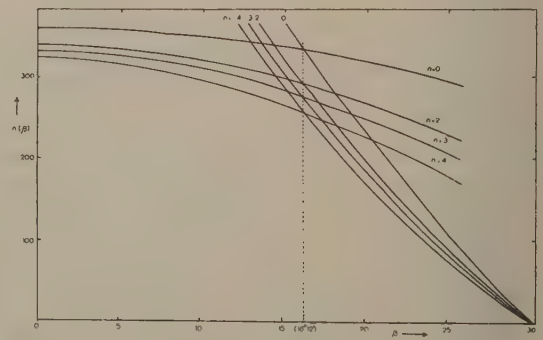

Fig. A.1. Calculated distribution of (A, B)-particles.

Eqs. (A2) and (A3) are represented in fig. A.1 for different values of n. The break in the curve represents the onset of a shadow effect and occurs at an angle β for which $\tan\beta = (a-b)/z$.

A.2. COINCIDENCES BETWEEN THE COUNTER SYSTEMS B AND C

The corresponding expressions for coincidences between the layers B and C can be obtained from the above formulae by putting $a = b$ and consequently $\eta = 0$. One therefore finds

$$N_0(\beta)\,\mathrm{d}\beta = I_0(2b - z\tan\beta)\, z\,\mathrm{d}\beta\, f_0(\xi) \qquad \text{(A13)}$$

$$N_2(\beta)\,\mathrm{d}\beta = \tfrac{1}{4} I_0(2b - z\tan\beta)\, z\cos^2\beta\,\mathrm{d}b\,[3 f_0(\xi) + g_0(\xi)] \qquad \text{(A14)}$$

$$N_3(\beta)\,\mathrm{d}\beta = \frac{2}{15} I_0(2b - z\tan\beta)\, z\cos^3\beta\,\mathrm{d}\beta\, h_0(\xi) \qquad \text{(A15)}$$

$$N_4(\beta)\,\mathrm{d}\beta = \tfrac{1}{4} I_0(2b - 2\tan\beta)\, 2\cos^4\beta\,\mathrm{d}\beta \left[\frac{5}{2} f_0(\xi) - \frac{1}{6}\phi_0(\xi)\right], \qquad \text{(A16)}$$

where

$$f_0(\xi) = \xi\tan^{-1}\xi$$

$$g_0(\xi) = \xi^2/(1+\xi^2)$$

$$h_0(\xi) = \frac{8\xi^4 + 12\xi^2 + 3}{(\xi^2+1)^{3/2}} - 3$$

$$\phi_0(\xi) = \frac{5\xi^2 + 7}{(\xi^2+1)^2} - 7\,.$$

$$\xi = \frac{2b}{z}\cos\beta\,.$$

The expressions (A13) to (A14) are also valid for coincidences between the counter systems A, B and C and between the systems A, B, C and D since the systems A and D cover the entire solid defined by B and C.

NUCLEAR INSTRUMENTS 3 (1958) 292–297; NORTH-HOLLAND PUBLISHING CO. – AMSTERDAM

ELECTRONIC APPARATUS FOR THE MEASUREMENT OF DYNAMIC MAGNETIC FIELDS

I. F. QUERCIA

Istituto Nazionale di Fisica Nucleare, Laboratori di Frascati

Received 12 August 1958

An apparatus is described which reproduces with a staircase voltage waveform a magnetic field rising between 0 and about 120 gauss. The device is well suited for the measurement of the instantaneous value of the magnetic field in the gap of an electron synchrotron. It consists of a peaking strip magnetic probe, and an electronic apparatus.

1. Introduction

The problem of measuring the instantaneous value of a magnetic field which is changing in time arises rather frequently in research and in technological work. Many devices have been developed by different authors, which are well suited for particular situations[1]). The apparatus described in the present paper has been developed with the purpose of measuring the rising magnetic field in the gap of the 1 GeV Frascati Electron-synchrotron between 0 and about 120 gauss. The apparatus produces a voltage wave form which accurately reproduces the magnetic field increasing with rates of rise between 0.05 gauss/μs and 0.3 gauss/μs, and is well suited, e.g. for controlling the frequency modulation program of the Radio Frequency accelerating system of the Synchrotron. We think that, with some modifications, it would be possible with a similar apparatus to track magnetic fields rising to higher values; in that case the apparatus would be useful for many other applications, e.g. the programming of frequency modulation in Proton Synchrotrons.

The apparatus consists of a "magnetic probe" and an "electronic device", which will be described in the following paragraphs.

[1]) J. L. Symonds, Methods of measuring strong magnetic fields, Rep. Progr. in Phys. 18 (1955) 83 presents a very useful summary of the different technical approaches to the problem, developed up to that date.

2. Magnetic Probe

The magnetic-sensitive probe is a biased "peaking strip"; its pulses are used to drive an electronic apparatus. As is well known[2,3]), a "peaking strip" is a length of wire of a magnetic material with high permeability; in our case it is a wire of "Ultraperm 10", 20 mm in length, 0.025 mm in diameter. The static hystereris loop of such a wire is very narrow so that only a few hundredths of an oersted are required to reverse the direction of the magnetic polarization inside the wire[4]). In a coil wound around this wire a voltage pulse is induced every time the magnetic polarization of the wire is quickly reversed. The high permeability magnetic wire and the pickup coil together are usually called a "peaking strip" (referred to as PS in the following).

In our case the PS is surrounded by a coil in which a biasing current can be injected. The voltage pulse is produced by the PS when the sum of the field to be measured and the field due to the biasing coil, crosses the zero value, reversing the magnetic polarization of the wire.

[2]) J. M. Kelly, Rev. Sci. Instr. 22 (1951) 256.

[3]) S. Giordano, G. K. Green and E. J. Rogers, Rev. Sci. Instr. 24 (1953) 848.

[4]) Wires of "Ultraperm 10" were furnished by: Vacuumschmelze Aktiengesellschaft Hanau, Gruener Weg 37 – West Germany. The wire was contained in a quartz tube as shown in fig. 1 and was cemented with araldit to the tube according to the procedure described by: G. Diambrini, Nuovo Cimento 3 (1956) 336.

In this way a voltage pulse is produced by the device, every time the field to be measured by the probe, reaches the value of the biasing field. In fig. 1 the dimensions of the probe are

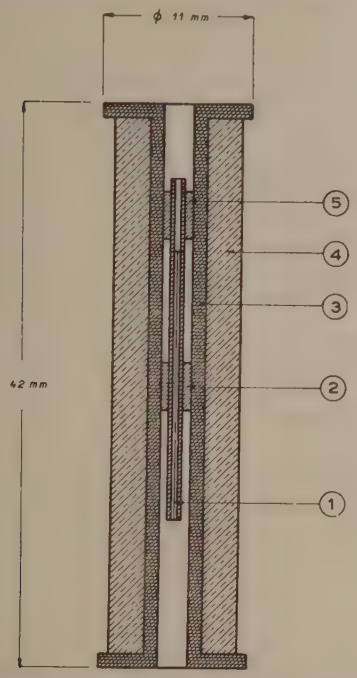

Fig. 1. Magnetic probe. 1. Ultraperm 10 wire, diameter 0.025 mm, length 20 mm contained in a quartz tube ext. dia. 0.9 mm, int. dia. 0.2 mm. 2. Pick up coil, 400 turns of enameled copper wire of dia. 0.05 mm. 3. Plexiglass frame. 4. Bias coil. Copper wire 0.2 mm dia. 750 turns/cm. 5. Compensating coil, see n. 2.

given together with the characteristics of the pickup and biasing coils[5]).

3. Electronic Apparatus

The electronic apparatus injects a current step in the biasing coil, every time it is triggered by a positive pulse from the PS. If we suppose that the rest bias current corresponds to a magnetic field $-H_0$, the first pulse is produced by the PS when the measured field reaches the value $B_0 = +H_0$. This first pulse triggers the electronic device, and a step of current is injected in the bias coil; the biasing field is thus raised to the value $H_1 = -(H_0 + \Delta H)$. While the bias field rises from $-H_0$ to $-H_1$, the measured field increases by an amount ΔB. If ΔB is less than ΔH, the total field at the PS is reversed and a negative pulse is generated. Now the PS is ready to produce a second positive pulse when the measured field reaches the value $B_1 = -H_1$. This second pulse causes a second step of current to be injected in the bias coil, and the process in repeated (see fig. 2). In this way the biasing field is increased by steps, of amplitude ΔH, each step being triggered by the PS which in turn fires every time the measured field is increased by an amount $\Delta B = \Delta H$. The

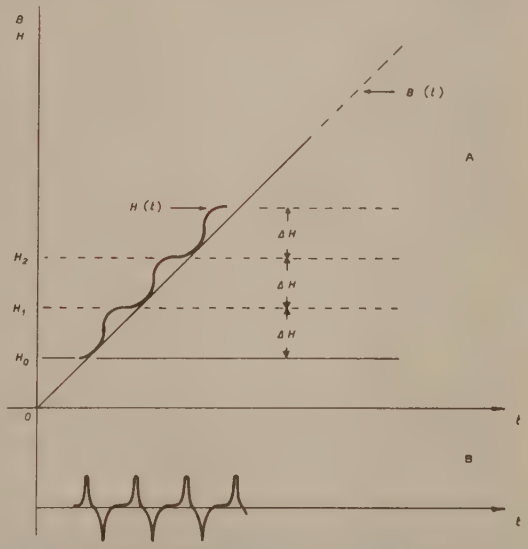

Fig. 2. Diagrams showing the process of generation of the staircase waveform. A. Measured field $B(t)$, Biasing field $H(t)$. B. Pulses from the peaking strip.

"staircase" formed by the successive steps reproduces the shape of the function of time $B(t)$, with an absolute error of the order of ΔH.

The block diagram of the apparatus is shown in fig. 3. The PS pulses have an approximate gaussian shape, with about 3 μs rise time in a field rising at a rate of more than 0.1 gauss per μs; the amplitude of the pulses is about 35 mV. These pulses are amplified by a conventional fast amplifier, having a gain of 200, and a rise time of about 0.5 μs.

[5]) Note that a compensating coil ((5) in fig. 1) is connected in series and in opposition to the pickup coil; this reduces the voltages induced in the pickup coil due to the coupling between pickup and biasing coils.

The pulses coming out from the amplifier are injected in a Schmitt amplitude discriminator; this selects the positive pulses from the negative ones and from the background.

The leading edge of the step is a linear ramp having a slope:

$$\frac{V_1}{\tau}.$$

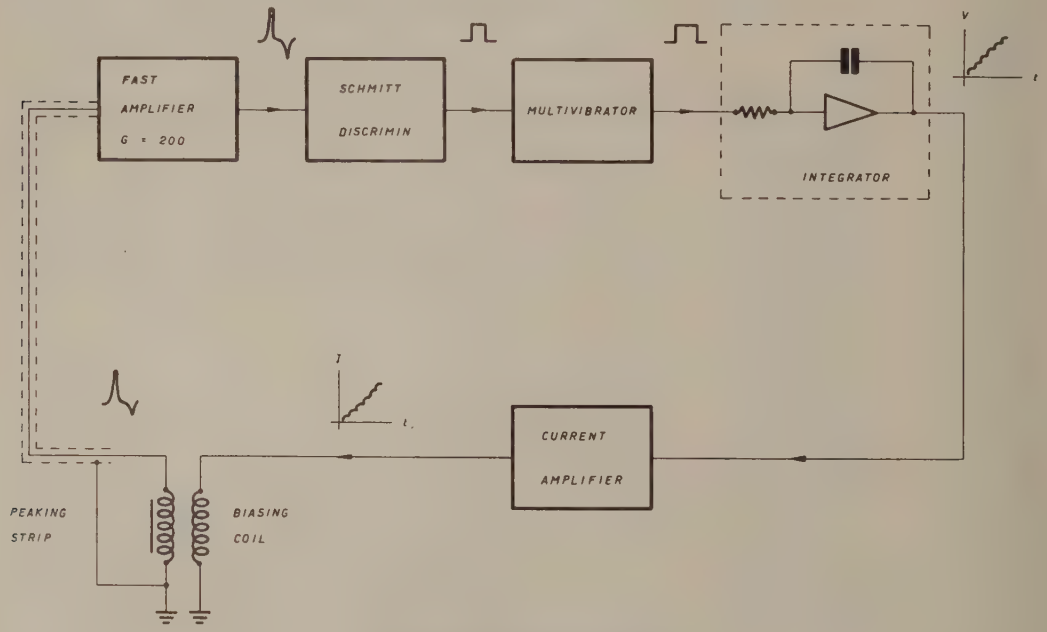

Fig. 3. Block diagram of the apparatus.

The pulses from the Schmitt circuit are used to trigger a multivibrator, which produces standard negative pulses. The amplitude of these pulses can be varied between 0 and 8 volt, by means of the 10 kΩ potentiometer in the plate circuit of the second tube; the duration of these pulses can be adjusted between 2 and 8 μs, by means of the 10 kΩ potentiometer in the grid-cathode circuit.

The negative rectangular pulses from the multivibrator are injected in to an electronic integrator having a time constant $\tau = RC$. The integration of each pulse produces a step of voltage, of amplitude:

$$V_u = \frac{V_i}{\tau} T$$

at the output; here V_1 is the amplitude of the integrated pulse, while T is the duration of the pulse.

Because of the finite gain G of the amplifier in the integrating circuit, the steps of voltage at the output decay exponentially with a time constant $\theta = G \cdot \tau$. The diagram of the apparatus is given in fig. 4. The integrating time constant is $\tau = 100$ μs, so that by changing the time duration of the pulses from the multivibrator, the voltage steps can be adjusted between 0.14 and 0.56 volt. The gain of the integrating amplifier is about $G \cong 50$ so that the decay time constant is about $\theta \cong 5000$ μs.

In fig. 4 the details of the Schmitt discriminator, the multivibrator and the integrating circuit are given.

The voltage steps from the integrating circuit are injected in a negative feed-back current amplifier, shown in fig. 5. The current in the biasing coil is controlled by the EL34 power tube.

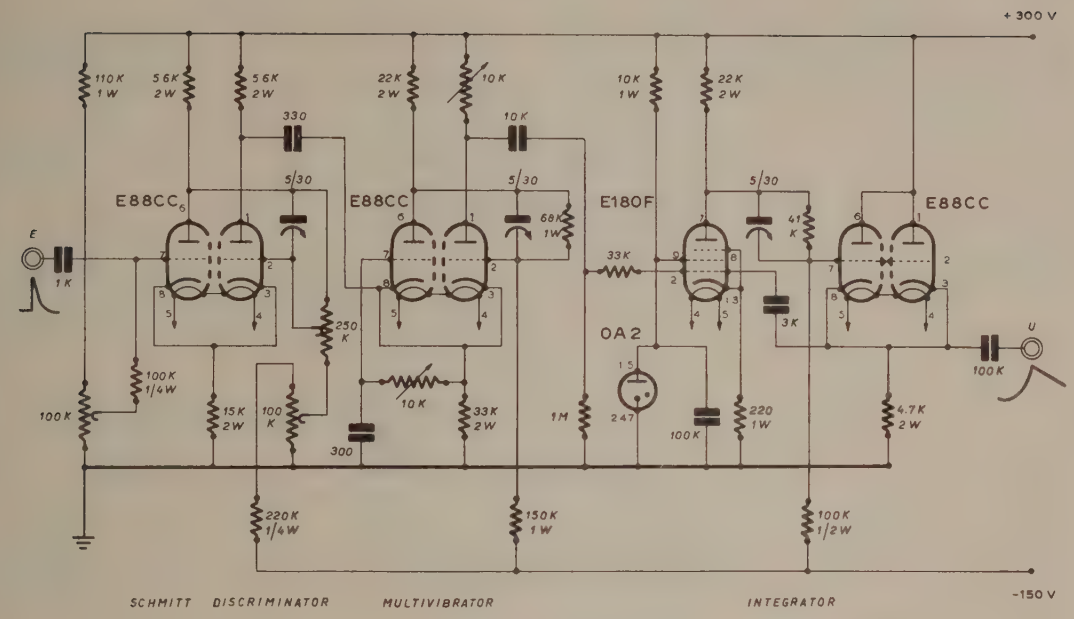

Fig. 4. Voltage staircase generator.

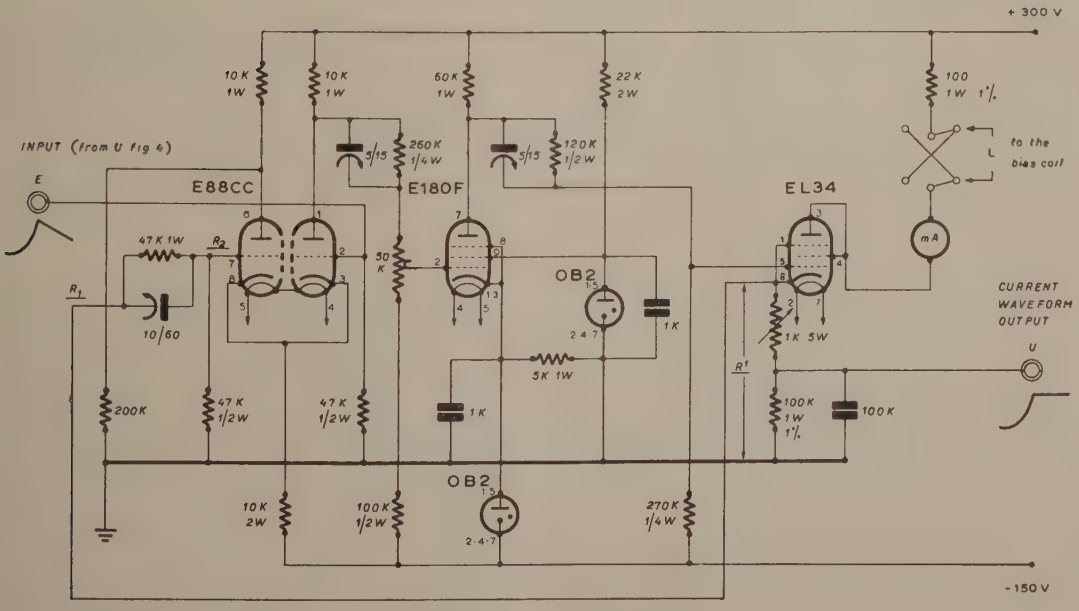

Fig. 5. Current amplifier.

The current gain of this amplifier may be calculated as follows: the negative feed-back tends to cancel any voltage difference between the two grids of the input differential amplifier (tube E88CC).

If V_1 is the voltage at the input grid, a current is developed by the power tube so that the voltage fed back to the second input of the differential amplifier is just equal to V_1. The voltage fed back is given by

$$iR \frac{R_2}{R_1 + R_2},$$

so that the current gain is:

$$\frac{i}{V_1} = \frac{R_1 + R_2}{R_2} \frac{1}{R}.$$

The output impendance of the current amplifier is a rather important parameter in our circuit for two reasons. First: the bias coil has an inductance of about $L = 5$ mH, and a time constant $t = L/r$ where r is the output resistance of the current generator feeding the current in the coil; in our case it is necessary to have a time constant $t < 1$ μs, so that an output resistance $r > 5\,000$ is needed. Second: the changing magnetic flux through the bias coil induces variable voltages at the terminals of the coils, the current in the coil must be independent from such voltages; this requirement is achieved by letting the current source have a very large output resistance.

A current feed-back amplifier as an output impedance given by[6])

$$Z_{fb} = Z\,(1 - \mathscr{L})$$

where $\mathscr{L}$ is the loop gain of the amplifier with the output (coil) terminals short circuited, and: Z is the output impedance of the power tube.

In our case the loop gain is not less than 1 000, assuming an output resistance of the triode connected EL34 of $Z \cong 10\,000$ ohm, the output impedance of the current amplifier is of the order of 10 megaohms, large enough for our purposes.

[6]) See e.g. T. S. Gray, Applied electronics, 2nd Ed. (John Wiley & Sons, Inc., 1954) p. 587.

[7]) These values have been measured by Dr. G. Diambrini-Palazzi, whom we wish to thank for these data.

4. Performance of the Apparatus

Tests have been made by putting the probe at various distances in the fringing field of a magnet, excited by 50 c/s A.C. current. The peak value of the field in the gap of the magnet was above 1 500 gauss, so that, in the fringing field, rates of rise of the field the order of 0.4 gauss/μs were easily reached.

With a rate of rise of the field at the probe site of 0.1 gauss/μs, a field of 90 gauss is reproduced by 29 steps, with an average value of $\Delta H = 3$ gauss/step (see fig. 6).

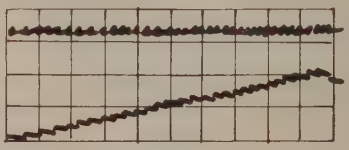

Fig. 6. (sweep length = 1 ms.) Amplified pulses from peaking strip. 90 gauss, 29 steps staircase, $dB/dt = 0.1$ gauss/μs.

With a rate of rise of 0.3 gauss/μs, a field of 90 gauss is reproduced by 14 steps, with an average value of $\Delta H = 6.4$ gauss/step (see fig. 7).

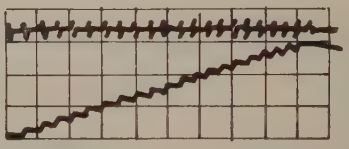

Fig. 7. (sweep length = 0.5 ms.) Amplified pulses from peaking strip. 90 gauss, 14 steps staircase, $dB/dt = 0.3$ gauss/μs.

The different behaviour of the apparatus at different values of the rate of rise of the measured magnetic field is justified by the fact that the value of the coercitive field in the magnetic material used for the peaking strip, increases from the value of about 7 millioersted in the static case, to a value of 1.2 oersted for fields rising at a rate of 0.1 gauss/μs, and to a value of 2.2 oersted for fields rising at a rate of 0.3 gauss/μs[7]).

In fig. 8 the amplified pulses from the peaking strip, together with the corresponding steps of

the staircase waveform, are shown in an enlarged scale. The staircase tracks the current waveform, shown in the photograph by the solid curve,

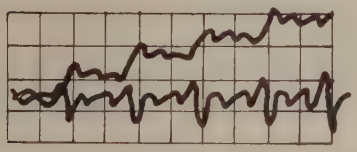

Fig. 8. Enlarged scale sweep 10 μs/□, staircase (v.s. 1 volt/□ = 9 gs/□), pulses (v.s. 10 volt/□).

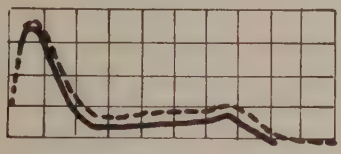

Fig. 9. Staircase wave form tracking a magnetic field produced by injecting in a solenoidal coil a current pulse (solid line). Vertical scale 24.6 gs/□. Sweep 1 ms/□.

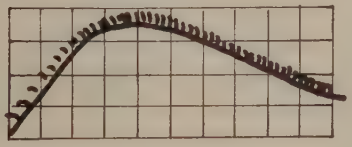

Fig. 10. Some as fig. 9 in enlarged scale. Vertical scale 24.6 gs/□. Sweep 200 μs/□.

In fig. 9 the staircase waveform reproducing a fancy magnetic field, produced by injecting a pulse of current in a solenoidal coil, is shown. with a high degree of accuracy, as is better seen in fig. 10 which is an enlarged part of fig. 9.

NUCLEAR INSTRUMENTS 3 (1958) 298–302; NORTH-HOLLAND PUBLISHING CO. – AMSTERDAM

THE RESPONSE OF A NaI(Tl) CRYSTAL TO MONOERGIC NEUTRONS†

S. M. SHAFROTH, E. N. STRAIT and R. T. CARPENTER††

Northwestern University, Evanston, Illinois

Received 20 September 1958

The response of a $1\frac{3}{4}'' \times 2''$ NaI(Tl) cylinder to neutrons in the pulse height region between 2.5 and 7 MeV gamma energy equivalent was studied as a function of incident neutron energy for a range of neutron energies between room scattered neutrons and 1.162 MeV. The $Li^7(p, n)Be^7$ reaction was used as a source of neutrons since it is relatively free from high energy gamma ray background. Monoergic neutron response curves were obtained for neutron energies of 166 keV, 341 keV, and 469 keV. All other distributions were for proton energies giving rise to two neutron groups. The pulse height distributions were measured for a fixed number of counts of a shielded long counter at each neutron energy. The long counter was calibrated against Ilford C2 emulsions for the case of 1.162 and 0.698 MeV neutrons in order to obtain the neutron flux from the long counter counts. The pulse height distributions are nearly linear between 4 and 6.6 MeV. The extrapolations of these distributions intersect the gamma equivalent axis at approximately the binding energy of the last neutron in I^{128}.

1. Introduction

It has been known for many years that NaI(Tl) crystal scintillation counters respond to neutrons as well as gammas and the low energy response has been given considerable attention in the literature[1,2]). However, the exact characteristics of the response in the pulse height region between 2.5 and 7 MeV gamma equivalent have not been published heretofore, though many laboratories have studied them in connection with individual experiments[3]). Often the neutron response constitutes an undesired background when gamma ray producing reactions are being studied. Such a situation was encountered by one of us (SMS) during an investigation of gamma-gamma coincidences from the $Be^9(d, n)B^{10*}$ (γ) reaction[4]). More recently work in this laboratory[5]) on the Doppler shift of the 3.57 MeV gamma arising from the $Be^9(p, \alpha)Li^{6*}$ (γ) reaction made it desirable to know the pulse height distribution produced by the accompanying neutrons from the competing reaction $Be^9(p, n)B^9$. The general situation is illustrated in fig. 1 where the three peaks from the 3.57 MeV gamma are accompanied by a high energy tail due to gammas arising from neutron capture in the iodine of the NaI crystal. The present work was undertaken in order to permit correction for neutron background.

2. Experimental Procedure

The response of a $1\frac{3}{4}''$ D $\times$ $2''$ NaI(Tl) cylinder mounted on a Du Mont 6292 photomultiplier tube and surrounded by a layer of lead $\frac{1}{16}''$ thick was studied in the pulse height region between 2.5 and 7 MeV gamma equivalent. The response in the region below 2.12 MeV depends on the past history of neutron irradiation because of the beta decay of I^{128} which has a 25 minute half-life. The pulses from the scintillation counter were analyzed by a Radiation Counter Laboratories 256 channel pulse height analyzer. Neutrons were produced by (p, n) reactions in lithium and beryllium, using the proton beam from the Northwestern University electrostatic

† Work supported in part by the National Science Foundation.

†† Now at Argonne National Laboratory.

[1]) Robert B. Day, Phys. Rev. **102** (1956) 767; This paper lists a number of other references.

[2]) V. K. Rasmussen, F. R. Metzger and C. P. Swann, Phys. Rev. **110** (1958) 154.

[3]) L. C. Thompson and J. R. Risser, Phys. Rev. **94** (1954) 941.

[4]) S. M. Shafroth and S. S. Hanna, Phys. Rev. **95** (1954) 86.

[5]) R. A. J. Levesque and S. M. Shafroth, to be published.

accelerator at energies between 1.8 and 3 MeV. The $Li^7(p, n)Be^7$ reaction was chosen as the neutron source for nearly all of the present work because these neutrons are accompanied by relatively few high energy gammas. Targets of natural lithium, 5 to 10 keV thick, were situated at 30° with respect to the proton beam on the opposite side from the scintillation counter, and located such that its center was 2 meters from the target. In order to reduce neutron scattering as much as possible all moveable scattering materials were removed.

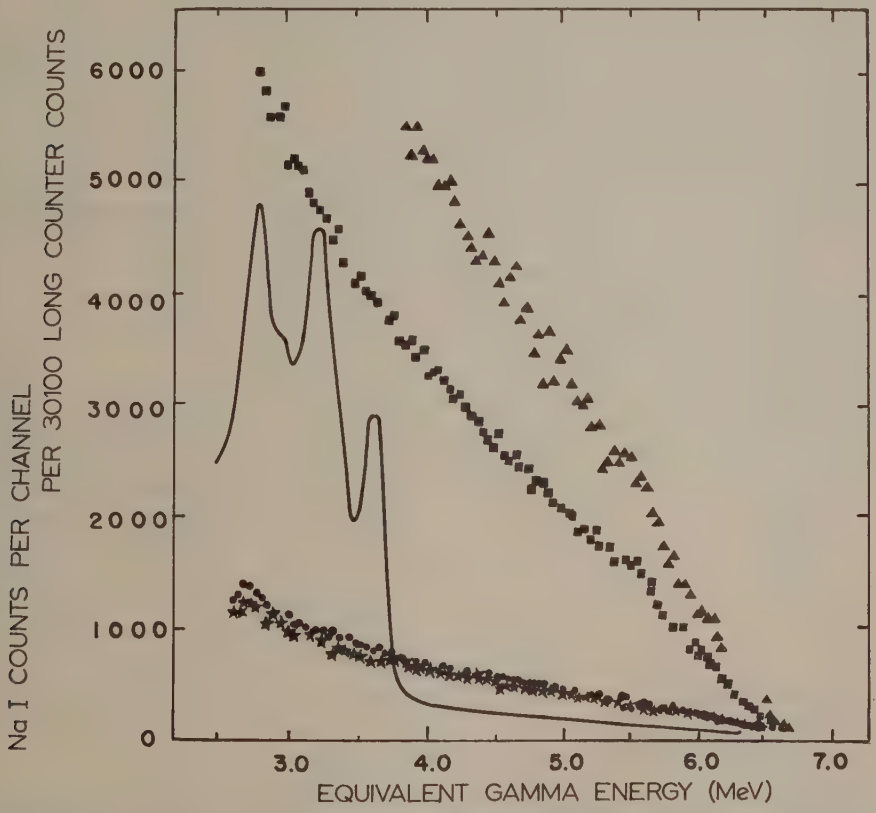

Fig. 1. Pulse height distributions produced in a $1\frac{3}{4}''$ D × 2] NaI(Tl) crystal by various sets of "double energy" neutrons from the $Li^7(p, n)Be^7$ and the $Li^7(p, n)Be^{7*}$ reactions, scattered neutrons, and thick target $Be^9(p, n)B^9$ neutrons. All distributions except the latter are for 30 100 long counter counts.

▲ Room scattered neutrons; ■ E_n 0.7, 75 keV; ● E_n 765, 193 keV; ★ E_n 994, 520 keV; — Be^9 + p ordinates arbitrary.

evaporated onto 0.05 mil nickel foils in the vacuum of the target chamber. The beam stopped in thick tantulum. The scintillation counter was placed at 30° with respect to the proton beam and with its front face 16 cm from the target spot. A shielded long counter of the type described by Hanson and McKibben[6]) was

[6]) A. O. Hanson and J. L. McKibben, Phys. Rev. 72 (1947) 673.

The major remaining scattering sources were the target chamber itself, the concrete walls of the room which were about 2 m from the target, the concrete floor which was 128 cm below the target and a light plywood platform which hangs over the 90° deflecting magnet and was about 1 m from the target chamber at its closest point.

At an incident proton energy of 2.934 MeV

an inverse square law check made by measuring the NaI counts per long counter count as the NaI crystal was moved back from the target indicated that 14% of the pulses greater than about 3 MeV were caused by room scattered neutrons when the NaI counter was in its standard position. The contribution of the scattered neutrons to the pulse height distributions becomes less important as the proton energy is descreaed because fewer neutrons are produced at places other than the target, e.g. the various beam defining slits, and the direct neutrons the $Li^7(p, n)Be^7$ have lower energies and therefore larger capture cross sections in the iodine of the crystal.

In the range of proton energies between 1.8 and 2.94 MeV the major sources of high energy gammas are the 17 MeV capture gammas from Be^8 and the capture gammas arising in the nickel. In order to determine their contribution to the pulse height distributions, a run was made 40 keV below the $Li^7(p, n)$ threshold. The pulse

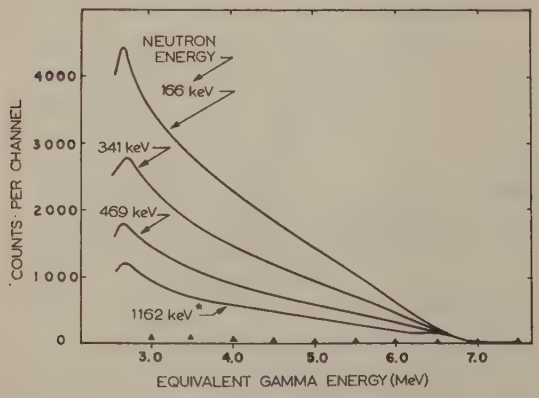

Fig. 2. Pulse height distributions produced by three monoergic neutron groups arising from the $Li^7(p, n)Be^7$ reaction in a $1\frac{3}{4}''$ D × 2″ NaI(Tl) crystal. The distribution labled 1162 keV is obtained after correcting for the presence of the 698 keV neutron group which was also present. Channel width 41 keV; — 1.8×10^5 neutrons/cm², incident on front face of crystal; ▲ Response 40 keV below threshold for same integrated charge as 166 keV curve.

height distribution produced by these gammas is shown in fig. 2. The pulse height distribution produced by 166 keV neutrons for the same integrated proton current is also shown in fig. 2. The difference between these two curves is the net neutron response, since the cross section for the production of 17 MeV Be^8 gammas is nearly constant in this region of proton energies[7]), and since there are many closely spaced resonances for radiative proton capture in each isotope of nickel[8]) so that the net amount of capture gamma radiation coming from the nickel foil, which was 40 keV thick to 2 MeV protons, is roughly independent of bombarding energy in the region of interest. The gamma background between 3 and 7 MeV is 5% of the total response for $E_n = 166$ keV. The percent of the total response due to gammas originating at the target increases with increasing bombarding energy until at $E_p = 2.934$ MeV (max $E_n =$ 1.162 MeV) it becomes 20% of the total response.

In order to obtain the value of the neutron flux at the different neutron energies studied, the long counter was calibrated against nuclear emulsions at a single proton energy. The proton energy chosen for the calibration was 2.934 MeV. This produced neutrons of energies 1.162 and 0.698 MeV at 30 degrees to the proton beam. Two Ilford C2 emulsions were located at 30° above the proton beam in the vertical plane. The plates had their front edges 8.97 cm from the target spot and were oriented so the neutrons entered parallel to the emulsion surface. The shielded long counter was also at 30° to the proton beam but in a horizontal plane and with its center 194 cm from the target spot. From the distribution of the number of proton recoil tracks versus track length obtained during a 193 minute exposure at an average beam current of 1 microampere the neutron flux was calculated. Only those tracks whose directions fell within a prism bounded by a 20° dip angle in the emulsion and angles in the emulsion plane 20° to either side of the neutron direction were counted. Of these, only those falling within a similar 15° prism were used for the calibration. From this measurement it was concluded that

[7]) F. Ajzenberg and T. Lauritzen, Revs. Mod. Phys. **27** (1955) 77.

[8]) C. R. Gossett, J. W. Butler, and H. D. Homgren, Bull. Am. Phys. Soc. Ser. II, **1** (1956) 40.

the total neutron flux 9.72 cm from the target spot consisted of $2.6 \pm 0.1 \times 10^7$ neutrons/cm² from the 1.162 MeV group and $5.8 \pm 0.6 \times 10^6$ neutrons/cm² from the 0.698 MeV group. During the time that neutrons were irradiating the emulsions, 3.84×10^6 long counter counts were recorded. For other neutron energies it was assumed that the relative sensitivity of the long counter followed the curve given by Hanson and McKibben[6]).

3. Results and Conclusions

The pulse height distributions produced by three monoergic neutron groups as well as the pulse height distribution which would be produced by 1.162 MeV neutrons is shown in fig. 2. The 1.162 MeV distribution was obtained by correcting the observed distribution at $E_p = 2.934$ for the effect of the 698 keV group. Each distribution is normalized to a neutron flux of 1.8×10^5 neutrons per cm² incident on the front face of the crystal.

The response of the sodium iodide crystal to various sets of neutron groups in the double energy region, scattered neutrons and thick target $Be^9(p, n)B^9$ neutrons is shown in fig. 1.

The cross section given by Hughes and Harvey[9]) for the $I^{127}(n, \gamma)I^{128}$ reaction as a function of neutron energy is shown in fig. 3 as the solid line. The plotted points are from the present work and represent for each neutron energy the sum of the counts in all channels between 2.73 and 6.17 MeV after correction for scattered neutrons and gammas. A normalization factor was applied to cause the measurements to agree at $E_n = 166$ keV. The fit of the remaining points is confirmation that the observed pulse height distributions are indeed produced by

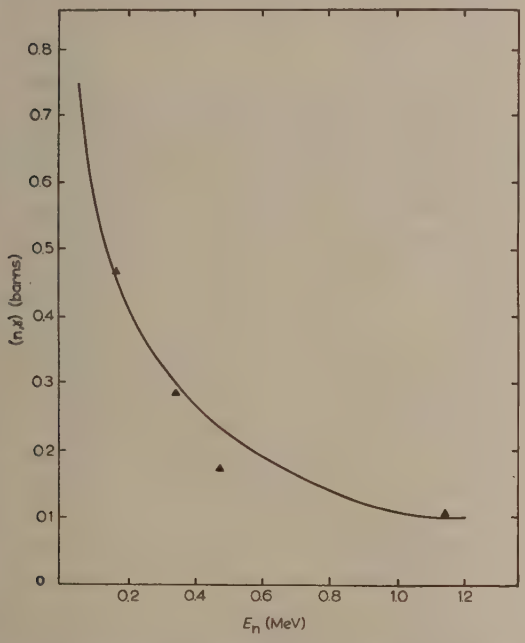

Fig. 3. Comparison of present work with the (n,γ) cross section curve for iodine. The plotted points are the total response of the crystal between 2.73 and 6.17 MeV after correction for the gamma background and scattered neutrons. The solid line is the I^{127} neutron capture cross section curve.

▲ Present work. Arbitrary units normalized at $E_n =$ 166 keV.

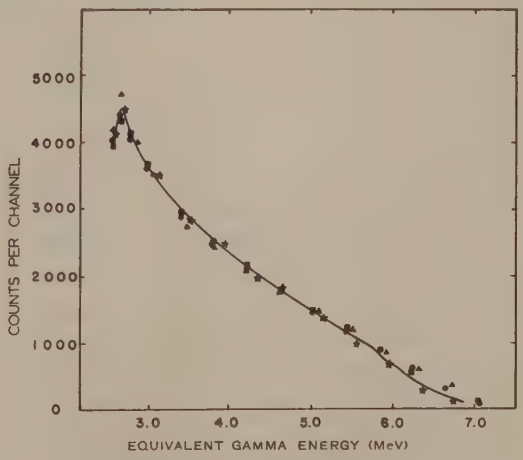

Fig. 4. Comparison of shapes of pulse height distributions for various neutron energies. Each ordinate of the curves in fig. 1 and of curves similar to those in fig. 2 is multiplied by the factor in parentheses. The factors were chosen so as to make all curves coincide at 4.62 MeV.

— 166 keV neutrons (30 100 l.c.); ★ E_n 0.7, 75 keV neutrons (0.7 × 30 100 l.c.); ■ E_n 341 keV neutrons (1.55 × 30 100 l.c.); ● E_n 469 keV neutrons (2.57 × 30 100 l.c.); ▲ E_n 1162-700 keV neutrons (3.32 × 30 100 l.c.).

[9]) Neutron Cross sections, compiled by D. J. Hughes and J. A. Harvey, Brookhaven National Laboratory Report BNL-325 (Superintendent of Documents, U.S. Government Printing Office, Washington, D.C., 1955).

neutron capture in the I^{127} within the scintillation crystal.

Furthermore the pulse height distributions of figs. 1 and 2 have similar shapes. The result of multiplying each of these distributions by a normalizing factor so that they all coincide at 4.62 MeV gamma equivalent is shown in fig. 4. Since the resultant curves closely coincide, it is possible to estimate the number of neutron produced counts in any energy interval in the pulse height region between 2.75 and 7.0 MeV in a NaI crystal if one knows the neutron flux as a function of energy incident on the crystal. The number of neutron produced counts, N, in a given pulse height region is:

$$N = K\ N^*\ \Sigma\ F(E)\,\sigma(E)$$

where N^* is the number of counts in the pulse height region of interest from the 166 keV curve of fig. 2. K is a constant which depends on the size and shape of the crystal as well as the shape of the 166 keV curve. $K = 1.18 \times 10^{-5}$ cm^2/neutron barn. $F(E)$ is the number of neutrons per cm^2 of energy E incident on the crystal. $\sigma(E)$ is the $I^{127}(n, \gamma)I^{128}$ cross section in barns.

It is evident from figs. 1 and 2 that the pulse height distributions can be approximated by straight lines in the region between 4 and 6.6 MeV. If these lines are extrapolated to the gamma equivalent energy axis they intersect it between 6.6 and 7.0 MeV, approximately the binding energy of the last neutron in I^{128} (6.58 MeV)[10]).

Acknowledgments

We are greatly indebted to Dr. J. H. Roberts for having performed the nuclear emulsion neutron flux measurement on his project supported by the Atomic Energy Commission through an Argonne National Laboratory subcontract.

We are also indebted to Professor Murray Peshkin for several illuminating discussions.

We are grateful to the Atomic Energy Commission for support during completion of the accelerator and construction of auxiliary equipment.

[10]) N. S. Wall, Phys. Rev. **96** (1954) 664.

NUCLEAR INSTRUMENTS 3 (1958) 303–306; NORTH-HOLLAND PUBLISHING CO. – AMSTERDAM

RADIOFREQUENCY MODULATION IN THE THONEMAN ION SOURCE

J. ERÖ

Central Research Institute for Physics Department of Atomic Physics, Budapest

Received 25 August 1958

A fast energy analyser using a scintillation detector has been made which is able to trace the spectrum in 20 μs. It is shown that the ion beam has r.f. modulation of about 50 eV. A demodulating r.f. field after the exit channel eliminates this modulation if the ions pass through it at right phase, and thus the energy spread of the beam is diminished below 10 eV. By determining the time of flight of ions from the r.f. modulation to the demodulating field the conclusion was drawn that the r.f. modulation occurs immediately near the cathode.

1. Introduction

The energy spread of the ion beam of a Thoneman-type radiofrequency ion source is usually believed to be very small as the ions in the plasma of the discharges do not receive energy from the r.f. field owing to their large mass. However no experimental evidence supports this view[1]). Up to now the only satisfactory measurement of the energyspectrum reported in an earlier paper[2]) indicates an energy spread of 40–50 eV. In this paper the possibility of an r.f. modulation due to the interaction of the r.f. field with ions accelerated by the extracting d.c. voltage was shown to exist. The experimental investigation of this effect involved many difficulties, as the stabilities of the power sources were insufficient to warrant a detailed study of the spectrum. Moreover if any low frequency modulation were present, it could hardly be distinguished from the r.f. modulation. To avoid these difficulties the present work was performed by means of a high speed energy analyser taking the full spectrum within several μs. In this way only r.f. modulations of several Mc/s have been detected neither low frequency modulations, nor instabilities effect the result.

2. Experimental Arrangement

The energy analyser was an electrostatic deflector described in[2]) with a radius of 160 mm and an analysing slit of 0.2 mm breadth. The constant of the deflector was $A = 10$ eV/V, and it had a resolving power of about 0.2 p.c. To get high speed indication a thin CsI scintillating crystal served as detector instead of the electrometer used earlier. The time resolution of the detector system (crystal+electronics) was about 1 μs. The d.c. deflector voltage was modulated by means of a square-wave generator of 50 c/s having a slope of 0.4 V/μs and an amplitude of 60 V. This modulation of the deflector voltage caused the ion beam to sweep the analyser slit 100 times per sec. The time of passing of a 100 eV broad beam through the slit was 25 μs, according to the slope and the deflector-constant given above.

The whole arrangement is shown in fig. 1. The pulses from the multiplier were led to the vertical deflector plates of an oscilloscope the horizontal deflection of which was performed by the square-wave voltage itself. In this way the energy spectrum immediately appeared on the screen. To get the spectrum only once a period the light intensity was triggered by pulses obtained by differentiating the square-wave. The energy calibration was performed by altering the d.c. deflector voltage by a given value and

[1]) Flügge, Handbuch der Physik, Bd. 33 (1956). Korpuskularoptik. Kamke, Elektronen- und Ionenquellen.

[2]) J. Erö, Das Energiespektrum des Ionenstrahls einer Hochfrequenzionenquelle. Acta Physica Hungarica 5 (1956) 391.

measuring the corresponding displacement of the spectrum on the screen.

Above 2 keV ion energy the intensity of the scintillations in the crystal was enough to give pulses higher than the multiplier noise, but is the characteristic shape. It did not change substantially under very different conditions, the only observable effect being the increase or decrease of the breadth. Reducing the probe voltage from 4 kV to 2 kV the breadth decreased

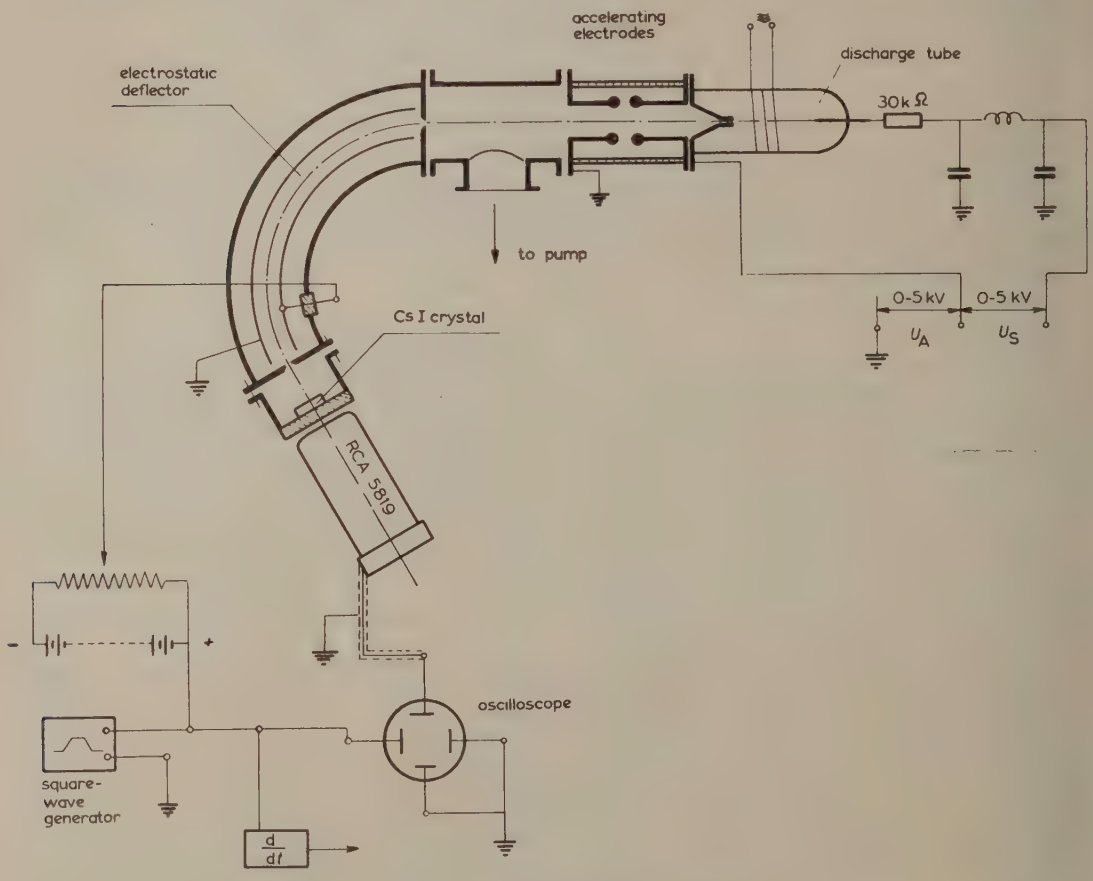

Fig. 1. Diagram of the experimental arrangement.

using probe voltages $U_s < 2$ kV an afterward acceleration of several keV was needed (U_A in fig. 1).

3. Measurements

After leaving the source the ions were completely screened against the r.f. field. A typical spectrum taken at $U_s = 3$ kV probe voltage is shown in fig. 2. The distance between two marks corresponds to 55 eV energy difference, thus the breadth of the spectrum is 50 eV. Remarkable by about 10–15% if the discharge had a high intensity, while at low intensity the decrease amounted 30–35 p.c. Keeping U_s constant a more pronounced variation was observed changing the r.f. field. Fig. 3 shows two spectra, both taken at $U_s = 4$ kV with the discharge having the same low intensity. In the first case (fig. 3a) the permanent magnetic field at the discharge had its optimal value and the oscillator power was reduced, while in the second case (fig. 3b) the oscillator power was kept at its maximum

value and the magnetic field was altered to get the same weak discharge. Owing to the increased r.f. field in case b, the distance between the two peaks grew from 45 eV to 86 eV.

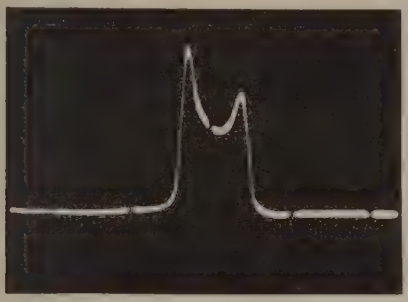

Fig. 2. Energy spectrum at 3 keV, showing the characteristic shape of an r.f. modulation. The distance between two marks corresponds to 55 eV.

The shape of the spectra points out very markedly the presence of r.f. modulation, being like the well-known $1/\sqrt{a^2 - y^2}$ amplitude-distribution of the sinus curve. The r.f. origin the energy spread is supported also by the fact mentioned above that the larger the r.f. field the broader is the spectrum.

between the two screens was about $d = 12$ mm and owing to the high r.f. impedance the leakage field of the oscillator produced a large r.f. field between them.

It is easy to show that a particle of charge e, and of velocity v entering the space between the two screens at time t', changes its energy by the amount

$$\Delta\mathscr{E}_2 = \frac{vE_0e}{\omega}\sqrt{2}\,\sqrt{1 - \cos\Delta\varphi}\,\sin\left(\omega t + \varphi_0 + \tfrac{1}{2}\Delta\varphi\right) \quad (1)$$

if the field strength in this space is $E = E_0 \sin(\omega t + \varphi_0)$ and the particle has an energy $\mathscr{E} \gg \Delta\mathscr{E}$. In this expression $\Delta\varphi = (d/v)\,\omega$, i.e. the phase angle corresponding to the time of flight in the r.f. field. Let the energy of a particle beam originally modulated as $\mathscr{E} = \mathscr{E}_0 + \mathscr{E}_1 \sin(\omega t - \varphi_1) = \mathscr{E}_0 + \Delta\mathscr{E}_1$ then after passing through the field the resulting modulation will have a minimum value when the phases of $\Delta\mathscr{E}_1$, and $\Delta\mathscr{E}_2$ are opposite, i.e.

$$\varphi_0 + \tfrac{1}{2}\Delta\varphi = -\varphi_1 + (2n + 1)\,\pi\ . \quad (2)$$

$\varphi_1 = \omega l_1/v$ represents the time of flight from the position of the first modulation to the first screen. With the notation $l'_1 = l_1 + \frac{1}{2}d$ our phase-condition (2) will be

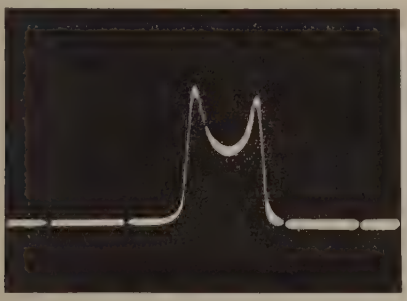

Fig. 3a

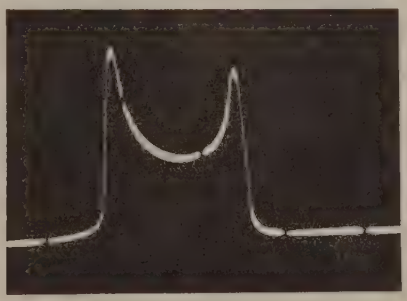

Fig. 3b

Fig. 3. Energy spectra in case of a low intensity discharge. (Distance between two marks is 55 eV.)
Fig 3a. Low r.f. field. Fig. 3b. High r.f. field.

To eliminate the energy spread, and at the same time to get a doubtless evidence of the modulation being due to the oscillator field, the ion beam was passed through a demodulating r.f. field. This was performed by inserting two screens with a high r.f. impedance between them after the exit channel (fig. 4). The distance

$$\frac{\omega}{v}l'_1 + \varphi_0 = (2n + 1)\,\pi$$

or

$$\frac{1}{v} = \frac{(2n + 1)\,\pi - \varphi_0}{l'_1\omega} \quad (3)$$

Using an oscillator of 60 Mc/s condition (3) was satisfied, say, at $U_s = 4.42$ kV, and a very narrow spectrum was obtained shown in fig. 5.

The line breadth is 15 eV, but this figure gives only the upper limit of the energy spread, as the resolving power of the analyser was ≈ 0.2

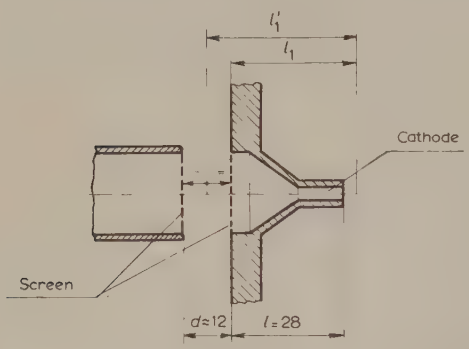

Fig. 4. The cathode of the ion source and the two demodulating screens.

p.c. corresponding to an energy of $8 \approx 10$ eV. This means that the energy spread of the ions of the Thoneman-source is below 10 eV after eliminating the r.f. modulation.

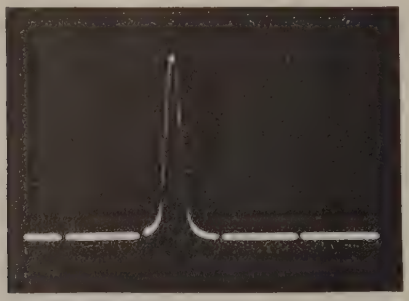

Fig. 5. Energy spectrum after eliminating the r.f. modulation. (Distance between two marks is 55 eV.)

The distance between the two peaks of the spectrum had minima not only at 4.42 keV energy. Fig. 6 shows the peak distance $\Delta\mathscr{E}$ as a function of the reciprocal velocity of the ions at 60 and 27 Mc/sec oscillator frequencies. There are very sharp equidistant minima. Let $\Delta_i = 1/(v_{i+1}) - 1/v_i$ the difference of reciprocal velocities between the i-th and $(i+1)$-th minima, then eq. (3) gives:

$$\Delta_i = \frac{2\pi}{l'_1 \omega} \quad \text{and} \quad l'_1 = \frac{1}{\nu \Delta_i} . \tag{4}$$

Knowing ν and Δ_i, one can determine l'_1 and thus the position of the r.f. modulation in the ion source. Table 1 gives the mean values of $1/v_i$ measured at several frequencies, and the corresponding l'_1.

Table 1

Frequency (Mc/sec)	$10^6 \Delta_i$ (sec/m)	l'_1 mm	
27	1.1	33.6	
48.5	0.51	40.5	
53	0.5	37.6	$\overline{l'_1} = 37{,}8$ mm
54.3	0.49	37.5	
56.1	0.46	38.6	
60	0.43	38.7	

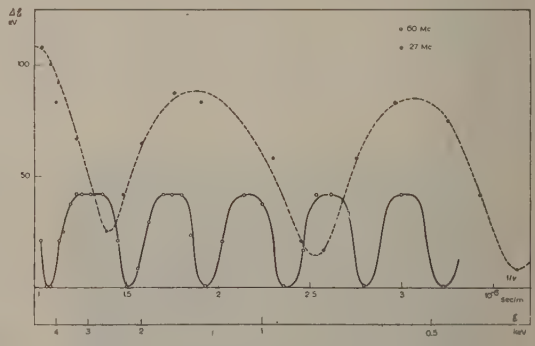

Fig. 6. The distance of the two peaks of the spectrum as a function of the reciprocal velocity, at 60 Mc (full line) and 27 Mc (dotted line).

According to the mean value of $\overline{l'_1} = 37.8$ mm, the distance $l_1 = (l'_1 - \frac{1}{2}d)$ is $l_1 = 31.8$ mm (see fig. 4). This shows that the r.f. modulation occures just before the cathode, most probabaly in the dark space.

I am indebted to Mr. L. Vályi for his valuable help in the measurements.

NUCLEAR INSTRUMENTS 3 (1958) 307–308; NORTH-HOLLAND PUBLISHING CO. – AMSTERDAM

LETTER TO THE EDITOR

METHOD FOR ELIMINATING THE EFFECTS OF AMPLITUDE DRIFTS IN MEASUREMENTS OF RATIOS OF COUNTING RATES

G. GOLDRING, M. BIRK, Z. KAMIL† and D. MYDANSKY†

Department of Physics, The Weizmann Institute of Science, Rehovoth

Received 16 June 1958

In measurements of ratios of counting rates, the effects of amplitude drift can be eliminated by the use of one amplifier and one pulse height analyser common to all radiation detectors. A mixing and relaying system incorporating this method is described.

1. Introduction

In many experiments one measures the ratio of counting rates in two detectors, which are set to monitor radiations of fixed given energies. The energy is usually defined by single channel pulse height analysers preceded by linear amplifiers and a drift in either amplifier or in either analyser will affect the counting rate and ultimately the measured ratio.

In a double scattering of β-rays experiment[1]) carried out in this laboratory, these drifts imposed a serious limitation on the accuracy, since the counting rates were strongly dependent on energy.

In order to eliminate this effect, a method has been devised where the pulses from both detectors are passed through one amplifier and one analyser and then correspondingly relayed to two scalers.

2. Method

A block-diagram of the circuit used is given in fig. 1. This is a "mixing-resolving" arrangement, where pulses from either detector are passed, through a mixer, into a common amplifier-analyser system and then resolved to feed two different scalers. The relaying of the output of the analyser to the proper scalers is done by the two gates. A gate will open only when it receives a coincidence pulse from its detector. The two discriminators are set to be triggered by pulses resulting from radiations of an energy somewhat lower than that corresponding to the threshold of the pulse height analyser. In this way, the possibility of false counts in the scalers due to random coincidences is reduced.

Conventional electronic circuits have been used in the instrument. The mixer is a double-triode with a common cathode-resistor. The pulses from the two detectors are fed into the two grids and the output is taken from the common cathode. Each discriminator consists of an amplifying stage and a secondary-emission tube (EFP60) trigger circuit[2]). The gates are 6BN6 tubes which are opened by the discriminators for 3 microseconds.

It should be noted that at high counting rates the possibility of superposition, at the mixer, of pulses coming from the two detectors cannot be neglected. Another problem is the possibility of pulses getting through the improper gates. Thus, at high counting rates, one has to shorten the pulses coming out of the detectors and also the duration of the gating pulses.

When the number of pulses of amplitudes

† Israel Atomic Energy Commission.

[1]) A. de Shalit *et al.*, Phys. Rev. **107** (1957) 1459.

[2]) N. F. Moody *et al.*, Electronic Engng. **24** (1952) 214.

above the range of the single channel pulse height analyser is considerably high, it would be advisable to use "windows" instead of discriminators.

phototubes is practically unaffected by power-supply drift. Drifts in the pre-amplifiers and in the mixer, which are cathode-followers, may be neglected.

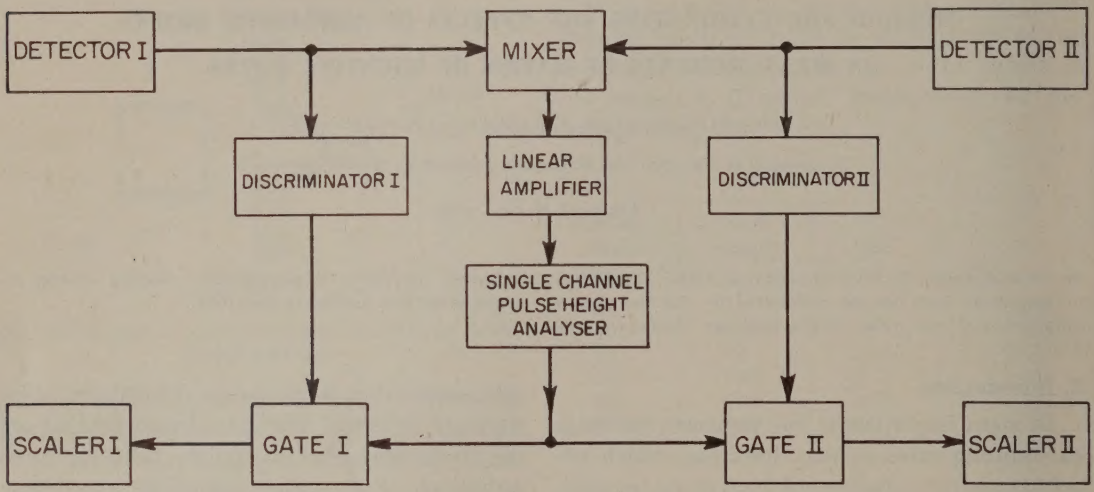

Fig. 1. Block-diagram of mixing-resolving arrangement.

The use of one amplifier and one analyser requires that the output pulses of the two detectors be in the same amplitude range. This is achieved by adjusting the high voltages supplied to the two photomultiplier tubes. These voltages have been obtained, through variable series resistors, from one power supply and thus the ratio of the gains of the two

3. Performance

The instrument has been in operation for several months and has proved reliable. The ratio of the counting rates recorded by the two scalers was found to remain constant even though the drift in amplifier and pulse height analyser caused fluctuations of up to 5 per cent in the counting rate of each scaler individually.

NEWS ITEM

Columbia University and Sylvania-Corning Nuclear Corp. announce establishment of First International Symposium on Nuclear Fuel Elements; Two-day session planned for January 28–29, 1959, at Columbia.

Spotlight on Industry

This section appears each month and features various happenings of interest in the nuclear industrial world and objective information on products of the nuclear manufacturers. It is offered entirely as a service and all nuclear manufacturers are cordially invited to submit clearly objective and descriptive material on their endeavors and product developments for consideration for use in this section.

MACHINED BERYLLIUM OXIDE SHAPES

The Beryllium Corporation, Reading, Pennsylvania

Hot pressed and machined beryllium oxide shapes designed for new applications are now being produced.

In the production of these shapes, high purity beryllium oxide powder is calcined from specially processed beryllium hydroxide at 1000°C. A light, fluffy material with an average particle size of one to two microns, the powder is packed in graphite molds for hot pressing in an induction pressing furnace. Densities exceeding 95 per cent theoretical can be attained in the hot pressing operation.

After cooling, the beryllium oxide blocks are machined into desired shapes by diamond-tipped machine tools operating in closed air systems. Machine tools are pres-set or remotely controlled. The finished product is an extremely smooth, uniformly dense material.

Blocks up to 12 inches in diameter and 6 inches in height are now being produced. They may be machined with extremely close tolerances into building blocks.

SCANNING CONTROL

Assembly Products, Inc., Chesterland, Ohio

As many as 24 stations may be monitored in sequence with a new scanning control.

An abnormal condition at any point is instantly indicated by a red warning light atop the control and by an alarm, if one is wanted. In addition, the equipment being monitored may be shut down if this is desirable. For quick trouble-shooting, the number of the station affected is shown in a Burroughs tube.

Originally developed for monitoring temperatures from minus 200 degrees to plus 3000 degrees Fahr., the scanner will provide similar protection with almost any other measurable variable.

A selector switch, immersed in oil for long operating life, checks stations in order, 12 per minute. Signals from thermocouples or other sources are indicated continuously by the moving pointer of the meter-relay. The alarm is sounded if the indicating pointer touches either a high or low limit pointer.

Special safety feature are applied.

PNEUMATIC INDICATING & RECORDING CONTROLS

Ad. Auriema, Inc., 85 Broad Street, New York, 4, New York

The Partlow Corp. has introduced a new low-cost pneumatic recording controller and a pneumatic indicating temperature controller. Both the recording and the indicating controls feature a readily adjustable throttling range of 3 to 20 per cent. Both controls also utilize an interchangeable mercury thermal element as the sensing medium.

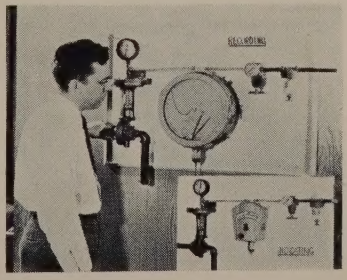

The *recording* control is designed to utilize a 15 pound air line to actuate an air-operated device. It is available in any of 10 optional temperature ranges within the extremes of —35 to 600 degrees C. The control has a built-in, failsafe provision in its design. It features a 10-inch circular hart either electric or spring driven for 24 or 48-hour or 7-day periods. One of the features is a readily adjustable throttling range, 3–20%.

ELECTRONIC VOLTMETERS

Metronix, Inc., Chesterland, Ohio

The smallest self-contained electronic voltmeters now available, requiring only as much panel space as ordinary $4\frac{1}{2}$-inch meters, are announced.

These single-range vacuum tube voltmeters were especially designed for panel-mounted O.E.M. applications where their high input resistance will not affect circuits being monitored. For compact mounting, barrels are only $4\frac{1}{2}$ inches deep, overall.

Accuracy is plus or minus 2 per cent of full scale deflection, except that AC voltmeters operating above 50 kilocycles frequency have 3 per cent accuracy.

SIGNS FOR SAFTEY

Picker X-Ray Corporation 25 South Broadway White Plains, New York

Anyone who uses radioactive isotopes in a quantity large enough to expose personnel to appreciable levels of radiation can meet AEC recommendations governing radiation warning signs with two new aluminium signs.

One sign, marked *Caution Radiation Area*, is for areas where the radiation level exceeds 5 millirem per hour but is less than 100 millirem per hour. The other sign, marked *Caution high Radiation Area, Personnel Monitoring Required*, is for areas where the radiation level exceeds 100 millirem per hour. In the latter areas the AEC requires personnel monitoring, which is the wearing of devices that measure the amount of radiation received. The fact that the AEC requires personnel monitoring in high radiation areas is noted on the high radiation sign for extra warning.

Both signs contain the radiation caution symbol, color, and words prescribed by AEC regulations.

PDI DIGITAL DATA SYSTEM

Borg-Warner International Corporation 36 South Wabash Avenue, Chicago 3, Illinois

A new system, called Precision Digital Instrumentation, is built around BJ Electronics' exclusive Vibrotron Transducer, which accepts any standard 3–15 psig input and converts this *directly* into a precise FM frequency output.

According to Borg-Warner International the use of direct conversion and FM techniques in the PDI System represents an important approach to process instrumentation.

The Vibrotron Transducer consists essentially of a length of fine wire stretched between a pressure sensitive diaphragm and an anchor point, with the wire set into motion by a special Vibrotron Amplifier. Pressure variations change the vibrating frequency of the wire, and the electrical FM output frequency of the Vibrotron changes accordingly, providing the necessary digital information ready for final processing and readout.

In addition, the FM approach is said to permit the use of solid state device switching throughout.

Response of the equipment (from pressure-line input to data output) is said to be virtually instantaneous and adaptable to almost any readout-rate requirement.

NEW ATOMIC MATERIALS LABORATORY

Nuclear Metals, Inc., Concord, Mass.

The largest privately-owned metallurgical research and development laboratory in the world was opened recently in one of America's most historic towns – Concord, Mass.

NEW SCINTILLATION DETECTOR

Nuclear-Chicago Corporation, 223, West Erie Street, Chicago 10, Illinois

The Nuclear-Chicago Model DS8 Scintillation Probe provides precision detection of fast or slow neutrons, gamma and beta radiation. Utilizing a new 10 stage, $\frac{3}{4}''$ photomultiplier

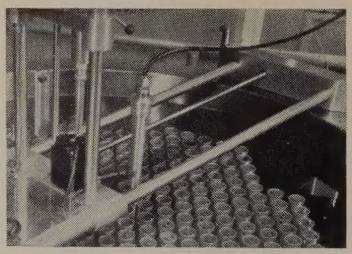

tube and a transistorized electronic circuit, the basic detector weighs less than 5 ounces and is just 1″ in diameter It is completely water tight and corrosion proof. A resolution time in the microsecond region permits its use in extremely high radiation fields.

$\frac{11}{32}''$ Accessories include a neutron probe in diameter for flux measurements in reactors and subcritical assemblies. The neutron sensitive area is confined to the very end of the 42″ probe so that "point" measurements may be made easily. The probe housing is quickly removed to permit substitution of fast neutron or slow neutron sensitive phosphors.

10-MeV TANDEM ACCELERATORS

High Voltage Engineering Corporation, Burlington, Mass.

A giant 10-million-electron-volt Tandem Van de Graaff accelerator for basic physics research, fourth of its kind in the world, will be installed in 1960 at the Kellogg Radiation Laboratory of CalTech. Programs utilizing the accelerator will be under direction of Dr. C. C. Lauritsen, senior scientist.

The Tandem features extreme beam homogeneity and stability in the 10 MeV energy range. The 35-ton machine comprises two 5-MeV Van de Graaff accelerators horizontally placed end to end with a common high voltage terminal.

First machine of this type is now being installed at the Chalk River Facility of Atomic Energy of Canada Ltd. Second and third machines respectively will go to the University of Wisconsin and Florida State University.

NEW PROCESS

Corning Glass Works, Corning, New York

Extremely thin-walled ceramics formed into lightweight honeycomb structures capable of operating at high temperatures have been introduced by Corning Glass Works.

Bulk specific gravity 0.5. Specific gravity of material 2.6. Melting temperature 1250–1350° C. Specific heat (25° C) 0.20 cal/g. Mean specific heat (25–400° C) 0.24 cal/g. Linear coefficient of thermal expansion (25–300 °C) 1×10^{-7}/° C. Short time no load max. operating temp. 1000° C. Long time no load max. operating temp. 700 °C. Compressive strength: Parallel to cell 2000 psi; Perpendicular to cell, parallel to flat rib 400 psi; Perpendicular to cell, perpendicular to flat rib 40 psi. Hole size average 0.095″ long, 0.045″ high. Construction, corrugations/inch 20. Open frontal area 75–80%. Surface area 1500 ft^2/ft^3. Wall structure porous, permeable. Web thickness 0.005″. Max. diameter presently available 20″. Max. cell depth presently available $3\frac{1}{2}''$.